THESIS FOR THE DEGREE OF DOCTOR OF PHILOSOPHY

Thermal properties of clusters and molecules

- Experiments on evaporation, thermionic emission, and radiative cooling

ERIKA SUNDÉN

UNIVERSITY OF GOTHENBURG

Department of Physics
University of Gothenburg
Göteborg, Sweden, 2012

Thermal properties of clusters and molecules
- Experiments on evaporation, thermionic emission, and radiative cooling
Erika Sundén

ISBN: 978-91-628-8429-1

Doktorsavhandling vid Göteborgs Universitet

Atomic and Molecular Physics
Department of Physics
University of Gothenburg
SE-412 96 Göteborg
Sweden
Telephone +46 (0)31 786 1000

Typeset in LaTeX

Figures created using MATLAB, Power Point, Chemcraft, and Inkscape.

Printed by Kompendiet
Göteborg, Sweden 2012

THERMAL PROPERTIES OF CLUSTERS AND MOLECULES

- Experiments on evaporation, thermionic emission, and radiative cooling

Erika Sundén

Department of Physics
University of Gothenburg
Göteborg, Sweden, 2012

ABSTRACT

This thesis presents experiments performed on clusters and molecules, where the three channels of unimolecular decay have been studied. Evaporation from protonated and negatively charged water cluster have yielded size dependent heat capacities, where the smallest sizes with fewer than 21 molecules show a heat capacity similar to bulk ice whereas clusters with molecules between 21 and 300 have a heat capacity in between that of ice and liquid water. The increase in heat capacity per added molecule in the cluster indicates that the intramolecular degrees of freedom are frozen at the temperatures in the experiment (T≈160 K). Experiments on small mixed water-ammonia clusters resulted in relative evaporation fractions for sizes between a total of three to eleven molecules, and 16 molecules. The clusters were found to evaporate predominantly water molecules except for clusters containing six or more ammonia molecules. Relative evaporation rates for D_2O, HDO, and H_2O were measured for $NH_4^+(H_2O)_4$ with zero to six deuteriums interchanged with the hydrogens. The relative rates were found to be $1 : 0.71 : 0.56$.
Absolute timedependent cooling rates for hot C_{60}^- were obtained in an electrostatic storage ring with single photon absorption experiment. The cooling of the molecule could be divided into a thermionic emission part and a radiative part, where the crossover between the two occurred at 5 ms, after which radiation was shown to be the dominant cooling channel. The spontaneous decay profiles were used to extract decay parameters of the large organic anion zink phthalocyanine (ZnPc). Numerical simulations of the decay process show good agreement with measurements, using parameters derived from an analytical approximation also used for fullerenes. Photoabsorption experiments were performed on the much smaller C_5^-, showing the presence of strong radiative cooling. The cooling rate was determined by the dependence of the photoinduced neutralization yield vs. photon energy and laser firing time.

Keywords: water clusters, fullerenes, unimolecular decay, evaporation, thermionic emission, radiative decay, cooling rates, heat capacities

Research publications

The work presented in this thesis is an introduction to and summary of the following research articles, referred to as Paper I-IV.

PAPER I

Heat capacities of freely evaporating charged water clusters
A. E. K. Sundén, K. Støchkel, S. Panja, U. Kadhane, P. Hvelplund, S. Brøndsted Nielsen, H. Zettergren, B. Dynefors, and K. Hansen
Journal of Chemical Physics **130** (2009) 224308

PAPER II

Relative light and heavy water evaporation from $NH_3(H_2O)_3H^+$ *clusters*
A. E. K. Sundén, K. Støchkel, P. Hvelplund, S. Brøndsted Nielsen, B. Dynefors, and K. Hansen
In manuscript (2012)

PAPER III

Absolute cooling rates of freely decaying fullerenes
A. E. K. Sundén, M. Goto, J. Matsumoto, H. Shiromaru, H. Tanuma, T. Azuma, J. U. Andersen, S. E. Canton, and K. Hansen
Physical Review Letters **103** (2009) 143001

PAPER IV

Radiative cooling of C_5^-
M. Goto, A. E. K. Sundén, Y. Zama, H. Shiromaru, H. Tanuma, T. Azuma, J. Matsumoto, Y. Achiba, and K. Hansen
In manuscript (2012)

Publications not included in the thesis:

Near-infrared photoabsorption by C_{60} dianions in a storage ring
U. Kadhane, J. U. Andersen, E. Bonderup, B. Concina, P. Hvelplund, M.-B. Suhr Kirketerp, B. Liu, S. Brøndsted Nielsen, S. Panja, J. Rangama, K. Støchkel, S. Tomita, H. Zettergren, K. Hansen, A. E. K. Sundén, S. E. Canton, O. Echt, and J. S. Forster
Journal of Chemical Physics **131** (2009) 014301

Studies of Unimolecular Decay in Model Cluster Systems
A. E. K. Sundén
Licentiate Thesis, University of Gothenburg (2009)

Mikroskopiska vattendroppars egenskaper - en pusselbit i klimatfrågan
Erika Sundén och Klavs Hansen
Fysikaktuellt **2** (2011) 9

TABLE OF CONTENTS

Research publications I

Table of Contents III

1 Introduction 1

2 Clusters and molecules 3
2.1 Water clusters . . . 5
2.1.1 Protonated water clusters . . . 7
2.1.2 Mixed water and ammonia clusters . . . 11
2.2 Carbon containing molecules and clusters . . . 11
2.2.1 Fullerenes . . . 12
2.2.2 Large carbon-containing molecules . . . 14
2.2.3 Small carbon molecules . . . 15

3 Experimental techniques and equipment 17
3.1 Cluster sources . . . 17
3.1.1 Corona discharge . . . 17
3.1.2 Laser desorption . . . 19
3.2 Linear accelerator . . . 19
3.3 Storage rings . . . 22
3.4 Detection . . . 24
3.5 Laser excitation . . . 25

4 Theory of thermal decay 27
4.1 Statistical decay channels . . . 28
4.1.1 Fragmentation . . . 29
4.1.2 Thermionic emission . . . 33
4.1.3 Radiative cooling . . . 34
4.2 Cluster abundances and energy distributions . . . 35
4.2.1 Fragmentation in the small cluster limit . . . 36
4.2.2 Fragmentation in the large cluster limit . . . 39
4.2.3 Thermionic emission and radiative cooling . . . 40

5 Evaporation from water clusters **45**
5.1 Heat capacities of charged water clusters 53
5.1.1 Poisson distributed evaporation 54
5.1.2 Heat capacities 55
5.2 Mixed ammonia and water clusters 57
5.2.1 Discussion on stability and structure 58
5.3 Relative evaporation rates for light, heavy, and mixed water molecules 61
5.3.1 Branching ratios and evaporation rates 62

6 Thermionic emission and radiative cooling **69**
6.1 Absolute cooling rates for C_{60}^- 69
6.1.1 Experimental procedure and data analysis 70
6.1.2 Results and discussion 72
6.2 Radiative cooling and thermionic emission for large molecules . 76
6.2.1 H_2tBTPP 78
6.2.2 ZnPc 79
6.3 Energy distribution of C_5^- 86
6.3.1 Experimental procedure 87
6.3.2 Results and discussion 88

7 Summary **93**

Acknowledgements **95**

Bibliography **99**

CHAPTER 1

Introduction

Cluster and molecular research is a huge subject containing many interesting and yet unexplored aspects. This thesis explores a small section of these aspects, applied to a handful of different clusters and molecules.

Cluster research is a fairly new branch of science and has attracted interest from a variety of disciplines such as physics, chemistry, biology, and medicine. The ability to study how collective properties develop from the smallest individual constituent, an atom or molecule, to the bulk material have deepened our understanding of matter. Yet there are many aspects left to discover and phenomena that still lacks explanations.

Utilizing vacuum systems and the ability to introduce and manipulate individual clusters and molecules inside them gives us the opportunity to study these systems with minimum interaction with the environment, thus probing the inherent properties of the clusters and molecules.

The focus of the work presented here is the study of the thermal properties of these small systems. How do individual clusters and molecules cool down, what happens to the energy? What can be revealed about the inherent properties of the clusters, molecules, or ensembles by measuring decay of different sorts (evaporation, thermionic emission, or radiative cooling)?

This thesis is divided up into five main chapters. Chapter 2 gives an introduction to the clusters and molecules studied here and what is known about these systems. The chapter contains two parts; one deals with water clusters (pure and mixed) and one introduces the different carbon containing molecules studied.

The next chapter deals with the experimental equipment used in the different experiments. The experiments performed on the three different water systems were carried out at the University of Aarhus in Denmark, using an apparatus called the Separator. For the carbon containing molecules we utilized an electrostatic storage ring, the TMUe-ring, at the Tokyo Metropolitan University in Japan. These two complex experimental setups are described from a user point of view, *i.e.* many of the intricate details of these two machines that are essential for their performance are left out from the descriptions herein.

Chapter 4 is the theory chapter. This chapter is intended to bring the reader up to speed on the terminology and the relations used in the following two experimental chapters. It goes into details of some of the derivations to clarify what assumptions are made behind the expressions and equations used later on. It is however not a comprehensive guide to unimolecular decay or the evaporative ensemble, for that I refer you to *e.g.* reference [1] which is the source of a lot of the material in this chapter.

The two main chapters are Chapter 5 and 6, where the experiments and the results are presented. Chapter 5 is about the evaporation experiments performed on three different types of water clusters and starts with a common introduction to the experimental procedure. Then the results from the three different water cluster systems are discussed separately. The next chapter deals with thermionic emission and radiative cooling from the carbon containing molecules. In the first section the results from absolute cooling rates from C_{60}^- are presented. The next section illustrates a different procedure for extracting cooling rates for molecular ions, utilizing only spontaneous emission. Finally, cooling rates and energy distributions for the small carbon ion C_5^- are presented.

The last chapter, Chapter 7, contains a brief summary of the most important results.

CHAPTER 2

Clusters and molecules

Gases of free atoms and molecules as well as the bulk have been studied extensively for a century. The intermediate region between an atom and the bulk is still to some extent unknown and the development of collective properties of atoms, such that exist in and characterize liquids and solids, have not been completely mapped out. Cluster research is here to bridge that gap. A cluster consists of a number of atoms or molecules that are bound to each other in some manner, ranging from just a couple of constituents up to several thousands.

The distinction between clusters and molecules is not so easily made. If only comparing certain selected species, one can say that a molecule is something you can buy in a bottle whereas a cluster is something more unstable or shortlived, although this is not true when including the vast number of shortlived molecular radicals. Another can be that a cluster is a system that is not closed in some sense, you can keep adding on or removing constituents from it. Physical and chemical properties of the cluster might however change as it grows or shrinks. The fullerene C_{60} is an example of where the scientific community has not agreed on the proper terminology, even in the first paper published on the structure both terms, 'molecule' and 'cluster', were used [2].

Some examples of cluster types are the rare gas clusters, bound together by van der Waals interactions. The relatively easy production method and their low reactivity have contributed to making them among the most widely studied types of clusters. Another type is the metal cluster family where the atoms are bound together via metallic bonds. They can be made up of a single element or a mixture of metals. Yet another family is the semiconductor clusters where typically covalent bonds holds the clusters together. We can also have ionic clusters which are often made up of two types of elements, *e.g.* a metal and a non-metal where the metal donates electrons to the non-metal and an ionic bond is created. Molecular clusters have bonds depending on their constituents, where often the polarizability of the molecules creates bonding between them. A form of this kind of bonding is called intermolecular hydrogen

bonding, which exists in clusters made up of molecules containing hydrogen and either oxygen, nitrogen, or fluoride, *e.g.* water clusters.

One reason for the study of clusters is to get a better understanding of properties associated with bulk volumes. These can be optical properties such as refractive index, absorbance, reflectivity, and color; electrical conductivity; thermodynamic properties such as heat capacity and melting/freezing point; and magnetic properties. In many cases it has been demonstrated that these types of properties undergo changes as the size of the cluster decreases. A well studied example is the case of gold clusters which have been observed to become non-metallic, good catalysts and change their color when the size of the particle is reduced to around 10 nm (see *e.g.* [3]).

The origin of these changes in physical properties can be attributed to the size of the particles. The physical confinement a cluster leads to a quantization of the energy levels. For metals, the confinement results in a type of 'superatom' with the valence electrons of each atom making up a superimposed cluster shell structure resembling that of an single atom. This shell structure is often seen in abundance spectra where the number of atoms corresponding to a shell closing generally has a higher abundance. This phenomenon was first discovered for sodium clusters, where an increased abundance was found for clusters containing $N = 2, 8, 20, 40, 58,$ and 92 atoms [4]. Also geometrical shell structure can contribute to higher abundances and more stable clusters [5]. The increased ratio of surface to 'bulk'-atoms or the preferred crystal structure (or lack thereof) of the cluster can also be the origin of size-dependent properties.

There are two fundamental applications for cluster research. One is 'material' applications, where clusters are made intentionally with a certain property that can be used in some technology. An important application is the use of nanoparticles or clusters as catalysts [6], and an example of a possible future application is using clusters as quantum dots for quantum computing [7, 8]. Investigations into radiative cooling of clusters can be very important in this context, where a study of C_{70} showed decoherence by radiation [9]. The other application is not a material one, *i.e.* does not generate a physical product, but instead furthers our knowledge of natural processes like particle formation in the atmosphere [10]. The two reasons for studying clusters are however not exclusive, and as in all science an application might appear that was not intentional from the start.

This chapter will give a brief background to the clusters and molecules studied in this work. It will not be a complete survey but instead highlight what is already known about properties related to the work presented here.

2.1 Water clusters

The study of water clusters can be used to map out the development from a single water molecule to bulk water. The water dimer is for instance the simplest system available for investigating the intermolecular hydrogen bonding in water. The nature of the bonding in liquid water has been an ongoing field of research for decades because of the many unique properties of water, like the density maximum at 4°C and the volume increase in the solid state. Some of these features are still not fully understood and explained.

Solvation of other types of atoms, molecules, or ions in water is another important field which can be studied by incorporating them in a water cluster of a well defined size. For instance, the properties of biomolecules may be very different in solvation *vs* in vacuum and the transition can be studied by attaching various numbers of water molecules to the biomolecule of interest.

Water clusters also carry an interest in themselves as they play a part in atmospheric processes. Although condensation on aerosol particles account for most of the droplet formation, ion induced nucleation is also believed to be a contributing factor, especially in the middle and upper troposphere where temperature is low and ion concentrations are relatively large [11, 12]. A possible pathway to aerosol growth is ions produced through *e.g.* galactic cosmic rays onto which water molecules attach [13]. Clustering of water molecules around ions was observed already at the end of the 19th century by a series of cloud chamber experiments carried out by Wilson, but at that time with the purpose of studying ionizing radiation [14].

Clustering, nucleation, and growth of an aerosol particle is dependent on ambient temperature, vapor pressure, radius, and constituents of the particle. A thorough derivation of the growth process can be found in reference [15]. Evaporation occurs mare easily from very small particles compared to a flat surface since the curvature causes reduced forces to act on the outermost layer of molecules. The partial vapor pressure needed for growth of a small particle is thus larger than the vapor pressure for condensation on a flat surface. The critical size of a particle is the size, which under a given vapor pressure and ambient temperature, will neither grow nor shrink. The critical diameter d_p for a particle made up of only one type of constituent (like water) can be expressed in terms of σ_s, M_w, and ρ which are, respectively, the surface tension, molecular weight, and density of the droplet liquid.

$$\frac{p_d}{p_s} = \exp\left(\frac{4\sigma_s M_w}{\rho R T d_p}\right), \tag{2.1}$$

where p_d/p_s is the ratio between the current vapor pressure and the saturation pressure. Particles larger than the critical size will grow whereas smaller

particles will evaporate and finally disappear. For growth to start on a single water molecule a theoretical supersaturation ratio (p_d/p_s) of 220 is necessary (*i.e.* the vapor pressure needs to be 220 times larger than the saturation vapor pressure over a flat liquid surface). However, even in unsaturated vapor molecular clusters can form due to attractive forces, such as van der Waals forces and/or intramolecular hydrogen forces. In this setting the clusters are not stable and will form and disintegrate continuously.

Ion induced nucleation and/or nucleation on another substance such as *e.g.* sodium chloride (from sea salt) will lower the threshold and reduce the critical size for a given vapor pressure and temperature. In the case of a soluble particle such as NaCl equation 2.1 is modified with a term on the right side consisting of the molecular weight of the salt M_s, the mass of the salt m and the number of ions produced in the solvation i (2 for NaCl) as

$$\frac{p_d}{p_s} = \left(1 + \frac{6imM_w}{M_s\rho\pi d_p^3}\right)^{-1} \exp\left(\frac{4\sigma_s M_w}{\rho RT d_p}\right). \tag{2.2}$$

The two factors in equation 2.2 are competing. For very small droplet sizes the factor containing the salt will dominate and the particle will grow up to the critical size as determined by equation 2.2. For larger d_p the exponential term will take over and the critical size will behave as pure water, as is expected when the salt becomes too dilute. See figure 2.1 for an illustration of this process.

Another proposed nucleation route, pertaining more to landlocked areas, contains water together with sulphuric acid and ammonia. This nucleation process has been measured *e.g.* in CLOUD, the nucleation chamber at CERN [16]. This work showed that both ionizing radiation and ammonia served to increase the nucleation rates. The necessity of ammonia in atmospheric nucleation events has been debated in the literature but the study at CERN as well as theoretical modeling (see *e.g.* [17]) have shown that it increases nucleation considerably compared to the binary situation of only water and sulphuric acid. Mixed ammonia and water clusters will be discussed more thoroughly in section 2.1.2.

Under the name of 'water clusters' fall both the neutral cluster $(H_2O)_N$ and some ionic species together with water molecules. The neutral clusters have, because of their lack of charge and thus difficulty to control and size select in an experimental setup, mainly been studied theoretically. Small neutral water clusters ($N = 2 - 10$) have however been investigated by momentum transfer experiments, where collisions with a rare gas beam were used for size selection (see *e.g.* Buck *et al.* [18]).

Among the clusters containing ionic species, there are the negatively charged water clusters which include both the hydroxide ions $(H_2O)_N OH^-$ and the

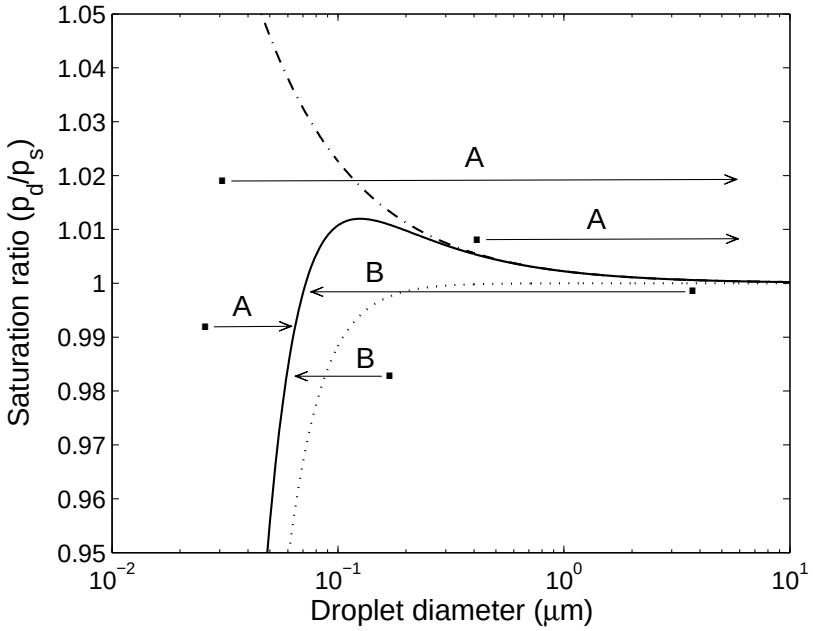

Figure 2.1: The critical diameter of a droplet containing 10^{-17} g NaCl. The solid line represents equation 2.2, the dotted line includes only the term pertaining to the salt and the dot-dashed line is the pure water term. For a constant pressure the arrows represent the evolution of a droplet. The particles labeled A will grow and the ones labeled B will evaporate and shrink.

clusters where there is simply one extra electron attached, $(H_2O)_N^-$. However, the most experimentally studied type of water cluster is the protonated one.

2.1.1 Protonated water clusters

Protonated water clusters are the water cluster type that has received most attention in experiments, probably in large due to the relatively simple production methods. When experiments were conducted trying to condense water around other types of ions such as O^+, O_2^+, N^+, N_2^+, or He^+ charge transfer quickly occurred creating $(H_2O)_N H^+$ [19]. Molecules with a higher proton affinity than water, *e.g.* ammonia, will however keep the extra proton and water can cluster around it. Mixed ammonia and water clusters will be discussed in the next section.

An early discovery and well studied feature of protonated water clusters is the appearance of the so called magic numbers [19, 20]. These magic number clusters are clusters with a specific number of molecules that in an otherwise smooth intensity mass distribution show up in higher abundance than

their neighbors. For protonated water clusters the most apparent magic numbers show up at cluster sizes of $N = 21$, 28 and 55 molecules. It was early shown that the magic numbers were not due to external factors such as production method used [21] and that they did not appear if detection was close enough in time to ionization [22,23]. Detection up to 4 μs after ionization still showed a smooth abundance distribution. The explanation of the time delay given by the authors was the high temperature still present in the clusters at short times after ionization. A particularly stable or unstable structure is not reached due to the 'liquid' state of the clusters. After enough time has passed enough molecules have evaporated and the structures freeze out to create the magic numbers detected. As a contrast they compare this behavior with other cluster types, such as the nobel gas clusters. There a timescale of a couple of atomic vibrations is enough to solidify the shell structure detected in abundance spectra.

Since the characteristic intensity variations in the protonated water cluster spectra were shown not to be due to the choice of production method, they must be inherent to the clusters themselves. In [24] it was shown through a determination of the dissociative activation energies deduced from abundance spectra that there are two different factors contributing to the magic numbers seen. The one at $N = 21$ falls under the shell closing category with both an increase in dissociation energy at 21 molecules and an decrease in dissociation energy for the cluster consisting of $N = 22$, whereas the magic numbers at $N = 28$ and 55 are the result of mainly a decrease in dissociation energies at the precursor of sizes $N = 29$ and 56.

The magic numbers are reproduced in our experiments as well and figure 2.2 shows a typical mass spectrum from a scan of the mass separating magnet at the separator in Århus. The magic number at $N = 21$ shows an increased abundance, but also the even number clusters at $N = 26, 28,$ and 30 show higher abundance than their neighbors.

In the experiment described in Chapter 5, spontaneous fragmentation of positively and negatively charged water clusters was studied. One could imagine that a process such as radiative cooling could contribute to cooling of the clusters, but this has been shown by Schindler *et al.* not to be the case within our experimental timescales [25]. They used an electromagnetic ICR-ion trap to study blackbody induced fragmentation of protonated cluster and found it to go approximately as $\tau = 1/N$ s, *i.e.* much slower than our experimental times (see Chapter 3.2).

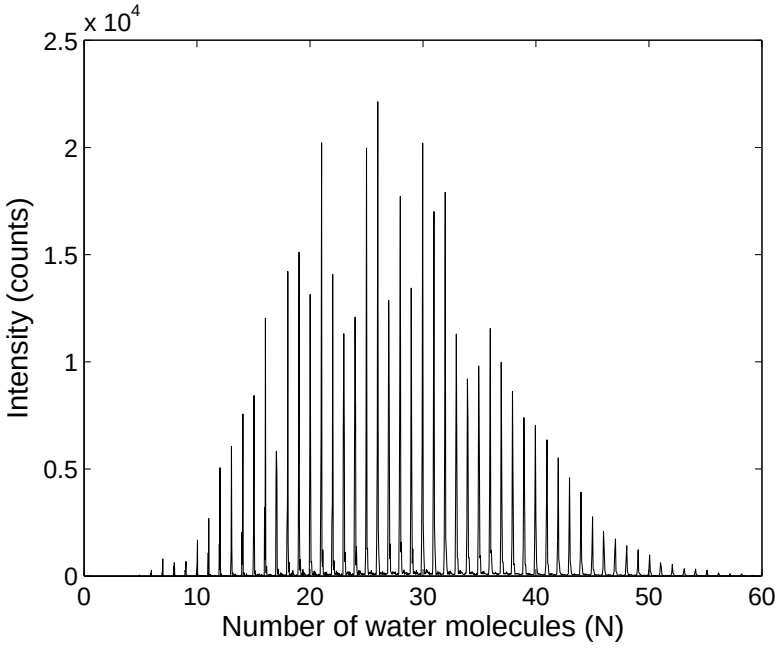

Figure 2.2: A typical mass spectrum in the small to medium size range of protonated water clusters.

Proton mobility

Proton mobility is a topic of interest in *e.g.* liquid bulk water because it has been found to be abnormally high. It is also of interest because it affects solvation and reactivity of other species in a water environment. The Grotthuss mechanism [26] describes the possibility of proton hopping when there is an excess proton in the mix. According to the theory the excess proton sits initially on one water molecule, which is connected to three other water molecules through hydrogen bonding. The extra proton then breaks its bond with the oxygen and is transferred to a neighboring molecule which in turn transfers a different proton to yet another molecule. The timescale for this process in bulk water has been found through neutron scattering to be about 1 ps [27].

Many different cluster studies have been performed to investigate the mechanism of proton exchange on a microscopic level. An advantage of using clusters in the study of proton mobility and exchange is the easy selection methods with complete control over the constituents in the experiment. In a typical experiment, a cluster containing N water molecules is selected and allowed to interact, at a well determined interaction energy, with heavy water molecules (D_2O). After a predetermined time, the extent of evaporation can be studied or an additional collisional activation step via collisions with a rare gas atom

can be carried out. The process studied is thus

$$\begin{aligned} H_3O^+(H_2O)_N + D_2O &\rightarrow [H_3O^+(H_2O)D_2O]^* \\ &\rightarrow \text{loss of } H_2O, HDO, \text{ or } D_2O. \end{aligned} \tag{2.3}$$

Detection of a cluster of even mass is clear evidence of proton scrambling, if one can exclude impurities in the experiment such as a mixture of HDO and D_2O in the collision cell. Experiments on proton exchange with clusters without an extra proton have also been performed, *e.g.* collisions between $(H_2O)_N^-$ and D_2O [28] where no scrambling was detected. This supports the idea of some sort of Grotthuss mechanism acting on the microscale as well as the macroscale.

In the case of pure protonated water clusters reacting with heavy water the verdicts on scrambling/non scrambling have been mixed. Smith *et al.* [29] performed cross beam experiments with $N = 0, 1, 2$ and saw that the resulting products were completely statistical, demonstrating a complete randomization of protons within the timespan of the intermediate state. On the other hand Honma and Armentrout [30] found the amount of proton exchange to be dependent on collision energy and that the lifetime of the intermediate state did not allow for complete H/D randomization.

Water systems with another ionic product have also been studied, such as the already mentioned negatively charged water clusters, but also O_2^- and NH_4^+. In the case of O_2^- no scrambling was found to take place [28], as expected on the basis of the Grotthuss mechanism. In the case of $NH_4^+(H_2O)_N$ the requirement of an extra proton is fulfilled but still no or very little scrambling was observed [31]. This was explained by the lower inherent acidity of the NH_4^+ ion, that means that transfer of a proton to a water molecule is a very energy demanding process and that therefore no H/D swaps occur.

Another aspect of mixed regular and heavy water clusters lies in their respective evaporation and nucleation rates. An experiment with either heavy water clusters picking up a light water molecule or vice versa and then colliding said mixed cluster with Ar atoms showed a slight preference for the heavy water to be in the neutral product [32], regardless of collision energy. The nucleation rates of heavy water and regular water clusters were measured by Wölk and Strey [33] finding a nucleation rate of a factor of 2500 higher for heavy water at the same vapor pressure and temperature. Desorption rates for thin ices made from either heavy or normal water were measured by Smith *et al.* [34] with the conclusion that heavy water evaporates at a $\approx 50\%$ slower rate compared to normal water at temperatures in the range $170 - 190$ K. These temperatures are comparable to freely evaporating small clusters in mass spectrometry experiments in vacuum, which will be shown in Chapter 5.

2.1.2 Mixed water and ammonia clusters

Many studies have revolved around mixed clusters containing water together with other molecules or atoms. A strong motivation for this is the atmospheric importance of such species, as discussed earlier in this chapter.

Another reason to study specifically ammonia and water mixed clusters is of more fundamental character. Both water and ammonia interact via intermolecular hydrogen bonds. Water is a symmetric molecule in that sense, with two donor sites on the two hydrogens and two acceptor sites on the oxygen. Ammonia is asymmetric and has three donor sites in the three hydrogen atoms and only one acceptor site. In an infinite network of hydrogen bonded molecules the most stable one should be the one with the highest number of symmetric constituents [35], but what happens in a system of finite size?

Of the mixed water and ammonia clusters $H^+(H_2O)_n(NH_3)_m$, $m = 1$ is the configuration most explored in the literature and much effort has been put towards finding the most stable configuration of the cluster. Many theoretical calculations [35–39] place the excess proton on the ammonia molecule creating an hydrated ammonium ion. The proton affinity of ammonia is 853.6 kJ/mol to be compared to 691 kJ/mol for water [40] which makes it energetically favorable for ammonia to carry the extra proton. However, for $n > 2$ infrared spectroscopy [41] revealed several isomeric structures regarding the other molecules in the clusters and high level calculations [41–43] have confirmed that the barrier separating these structures can be very low, around 2 kcal/mol corresponding to 0.1 eV/cluster.

Mixed clusters with more than one ammonia molecule have also been studied. For small mixed clusters the earliest proposed structure was four ammonia molecules surrounding an ammonium ion with water and the remaining ammonia molecules attached to an outer shell [44]. However, a later computational study [45] suggested that this was a too simple description and that there is a competition between ammonia and water for the last two molecular positions in the inner shell and for all the spaces in the second shell.

2.2 Carbon containing molecules and clusters

The field of carbon containing molecules and clusters is of course a nearly endless subject containing an enormous amount of species. This thesis will cover experiments made on four different molecules in four subgroups of carbon physics/chemistry; fullerenes, porphyrines, phtalocyanines, and small carbon clusters. In the experiments they are all negatively charged ions.

2.2.1 Fullerenes

Fullerenes (or Buckminsterfullerenes) are all-carbon based molecules with a cage-like geometry. The most famous and stable type of fullerene consists of 60 carbon atoms arranged in a truncated icosahedral structure, like a football with a carbon atom placed in each vertex of the 12 pentagons and 20 hexagons, see figure 2.3 for a drawing of the molecule. This proposed structure and the discovery of the great stability and abundance of C_{60} was made by Kroto, Curl, and Smalley in 1985 [2] for which they received the Nobel Prize in Chemistry eleven years later. All fullerenes contain 12 pentagons but can have various numbers of hexagons depending on the total number of carbon atoms making up the fullerene.

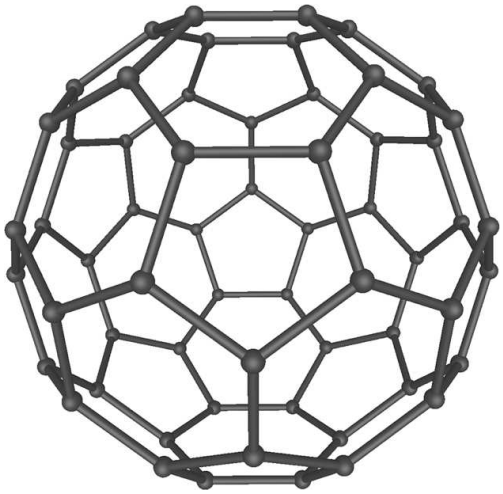

Figure 2.3: A drawing of the structure of C_{60}. Figure copied from en.wikipedia, Wikimedia Commons.

At the time of their discovery, fullerenes were created by pulsed laser vaporization of graphite in a flow of high density helium gas. The carbon-helium gas was expanded in a supersonic molecular beam into vacuum and then ionized by an excimer laser for detection in a time of flight (TOF) setup. Five years later Krätschmer *et al.* [46] found a way to produce bulk amounts of C_{60} and C_{70} by placing two rods of graphite in an atmosphere of helium and evaporating them by burning an electric discharge between them. The graphite rods are slowly consumed and fullerene-containing soot is formed. The fullerenes can be separated out using chromatographic methods. The production methods have continued to develop and various sizes of purified fullerenes can now be bought for a comparably low price.

Before the discovery of the fullerenes two types of pure carbon were known; diamond and graphite. In the diamond structure carbon atoms are arranged

in regular tetrahedrons which makes diamond a very hard but brittle material. Graphite on the other hand consists of sheets of carbon atoms arranged in a hexagonal structure within a sheet and with three of the four valence electrons through sp^2 hybridization making up strong covalent bonds. The remaining valence electron is delocalized and free to wander between the sheets, which are held together by weak forces. The individual sheets are very strong, but the bonds between the sheets can be easily broken, *e.g.* when writing with a graphite containing pencil.

The bonding in fullerenes is similar to the sp^2 hybridization of the carbon atoms in graphite, which makes the fullerenes stable but not entirely unreactive. The cage-form of the fullerenes puts strain on the bonds which have an energy minimum as a planar structure, *i.e.* as graphite. However, dangling bonds at the edges that would be the result of flattening a fullerene of finite size would increase the ground state energy too much to be a possible naturally occurring isomer. At the present time we know of two additional types of materials consisting of only carbon atoms; graphene and carbon nanotubes. Graphene is the name of a single sheet making up graphite. The first practical realization of producing this single sheet was made by Novoselov and Geim *et al.* (see *e.g.* ref [47]) for which they received the Nobel Prize in Physics 2010. The carbon nanotube consists of one or several walls of rolled up graphene sheets with or without an end cap. The experimental discovery of this structure was made by Iijima in 1991 [48].

Fullerenes have positive electron affinities. Through laser photodetachment in a storage ring experiment the electron affinity for C_{60} was measured to be 2.666 ± 0.001 eV and for C_{70} to be 2.676 ± 0.001 eV [49]. In 2005 the electron affinity of C_{60} was revisited by Wang *et al.* [50] and was found to be slightly larger, 2.683 ± 0.008 eV, as determined by first cooling the ions in a cold trap and then by performing vibrational resolved photoelectron spectroscopy. Their positive electron affinity, their stability (the energy barrier for fragmentation and carbon dimer emission is about 11 eV [51]), and the relative ease with which they can be vaporized and injected into vacuum have all contributed to making especially C_{60} a widely used 'test-molecule' in experiments, apart from the experiments concerned with revealing fundamental properties of the molecule itself.

There have been numerous applications suggested for fullerenes, but only a small fraction have yet been realized. Some of the suggested applications for fullerenes include using them as a starting material for diamonds and nanotubes, or as precursors for chemical vapor deposition (CVD) diamond films, in solar cells, as catalysts, as lubricants, and in medicine [52].

2.2.2 Large carbon-containing molecules

Porphyrins are a group of organic compounds, many naturally occurring. The common structure in all porphyrins is the central carbon ring consisting of 20 carbon atoms and four nitrogen atoms. Additional atoms and groups can then be added on to this base. One of the best known types of porphyrin is heme, the pigment in red blood cells. It contains an iron atom attached to the four nitrogens in the center of the ring.

The type of porphyrin studied in this thesis is the anionic species of 5,10,15,20-Tetrakis[4-(tert-butyl)phenyl]-21H,23H-porphine, molecular structure $C_{60}H_{62}N_4$, hereafter referred to as H_2tBTPP.

Phthalocyanines are a group molecules closely related to the porphyrines. They have the same type of central ring structure but have four of the carbon molecules replaced by nitrogen atoms. Without substitutions the phthalocyanines absorb in the wavelength region of $600 - 700$ nm and thus appear as green or blue. The porphyrines are often used as dye molecules. Depending on the type of central atom they can absorb in different regions of the visible spectra. Because of this property thin films of various phthalocyanines are studied for applications in organic solar cells (see *e.g.* [53]).

The type of phthalocyanin studied here is zinc phthalocyanine, molecular structure $C_{32}H_{16}N_8Zn$, hereafter referred to as ZnPc. A sketch of the two molecules in their optimized zero energy geometry as calculated with *Gaussian* [54] are shown in figure 2.4.

The electron affinity (Φ) for ZnPc has been measured in thin films yielding a value of 3.34 eV [55] but the value for free molecules is predicted by molecular orbital calculations to be 3.8 eV [56] and it is this predicted value that has been used in the calculations in Chapter 6.2.2. The vibrational levels of ZnPc have been studied with high level density functional theory (DFT) [57] and through a harmonic oscillator (h.o.) approach we deduce the caloric curve. This was compared to a more automated and simpler approach of calculating the vibrational levels (*Gaussian* [54]). For medium temperatures the two methods give very similar results for the heat capacity; 12.7 meV/K from the DFT-method as compared to 13.0 meV/K from *Gaussian* (at T=1600 K, which is the approximate emission temperature calculated in Chapter 6.2.2), corresponding roughly to a dimensionless C_v of 150.

The electron affinity of H_2tBTPP is estimated it to be the same as the electron affinity of H_2TPP, which has been found through experiments on the gas phase molecule to be 1.69 eV [58]. H_2TPP has the same central atomic structure as H_2tBTPP but is smaller and has four hydrogen atoms replacing the four tertiary butyl substitution groups (the four C_4H_9) at the end of each benzene ring.

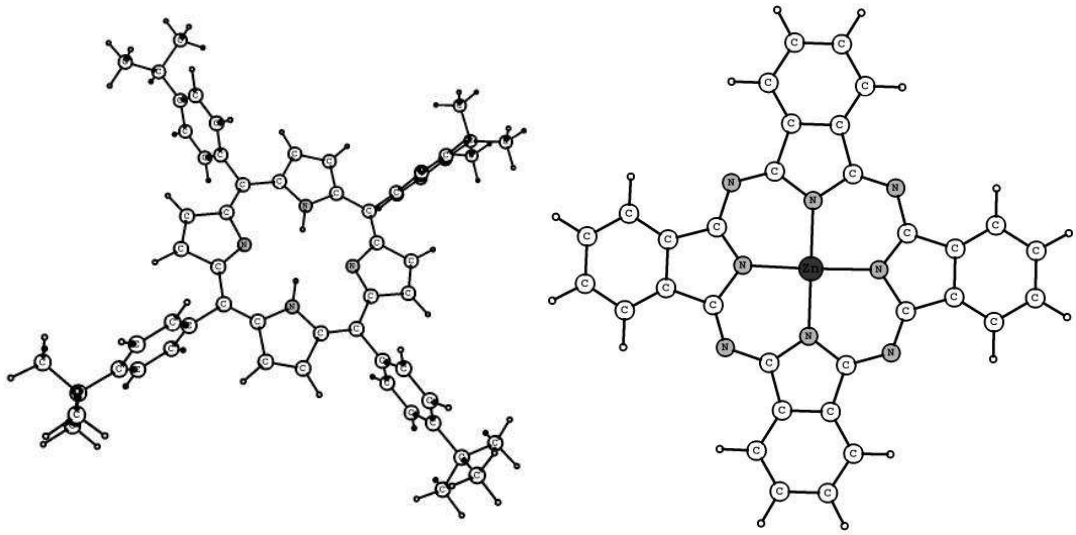

Figure 2.4: The two types porphyrin molecules studied. To the left is a figure illustrating the optimized zero energy geometry as calculated with *Gaussian* [54] for H_2tBTPP and to the right is the same for ZnPc. Note that the length scales are different in the two drawings.

The vibrational levels of this molecule were also calculated using *Gaussian* and the caloric curved deduced. No literature values for the full vibrational structure of this molecule were found to compare this to. The heat capacity using the same h.o. approach was found to be 22 meV/K at $T = 800$ K (the relevant emission temperature was found through a similar calculation as for ZnPc) which corresponds to a dimensionless C_v of 250.

2.2.3 Small carbon molecules

Small carbon clusters and molecules have attracted a lot of interest for several decades because of their appearance in nature and their rich and varying chemistry [59, 60]. Because of the flexibility of the carbon atom to create stable single, double, and triple bonds with its neighbors, a variety of structures can spontaneously appear from hot sources. In experimental settings the preferred structure of the smallest carbon molecules C_n with $n = 2 - 9$ appears to be linear, although both calculations and some experiments indicate that the even number species $n = 4, 6$, and 8 have both linear and cyclic configurations [60].

Anionic carbon molecules are also well studied, motivated partly by their recent detection in space. First out was C_6H^- in 2006 which was found in the molecular shell of the evolved carbon star IRC +10216 and in the rich molecular cloud TMC-1 in the Taurus complex of dark nebulae. The ion was identi-

fied by the match between the detected signal and its rotational bands mapped out in the laboratory [61]. Shortly thereafter detection of C_4H^- and C_8H^- followed [62]. As yet, no pure anionic carbon species has been detected in outer space as far as I know, but the knowledge of this field is rapidly growing as laboratory experiments become better and better at providing spectra to be compared to astrophysical data.

The small carbon molecule studied in this thesis is C_5^-. It is a linear molecule with cumulenic bonding, giving bond lengths of 1.309 Å (inner) and 1.296 Å (outer) [63], see figure 2.5 for a schematic illustration of the molecule. The anion has an electronic ground state configuration of $^2\Pi_u$ and the neutral C_5 has an electron affinity of 2.839 eV, as determined experimentally by photoelectron spectroscopy [64]. Small carbon molecules exhibit an odd-even effect in electron affinity where the odd numbered molecules have considerably higher affinity due to the ground electronic state ($^1\Sigma_g^+$) of the neutrals.

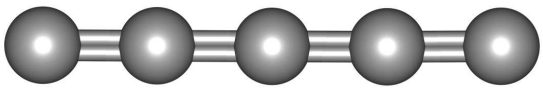

Figure 2.5: A schematic drawing of C_5. The double bonds in the cumulenic bonding are illustrated by the two bars between the carbon atoms.

CHAPTER 3

Experimental techniques and equipment

This chapter will give some information and background to the experiments and the experimental equipments and techniques used in the experiments described later in this thesis.

3.1 Cluster sources

The production method chosen depends highly on the type and size of the cluster systems desired. Highly stable and non-reactive clusters, such as many members of the fullerene-family, are often produced away from the analysis equipment, and can be stored for a long period of time. The majority of clusters however, will not survive a storage period in a jar or solution and must be studied immediately after production.

3.1.1 Corona discharge

Water clusters are examples of shortlived clusters that cannot be stored or moved around outside vacuum without changing their composition or falling apart. The clusters must thus be produced inside a vacuum chamber or immediately be led into one to be studied. The source used in the experiments covered in this thesis is called a corona discharge cluster source. When a potential gradient is large enough in a neutral medium (*e.g.* air) the medium will become ionized and create a plasma around the electrode [65]. If the electrode has a sharp point the potential does not have to be extremely high for the gradient to become very large locally around the tip. This region of ionized medium around the electrode is called a corona.

The source consists of a discharge needle and an optionally heated capillary normally used as an interface for an electrospray source. The discharge needle is placed in ambient air about $3 - 5$ mm from the capillary inlet, and raised to

a potential of $2-4$ kV relative to the capillary. Energy transferred to the ions from the plasma when corona discharge is performed at atmospheric pressure is only about $3-5$ eV [65] and is thus a quite gentle method of ionization. What type of ions are produced depends on the polarity and shape [66] of the needle.

The ions are produced in ambient air and will encounter neutral molecules on their way to the capillary. Charge exchange due to difference in electronegativity can occur here. Because of the polar nature of the water molecule, it will feel an effect from the charge and cluster around the ions, and thus shield the ions from further charge exchange. This clustering is more prominent for positive ions [65], but occurs also for negative ones. The charge reduces the critical size of the cluster, reducing the vapor pressure needed for supersaturation and clustering. The clusters will keep growing until they reach the capillary, see figure 3.1 for a schematic drawing of the experimental setup.

The capillary is 10 cm long with an inner diameter of 0.4 mm and serves as the gate into the first chamber of the vacuum system which has a pressure of 1 mbar. When interest lies in investigating only the ions produced, the temperature of the capillary is raised enough to evaporate all of the water coverage (as in many electrospray experiments with *e.g.* biomolecules where the temperature of the capillary in the apparatus used in the experiments in this thesis is set to about $T \approx 150$°C), but one can also control the cluster size distribution by tuning the temperature to keep an appropriate number of water molecules, see figure 2 in Paper I. Temperatures used for the capillary in these experiments were between $26-60$°C, where the highest temperature gives the smallest average cluster size.

In two of the experiments described in this thesis the objective was to create mixed clusters containing water and ammonia, or water and heavy water. When studying mixed ammonia and water clusters the ammonia molecules are mixed in with the water molecules in the gas around the needle through a setup where air is bubbled through a water and ammonia solution before entering the corona discharge area. The ammonia is contained to a small volume around the needle using a small cylindrical inclosure. The ammonia content in the clusters is varied by regulating the fraction of air going through the bubbling flask.

A slightly different setup was used in the experiment concerning mixing in deuterated water with regular water. Water clusters are produced in the same manner as the pure protonated water clusters but after passing through the capillary the clusters go into an octopole which is flooded to ca $3 \cdot 10^{-2}$ mbar with deuterated water vapor pressure. Low energy collisions take place and heavy water becomes incorporated in the clusters.

3.1.2 Laser desorption

The cluster source used for the carbon anion experiments described in Chapter 6 is of a quite different nature than for the production of water clusters. Commercially produced fullerenes, ZnPc, and H_2tBTPP are easily accessible and can be stored in powder form. Laser desorption was used to evaporate and ionize the molecules.

Already synthesized C_{60}, ZnPc, and H_2tBTPP-molecules are prepared as a film on a substrate and placed on a sample holder connected to the storage ring. The film is then irradiated with the fourth harmonic of a pulsed Nd:YAG laser (5 ns duration; New Wave Research, MiniLase II-30) [67] while being rotated slowly to maintain a fresh irradiation surface. The fast ions will immediately escape from the surface. The slow desorbed ions are extracted after a few μs using a pulse of ± 1.0 kV and 8 μs duration applied to the sample holder. To further accelerate them a DC voltage of ± 14.1 kV is applied. The system is designed to reduce the energy spread in the ions.

The laser desorption source was also used in the experiment on C_5^-. In the case of the small carbon clusters a graphite rod is ablated by the Nd:YAG laser without cooling gas and accelerated in the same manner as the above mentioned molecules.

3.2 Linear accelerator

Equipment which lets the charged particles pass every section only once before detection are called linear analyzers. That means that the paths taken by the particles do not overlap, and that the particles are in the experimental chamber a relatively short time before they are detected or lost. The Separator used in the experiments presented in this thesis is an example of such a system where the clusters are drawn into the chamber by an electric field. The beam is focused and accelerated, then mass selected in a magnetic field and flies freely in vacuum for a fixed distance before reaching a final analyzing section connected to a detector. A schematic drawing of the setup can be seen in figure 3.1.

After the clusters have passed through the capillary and entered the first chamber with a pressure of about 1 mbar they pass through a skimmer into the next pumping region [68]. The pressure is further reduced to around 10^{-3} mbar and the low-energy clusters are directed through the chamber via an octopole beam guide into the next region where the pressure is reduced even further to about 10^{-5} mbar. Electrostatic lenses and an Einzel-lens assembly guide

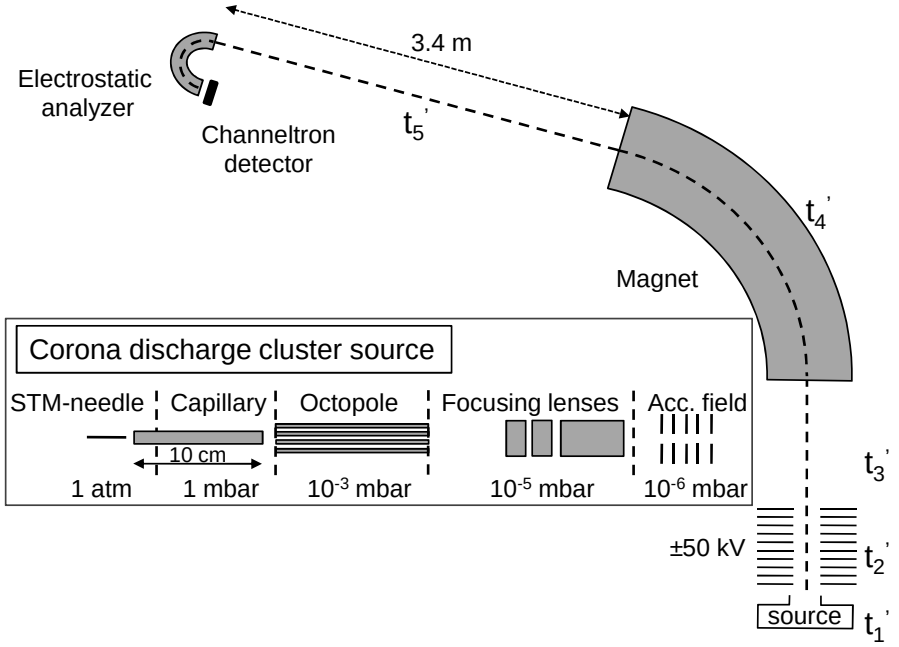

Figure 3.1: The experimental setup used for water cluster evaporation studies. The inset shows a magnified view of the corona discharge source, rotated $90°$. See text for details.

the clusters to the accelerating tube where the final pressure of 10^{-6} mbar is reached. A particle with a diameter of 1 nm (in the case of water clusters this corresponds to about 18 molecules) will collide on average with 0.13 restgas molecules when traveling a distance of 3.4 m in this pressure if a geometric cross section is assumed.

The entire cluster-production and beam guide-section is raised to the acceleration energy potential (in our case $U_{\mathrm{acc}} = 50$ kV) so the acceleration starts at the high energy and after 70 cm the potential is zero. The beam proceeds for 106 cm before reaching the mass selection magnet. The magnet has a bending angle of 72 degrees and a radius of 200 cm. The relation between the magnetic field B and particle mass m can be extracted from the centripetal force acting on the charged particle

$$\frac{mv^2}{r} = Bqv, \tag{3.1}$$

where v is the speed of the particle, q is its charge, and r is the radius of the magnet. Using the kinetic energy relation

$$U_{\mathrm{acc}} = \frac{W_{\mathrm{kin}}}{q} = \frac{mv^2}{2q}, \tag{3.2}$$

the speed can be eliminate from equation 3.1 and we obtain

$$\frac{m}{q} = \frac{(rB)^2}{2U_{\mathrm{acc}}}. \tag{3.3}$$

The mass selection magnet used in these experiments has a mass resolution of $m/\Delta m = 1000$. After running the experiments for a couple of hours the magnet gets rather hot and the practical upper limit for the magnetic field strength is about $B_{\max} \approx 1.2$ T, which at $W_{\text{kin}} = 50$ keV gives an upper mass limitation of about 5400 amu. By reducing the kinetic energy the mass can be increased, but this has implications for the mass resolution.

The charged particles then proceed for 3.4 m of free flight before reaching the hemispherical electrostatic analyzer [69] with a radius of 15 cm. The simplest kind of electrostatic analyzers consist of two curved parallel conductors that, when an electric field is applied between them, exert a radial force on the particle. The particle path bends inwards and depending on the kinetic energy either collides with the inner or outer wall, or has exactly the correct energy needed to pass trough the analyzer. Hemispherical in this context means that that there is also a field applied in the y-direction to focus the beam. Since the electrostatic analyzer separates particles according to energy and not mass, it does not have the same particle size limitations as a separation magnet and this has come to great use in *e.g.* electrostatic storage rings.

Experimental timescales

The time since creation of a cluster is of importance for the determination of temperatures, energies, rate constants and so on. In the separator there is a continuous stream of charged particles being created, accelerated, and detected. Figure 3.1 labels the different sections of the apparatus with t_1', t_2' etc. The times spent in the different sections are determined by the mass and charge of the particle, the distances traveled and the electric field strength acting on the charged particles. These are known quantities and the times are calculated through the velocities using the kinetic energy relation $E = mv^2/2$ together with the constant acceleration of the particles due to the electric fields ($s = v_0 t + \frac{1}{2}at^2$). The velocities scale mainly as $\sqrt{m}$ except for a small contribution due to the initial velocity of the clusters when entering the chamber.

The initial velocity is approximated with 330 m/s by estimating the velocity air will have when expanding into vacuum through the following reasoning. The thermal energy of a gas 'standing still' is $3k_BT/2$ (only counting the translational degrees of freedom, *i.e.* an ideal gas). The additional energy from the expansion (from 1 atm to perfect vacuum) is $1k_BT$ per molecule, so the total energy amounts to $5k_BT/2$. If we assume all this energy is transferred into kinetic energy we get

$$\frac{5k_BT}{2} = \frac{mv_{\max}^2}{2} \qquad \Rightarrow \qquad v_{\max} = \sqrt{\frac{5k_BT}{m}} \approx 660 \text{ m/s}, \tag{3.4}$$

with $m = 28.8$ amu (80% N_2 and 20% O_2) and $T = 300$ K. This is thus the maximum velocity the gas can get and as an average we have used $(v_{\max} - v_{\min}(= 0))/2 = 330$ m/s. In principle the maximum velocity can be higher because of transformation between the rotational energy of the air molecules to translational energy, but in this estimate we disregard this.

As an example of the timescales we have in the experiments, the times for a water cluster of $N = 50$ molecules are $t'_1 = 68$ μs (from entry into vacuum until acceleration), $t'_2 = 10$ μs (acceleration time), $t'_3 = 11$ μs (free flight between acceleration and mass selection in magnet), $t'_4 = 25$ μs (magnet transit time), and $t'_5 = 36$ μs (free flight). These times scale approximately with $\sqrt{m}$, but not exactly because of the small size-independent initial velocity.

3.3 Storage rings

Storage rings have proven to be a useful tool in investigating properties such as relaxation processes of atoms, molecules and clusters. In contrast to linear accelerators, storage rings lead the particles in turns through the apparatus and a stable charged particle could in the ideal case, with perfect vacuum and no other interactions, be kept in circulation forever.

Storage rings were first created in the 1930-40s in the subatomic community to facilitate better acceleration of particles, mainly relatively light ones such as protons or electrons. By circulating the particles several times through the accelerating section of a ring, each revolution would increase the kinetic energy of the particles. For bending the particle beam, magnets were used. When the need for even higher kinetic energies developed, the circumference of the rings had to be increased because of practical limitations in the magnetic field strength (see equation 3.1). When interest developed into studying larger particles such as free flying molecular ions and clusters in an intermediate kinetic energy regime, magnetic bending was no longer as practical because of power limitations of the magnets and the requirement of large facilities to contain such large apparatus. Instead, electrostatic deflectors and quadrupoles were put to use in the first electrostatic storage ring ELISA at the University of Aarhus [70]. Since the ring beam path is independent of the mass of the particles, quite large molecules (*e.g.* biomolecules and larger clusters) can be studied in these types of rings.

The TMU E-ring at Tokyo Metropolitan University [67] was built after a design similar to that of ELISA with a circumference of 7.7 m. A drawing of the TMU E-ring can be seen in figure 3.2.

I will not describe the entire ring in detail, but instead give a more general

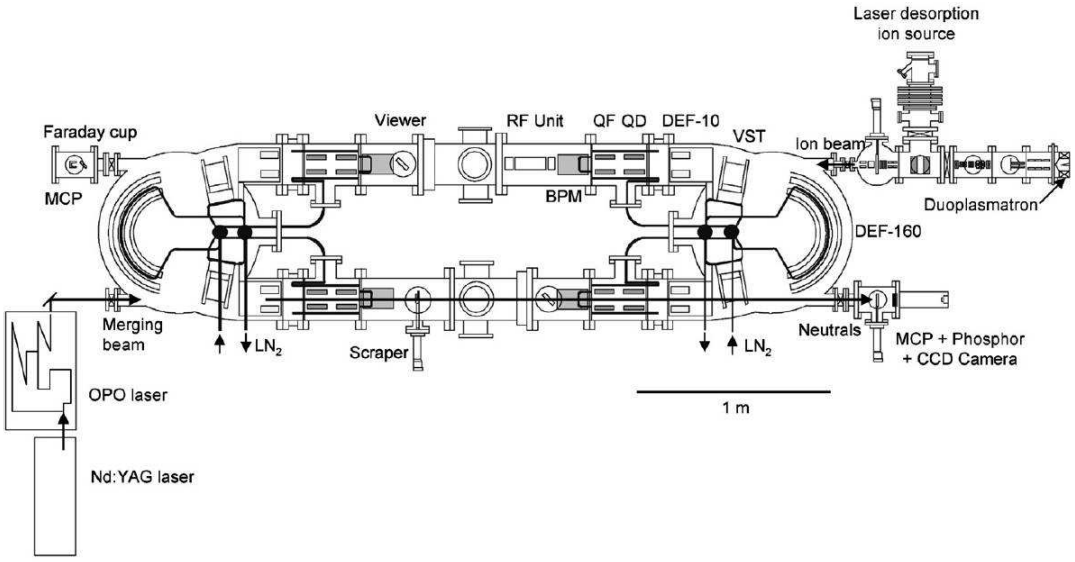

Figure 3.2: The TMU E-ring at Tokyo Metropolitan University. Figure copied from [67].

idea of what affects the circulating molecules and what is important for the experiments described later in this thesis.

The ions are prepared as described in section 3.1.2 and the ion beam enters the ring by passing through a 10° deflector (DEF-10). This deflector is run in synchronized pulse mode intended to chop up the beam in short bunches. Well inside the ring the ion-bunch follows the "race-track"-shaped path of the ring due to several deflectors and focusing and defocusing electrostatic quadrupole doublets. The ring also contains several diagnostic elements to monitor that the ions follow the right trajectory.

When the ion-bunch enters the ring one would like for the ions to follow exactly the same trajectory with the same velocity, and for the beam not to spread out over time. All ions with the same kinetic energy will follow the same trajectory in the ring, but if the mass is slightly different (*i.e.* isotopes) their velocities will be slightly higher or lower and the beam will spread out over time. To mass-select the beam further and minimize the spreading of the ion-beam kick-pulses can be applied. These are short high voltage pulses applied in-between two passes of the ion-bunch. Slower or faster ions will be deflected and not influence the rest of the measurements. In some cases several kick-pulses are necessary to get a good and clean beam, free from impurities.

Every 100 ms a new bunch of ions is let into the ring and immediately before that the old one is ejected. This is called dumping the beam and is done by turning off one of the deflectors for a time corresponding to one revolution of the ions in the ring.

There are mainly three reasons for loss of intensity in an ion beam. The ions can change their mass by losing an atom or molecule and consequently get a change in kinetic energy. The trajectory for the lighter ion will be different and the ions will eventually hit a wall. The ions can also collide with restgas inside the ring which might change their trajectories or fragment the particle. The final way, and the one exploited in the experiments reported here, is by losing its charge. These neutral particles can be detected, which will be covered in the following section.

3.4 Detection

The two setups described here use two different methods of particle detection. The storage ring at TMU is equipped with microchannel plate detectors (MCP) at the end of both straight sections of the ring. MCP's are arrays of $10^4 - 10^7$ miniature electron multipliers oriented parallel to one another [71]. The resistance between the front and the back of a plate is several MΩs and a voltage of typically around 1 kV is put over each plate. This setup allows high electron multiplication factors, time resolution in the order of < 100 ps, and a spatial resolution only limited by the channels' dimensions and spacing. When an energetic ion or particle hits the surface of the MCP it sputters away electrons which in turn create more secondary electrons and the resulting avalanche of electrons is finally detected through an anode as a current representing one particle count. For a higher multiplication factor, two or several plates can be connected in a cascade manner. An advantage of this type of detector is the ability to detect both neutral and charged particles, as long as they have a high kinetic energy. A possible disadvantage is that it does not discriminate against the detected fragments, *i.e.* we cannot tell if a molecular ion has lost an electron or a larger charged fragment in the setup at the ring.

The separator in Aarhus is equipped with a channeltron detector located directly after the hemispherical electrostatic analyzer. A channeltron works in a similar manner as one of the channels in an MCP but is larger in size. The geometry of a channeltron is often like a twisting horn, where the ions enter through the broad opening, hit the wall and create secondary electrons. A voltage of typically $2-3$ kV is applied over the channeltron, directing the electrons down the tube, resulting in more electrons when the secondary electrons hits the wall again and again. The resulting current of electrons is measured and the ions are counted.

3.5 Laser excitation

When studying cooling rates and relaxation processes in general it can be useful to be able to transfer a well defined amount of energy to the particle. This is often done with the help of lasers, as in the case of the carbon molecule-experiments described in this thesis. When a photon is absorbed by a particle the photon energy is taken up by the particle and it becomes internally excited.

By using pulsed lasers the fluence of photons can be concentrated to very short times and a very high density of photons can be achieved during the pulses but still keeping a low average power. There are laser systems that can produce pulses as short as tens of attoseconds (10^{-18} s), but the pulses used in the experiments presented here were several magnitudes longer, in the nanosecond (10^{-9} s) regime. To control the number of photons absorbed by the ions neutral density filters are used for laser pulse energy attenuation.

The laser system used in these experiments consists of an Optical Parametric Oscillator (OPO) pumped by a Nd:YAG laser. The tunable range of the OPO (Spectra-Physics, Quanta-Ray MOPO-HF) [67] is from 410 to 2200 nm (equivalent to $3.0 - 0.56$ eV). The photon energies used in the experiments in this thesis were between $1.85 - 2.8$ eV (visible light regime, $670 - 440$ nm), with a pulse energy of $0.5 - 5$ mJ, depending on the wavelength of the laser and the type of ion studied. The repetition rate of the laser is 10 Hz, set to coincide with the particle beam in one of the straight sections as is shown in figure 3.2.

CHAPTER 4

Theory of thermal decay

This chapter will give some theoretical background to the experimental results presented in the two following chapters. It will contain motivations and derivations of (some of) the equations used, and describe and expand upon the underlying assumptions that have been made. Its aim is also to connect the papers and the other results, and hopefully serve as a guide to a bigger picture of the evaporative ensemble and unimolecular decay. A lot of the material in this chapter can be found in a book of notes by Hansen [1], where it is described more rigourously and in more detail.

All systems tend to equilibrate with their environment. It is the 'zeroth' law of thermodynamics [72]. In a very small system, like an atom, the energy levels are well defined and lifetimes of specific excited states can be measured by tuning the excitation to the appropriate energy for excitation. In larger systems like molecules and clusters, there are numerous possible states the particle can be in with a given energy. Energy can transfer between different states and decay can occur through different relaxation process. An excited (or hot) molecule or cluster brought into a cold environment will eventually relax to a lower energy state (or cool down) by releasing some of its excess energy. In vacuum, equilibration through collisions is not an option for energy release. Instead the particle will release energy by unimolecular decay.

Unimolecular decay is the generic term for different types of energy release without interaction with an environment. Unimolecular decay consists of either evaporative cooling (fragmentation by releasing an atom, molecule, or larger moieties), thermionic emission (releasing one or several electrons), or radiative decay (emitting one or several photons). In the same system more than one of these unimolecular processes can occur at the same time, although usually with different rates.

4.1 Statistical decay channels

If a moderate amount of energy is transferred to a particle under timescales not too short, in terms of transition times between different states in the particle, the energy has time to couple to all degrees of freedom that are in the system. Energy release occurs then as a thermal (or statistical) process. The manner in which the energy is transferred to the particle; be it by photon absorption, from thermal contact to a hot surface, or through collisions with more energetic particles, makes no difference for a subsequent statistical release of energy. The particle has no memory of the excitation method after the energy has been dispersed amongst the degrees of freedom.

An often used theoretical description of the process of unimolecular decay comes from the principal of detailed balance, originally developed by Weisskopf [73] for the statistical emission of nuclei from a nucleus. The derivation now following is just one of many different ways of deducing decay constants of unimolecular decay. Depending on the type and size of the system studied, there might be better assumptions and approximations to be made.

The principle of detailed balance states that the rate for going from one state to another is the same as the rate of going in the opposite direction [74]. The rate is the rate constant times the population and the equality (when normalized) takes the form

$$\frac{\rho_{\text{final}}(E)}{\rho_{\text{final}}(E)+\rho_{\text{initial}}(E)}\,k_{\text{formation}} = \frac{\rho_{\text{initial}}(E)}{\rho_{\text{final}}(E)+\rho_{\text{initial}}(E)}\,k_{\text{decay}}, \tag{4.1}$$

where ρ_{final} is the level density of the final products after the decay and ρ_{initial} is the level density of the starting system. The final level density contains both the larger product particle and smaller emitted particle (or photon) and can be expanded to

$$\rho_{\text{final}} = \rho_{\text{fragment}}(\varepsilon_i)\,\rho_{\text{t}}(\varepsilon_t)\,\rho_{\text{daughter}}(E-E_a-\varepsilon_t-\varepsilon_i)\,\mathrm{d}\varepsilon_i\,\mathrm{d}\varepsilon_t, \tag{4.2}$$

where ε_i is the internal energy of the smaller emitted particle (fragment) and ε_t is its translational energy. Electron emission and particle evaporation is treated quite similarly with mainly differences in semantics (and of course numerical values).

If the fragment lost is an atom or a molecule, the larger particle is often referred to as the daughter, and it has a remaining energy that is the initial energy E minus the activation energy for emission E_a (often called the dissociation energy or activation barrier and referred to as D when specifically talking about particle dissociation) and minus the internal ε_i and translational ε_t energy of the fragment. The $\rho_t(\varepsilon_t)$ is the translational level density of the emitted fragment, usually just the kinetic energy.

When studying thermionic emission we have looked at the loss of an electron from a negatively charged molecule and then the remaining particle is often referred to as the neutral and the activation energy E_a is the electron affinity, labeled here Φ. The fragment lost (the electron) has no internal energy and consideration must only be given to its translational energy ε_t. In the case of photon emission as a cooling process the experimental situation is a bit different because it is very difficult to measure individual photons coming out of a low density of particles. Instead the easiest way of detecting radiative cooling in cluster science is by noting its effect on the other two types of unimolecular decay.

The three cases of unimolecular decay investigated experimentally in this thesis will now be discussed separately in more detail.

4.1.1 Fragmentation

Fragmentation entails both the loss of an atom or molecule, or larger parts of the cluster. In the case of water clusters spontaneous evaporation occurs one molecule at a time and it is not energetically favorable to lose larger moieties. For fullerenes the smallest unit of particle emission is the carbon dimer, C_2. Following a huge influx of energy during a short time, the cluster can explode and break apart completely, but this process is not described by detailed balance and is not what has been studied here.

The aim of this section is to deduce a practically useful expression for the decay constant k_{decay} to be able to relate it to experimental findings. We start with the opposite situation of fragment capturing. Imagine a particle (cluster or molecule) enclosed in a volume Ω. The mean rate constant for the particle to capture a fragment with a translational energy between ε_t and $\varepsilon_t + \mathrm{d}\varepsilon_t$ is

$$k_{\text{formation}}(E, \varepsilon_t)\,\mathrm{d}\varepsilon_t = \frac{\sigma(E - \varepsilon_t, \varepsilon_t)\,v}{\Omega}\,\mathrm{d}\varepsilon_t, \tag{4.3}$$

where $\sigma(E - \varepsilon_t, \varepsilon_t)$ is the capture cross section for the particle with resulting energy E and v is the velocity of the fragment, equal to $v = \sqrt{2\varepsilon_t/m}$. The rate constant for the reverse process of emitting a particle $k_{\text{decay}}\,\mathrm{d}\varepsilon_t$ is then according to equation 4.1 $k_{\text{formation}}$ divided by the level density of the parent particle (ρ_{parent}) multiplied by the number of states into which the parent particle can decay. This number is the level density of the daughter particle (ρ_{daughter}) times the number of states in volume Ω available for the fragment within the energy interval between ε_t and $\varepsilon_t + \mathrm{d}\varepsilon_t$, which is

$$\rho_{\text{fragment}} = \frac{\Omega\, m\, g_d}{2\pi^2\hbar^2}\sqrt{2\varepsilon_t m}\,\mathrm{d}\varepsilon_t, \tag{4.4}$$

where g_d is a degeneracy factor of the electronic states with a value depending on the specific kind of fragment. g_d is typically on the order of unity, *e.g.* for the carbon dimer it is either $g_d = 1$ (ground state and some of the excited states) or 3 (the other excited states) [75]. We get for k_{decay}

$$\begin{aligned} k_{\mathrm{decay}}(E,\varepsilon_t)\,\mathrm{d}\varepsilon_t &= k_{\mathrm{formation}}\frac{\Omega\, m\, g_d}{2\pi^2\hbar^2}\sqrt{2\varepsilon_t m}\,\frac{\rho_{\mathrm{daughter}}(E-D-\varepsilon_t)}{\rho_{\mathrm{parent}}(E)}\,\mathrm{d}\varepsilon_t \\ &= \frac{g_d\, m}{\pi^2\hbar^3}\,\sigma(E-\varepsilon_t,\varepsilon_t)\,\varepsilon_t\,\frac{\rho_{\mathrm{daughter}}(E-D-\varepsilon_t)}{\rho_{\mathrm{parent}}(E)}\,\mathrm{d}\varepsilon_t, \end{aligned} \quad (4.5)$$

where we see that the volume Ω disappears from the expression.

In the case of molecular evaporation, which is the case studied experimentally in this thesis in the water cluster experiments, the expression becomes somewhat more complicated due to the more complicated level density of the emitted fragment. Molecules can have energy deposited in both rotations, vibrations, and electronic excitations. Equation 4.2 can be divided into the specific contributions of different internal excitations in the level density in the following manner

$$\rho_{\mathrm{final}} = \rho_{\mathrm{r}}(\varepsilon_r)\,\rho_{\mathrm{v,el}}(\varepsilon_{v,el})\,\rho_{\mathrm{t}}(\varepsilon_t)\,\rho_{\mathrm{daughter}}(E-D-\varepsilon_r-\varepsilon_{v,el}-\varepsilon_t)\,\mathrm{d}\varepsilon_r\,\mathrm{d}\varepsilon_{v,el}\,\mathrm{d}\varepsilon_t, \quad (4.6)$$

where the subscripts r, v, and el refer to the rotational, vibrational, and electronic level densities of the fragment respectively. The vibrational energy and the energy deposited in electronic excitations for the fragment are combined into one parameter. If the ratio of vibrational and electronic frequencies to the daughter temperature is sufficiently high, which will be the case for water, these states are not excited so this level density is set to unity. Here it is assumed that we can in fact parameterize the level density in this way, which may not always be the case. Including this parametrization of the final level density from equation 4.6 in the expression for the decay constant we get

$$\begin{aligned} k_{\mathrm{decay}}(E,\varepsilon_t,\varepsilon_r)\,\mathrm{d}\varepsilon_t\,\mathrm{d}\varepsilon_r = \frac{g_d\, m}{\pi^2\hbar^3}\,\sigma(E-\varepsilon_t,\varepsilon_t)\,\varepsilon_t\,\rho_{\mathrm{r}}(\varepsilon_r)\,\times \\ \frac{\rho_{\mathrm{daughter}}(E-D-\varepsilon_t-\varepsilon_r)}{\rho_{\mathrm{parent}}(E)}\,\mathrm{d}\varepsilon_t\,\mathrm{d}\varepsilon_r, \end{aligned} \quad (4.7)$$

where the fragment level density left is the one pertaining to the rotational energy. The energies ε_t and ε_r deposited into the level densities of the fragment are subtracted from the level density of the daughter cluster.

Assuming that ε_t and ε_r are much smaller than the final internal energy of the cluster or molecule lets us expand the logarithm of the level density in these variables. This is not a huge assumption since for evaporation to occur at all some amount of excess energy needs to be present in the cluster. ε_t and ε_r are

in the following derivation expressed as a generic ε_x

$$\begin{aligned}
&\exp\left(\ln\left[\rho_{\text{daughter}}(E-D-\varepsilon_x)\right]\right) \\
&\quad\approx\quad \exp\left(\ln\left[\rho_{\text{daughter}}(E-D)\right]-\frac{\partial\ln\left[\rho_{\text{daughter}}(E-D-\varepsilon_x)\right]}{\partial\varepsilon_x}\,\varepsilon_x\right) \\
&\quad=\quad \rho_{\text{daughter}}(E-D)\,e^{-\frac{\partial\ln\left[\rho_{\text{daughter}}(E-D-\varepsilon_x)\right]}{\partial\varepsilon_x}\,\varepsilon_x} \\
&\quad=\quad \rho_{\text{daughter}}(E-D)\,e^{-\varepsilon_x/k_BT_{\text{daughter}}}, \qquad (4.8)
\end{aligned}$$

where the definition of the microcanonical temperature T_{daughter} (from now on shortened to T_d) has been used in the exponent in the final step of equation 4.8.

The expression for k_{decay} in equation 4.7 can now be integrated with respect to ε_t and ε_r. Integration over a Boltzman factor times the level density is equal to the canonical partition function Z and this is applied to the rotational level density of the fragment.

The translational energy ε_t is treated separately. If we for simplicity assume the capture cross section to be independent of the kinetic energy of the fragment we can perform the integral over the factors in k_{decay} dependent on translational energy as

$$\int_0^{E(\sim\infty)}\varepsilon_t\,e^{-\frac{\varepsilon_t}{k_BT_d}}\,\mathrm{d}\varepsilon_t=(k_BT_d)^2\int_0^{E(\sim\infty)}\frac{\varepsilon_t}{k_BT_d}\,e^{-\frac{\varepsilon_t}{k_BT_d}}\,\mathrm{d}\left(\frac{\varepsilon_t}{k_BT_d}\right)=(k_BT_d)^2, \qquad (4.9)$$

where we again use the approximation that the final daughter energy is much larger than ε_t. Putting the results together from equations 4.8 and 4.9, equation 4.7 becomes

$$k_{\text{decay}}(E)=\frac{g_d\,m}{\pi^2\hbar^3}\,\sigma(E)\,(k_BT_d)^2Z_{\text{r}}(T_d)\,\frac{\rho_{\text{daughter}}(E-D)}{\rho_{\text{parent}}(E)}. \qquad (4.10)$$

The difference between the daughter and parent level density is equivalent to the number of degrees of freedom that the fragment has [75], here labeled s, so

$$\frac{\rho_{\text{daughter}}(E-D)}{\rho_{\text{parent}}(E)}\approx\left(\frac{\hbar\overline{\omega}_D}{T_d}\right)^s\frac{\rho_{\text{parent}}(E-D)}{\rho_{\text{parent}}(E)} \qquad (4.11)$$

where $\overline{\omega}_D$ is a typical frequency of the material around the bulk Debye temperature [76]. The numerical value of s depends on the type of fragment evaporating and the temperature of the cluster. When dealing with unimolecular decay not involving the loss of atoms or molecules (such as thermionic emission and radiative cooling) the level density of the parent and daughter can be taken to be approximately the same but evaluated at different internal energies.

We continue with expanding the logarithm of the ratio of the level densities (where the subscript is no longer necessary)

$$\begin{aligned}
\ln\frac{\rho(E-D)}{\rho(E)} &= \ln\rho\left(E-D\right) - \ln\rho\left(E\right) \\
&= \ln\rho\left(E-\frac{D}{2}-\frac{D}{2}\right) - \ln\rho\left(E-\frac{D}{2}+\frac{D}{2}\right) \\
&= \ln\rho\big(E-\tfrac{D}{2}\big) - \tfrac{D}{2}\frac{\partial\ln\rho\left(E-\frac{D}{2}\right)}{\partial E} + \big(-\tfrac{D}{2}\big)^2\tfrac{1}{2!}\frac{\partial^2\ln\rho\left(E-\frac{D}{2}\right)}{\partial E^2} + \big(-\tfrac{D}{2}\big)^3\tfrac{1}{3!}\frac{\partial^3\ln\rho\left(E-\frac{D}{2}\right)}{\partial E^3} + \ldots \\
&\quad - \left[\ln\rho\big(E-\tfrac{D}{2}\big) + \tfrac{D}{2}\frac{\partial\ln\rho\left(E-\frac{D}{2}\right)}{\partial E} + \big(\tfrac{D}{2}\big)^2\tfrac{1}{2!}\frac{\partial^2\ln\rho\left(E-\frac{D}{2}\right)}{\partial E^2} + \big(\tfrac{D}{2}\big)^3\tfrac{1}{3!}\frac{\partial^3\ln\rho\left(E-\frac{D}{2}\right)}{\partial E^3} + \ldots\right] \\
&= -D\frac{\partial\ln\rho\left(E-\frac{D}{2}\right)}{\partial E} - \frac{D^3}{24}\frac{\partial^3\ln\rho\left(E-\frac{D}{2}\right)}{\partial E^3} + \mathcal{O}\left(\left(\frac{D}{2}\right)^5\right) \\
&\approx -\frac{D/k_B}{(T_p - D/2C_v)} - \frac{D^3/k_B}{12C_v^2(T_p-D/2C_v)^3} \\
&= -\frac{D}{k_B(T_p-D/2C_v)}\left(1+\frac{D^2}{12C_v^2(T_p-D/2C_v)^2}\right), \qquad (4.12)
\end{aligned}$$

where T_p is the microcanonical temperature of the parent cluster at the initial excitation energy E and C_v is the heat capacity of the cluster. The emission temperature T_e is identified with the last line in equation 4.12 as [77]

$$\begin{aligned}
-\frac{1}{k_BT_e} &= -\frac{D}{k_B(T_p-D/2C_v)}\left(1+\frac{D^2}{12C_v^2(T_p-D/2C_v)^2}\right) \\
\Longrightarrow T_e &\approx T_p - \frac{D}{2C_v} - \frac{D^2}{12C_v^2T_p}. \qquad (4.13)
\end{aligned}$$

If only the first two terms on the right side of equation 4.13 are included the emission temperature is approximately the midpoint between the parent temperature (T_p) and the daughter temperature ($T_d = T_p - D/C_v$), if the heat capacity C_v can be considered constant for the N and $N-1$ clusters. This approximation is in most cases sufficient.

With identifying $\hbar\omega_D \equiv T_D$ as the Debye temperature, everything in front of the last exponential is combined into one variable ω, as

$$\omega = \frac{g_d\, m}{\pi^2\hbar^3}\,\sigma(E)(k_BT_d)^2\left(\frac{T_D}{T_d}\right)^s Z_{\mathrm{r}}(T_d) \qquad (4.14)$$

which give us the familiar Arrhenius expression for the decay rate constant

$$k(E) = \omega e^{-D/k_BT_e} \approx \omega\exp\left[-\frac{D}{k_B(T_p-D/2C_v)}\right] \qquad (4.15)$$

were ω is the Arrhenius frequency factor with dimension $1/t$. This factor is sometimes also labeled A or ν in the literature. When the Arrhenius expression is used hereafter the temperature in the exponent is the emission temperature, unless otherwise stated.

4.1.2 Thermionic emission

Thermionic emission is very similar to fragmentation in the sense that both cases involve particle emission. The rate constant can also be expressed with the expression in equation 4.5. The difference between losing an atom or molecule or losing an electron lies mostly in the difference in capture cross section and mass of the emitted fragment. A geometrical cross section, such as the one presented in equation 5.1, is often not a good measure of electron emission cross sections because of the assumption of energy independence.

Direct measurements of absolute capture cross sections for clusters are very difficult to obtain. Ideally one would want a size selected neutral beam of clusters with control over both yield and thermal and kinetic energy. Colliding this cluster beam with a beam of electrons of predetermined and variable kinetic energy and the ability to measure all possible products would give an accurate cross section. Instead one has to work around this. The attachment cross section for several sizes of sodium clusters was measured by Scheidemann *et al.* [78] by colliding a neutral beam with a spread of cluster sizes with an electron beam and ionizing the remaining clusters using a UV-laser after the collision to detect the unaffected clusters. The cross sections measured for collision energies lower than the dissociation energy of one Na-atom ($E_{\text{coll}} < 1$ eV) fit well to the Langevin cross section, which is proportional to the polarizability α_p of the cluster. It can be expressed as [77]

$$\sigma_L = \pi \sqrt{\frac{2\alpha_p e^2}{E_{\text{coll}}}}, \tag{4.16}$$

and thus decreases as the energy increases. When the collision energy exceeds 1 eV the cross section levels out to a fairly constant value proportional to the area of the cluster, but considerably larger than the purely geometrical cross section.

The electron emission cross section for C_{60}^- has been determined experimentally by a fitting procedure to neutralization spectra for several different energies [77] and an upper and lower limit was found to be $\sigma = 20 - 60$ Å^2. In the specific case of C_{60}^- the cross section does not differ much from the geometrical one, which falls within this region at about 50 Å^2 (with a radius of 4 Å). The Langevin cross section overestimates this value by a factor of ten and is calculated as $\sigma_L \approx 350$ Å^2 with $E_{\text{coll}} = 0.15$ eV and $\alpha_p = 82$ Å^3 by [77] (in Gaussian units).

Another difference is the degeneracy factor g_d which for electron emission is 2 due to the spin degeneracy. The dissociation energy (or activation energy) for particle emission is in the case of electrons either the ionization energy (for

emission from neutrals) or the electron affinity (for emission from anions). The decay rate constant k then becomes

$$k(E,\varepsilon)\,\mathrm{d}\varepsilon = \frac{2m_e}{\pi\hbar^2}\,\sigma(E-\varepsilon,\varepsilon)\,\varepsilon\,\frac{\rho_{\mathrm{daughter}}(E-\Phi-\varepsilon)}{\rho_{\mathrm{parent}}(E)}\,\mathrm{d}\varepsilon, \tag{4.17}$$

but, as in the case of fragmentation, expansions and integrations can be made, and the expression can be written in the same simple form as in equation 4.15.

4.1.3 Radiative cooling

When we consider radiative decay (or photon emission) from clusters we need to treat the level density of the photon a little different from that of an electron or atom. Photons are 'full-blown' quantum species and can not be treated semi-classically. The decay constant for radiative decay is [1]

$$k(E,\nu) = \frac{8\pi\nu^2}{c^2}\,\sigma_{\mathrm{meas}}(\nu)\frac{\frac{\rho(E-h\nu)}{\rho(E)}}{1-\frac{\rho(E-2h\nu)}{\rho(E)}}, \tag{4.18}$$

where $h\nu$ is the energy of the emitted photon. The cross section σ_{meas} is the effective cross section, including both absorption and stimulated emission of radiation. The expression in equation 4.18 can be simplified and approximated further but for that I refer the reader to reference [1].

This decay constant $k(E,\nu)$ looks quite similar to the decay constants for electron and atomic emission, but with one important difference. It contains no activation barrier for the emission of photons. This makes radiative decay a competing channel for cluster cooling even if the cross section for photon absorption might be quite small.

For clusters with large activation barrier for particle emission or alternatively for quite cold clusters, radiative decay is the dominating process. The cross over between for instance electron emission and radiative cooling depends on the specific type of cluster.

As mentioned in the introduction to this chapter, direct measurements of photon emission are difficult in a low density of free particles and the experiments described in this thesis will include indirect measurements of this process. Three different ways of analyzing and interpreting data regarding thermionic emission and radiative decay experiments will be presented in Chapter 6.

4.2 Cluster abundances and energy distributions

Clusters and large molecules form a bridge between atoms and the bulk material and investigations can be performed as to *e.g.* how collective properties develop with size. Concepts such as temperature cannot simply be adapted from the macroscopic definitions but need special attention.

When studying free flying clusters or molecular ions in vacuum in *e.g.* an accelerator, a trap, or a storage ring the particles need to be vaporized. The practical aspects of this is discussed in the experimental sections; here some physical and energetic aspects will be examined. In many cases the clusters are created and/or vaporized in a hot source of some kind and then brought into vacuum. A buffer gas can be used to equilibrate the clusters to a certain temperature before injection into vacuum, but even without the buffer gas the clusters are likely to collide with each other. The ensemble of molecules or clusters can then be described by canonical quantities since the particles have access to a heat bath which allows a constant temperature to be kept. The temperature is thus a well defined quantity. Once the particles are transferred into the vacuum system they become effectively isolated and, if we disregard the different unimolecular cooling mechanisms, they would retain the excitation energy they had when entering the vacuum. The excitation energy is thus well defined and the particles are now best described by microcanonical quantities. The temperature to use is the microcanonical temperature already used in the decay rate constant derivation above, the inverse of the derivative of the logarithm of the level density with respect to energy of the particle, $1/k_BT \equiv d\ln(\rho(E))/dE$.

Another way of looking at the situation is that if you have a fairly large cluster, the internal energy will be dispersed between many degrees of freedom. The likelihood of the concentration of energy in a single degree of freedom is thus small and the cluster can sustain a high internal excitation energy without a reaction, such as the release of an electron or fragment, taking place. With the other degrees of freedom as a heat bath, one can then define a canonical temperature where the excitation energy of the cluster is considered as an average energy [79]. However, as also stated by Andersen *et al.* [79], an isolated system is fundamentally different from a system in thermal equilibrium with the surroundings and the natural way of describing it is through microcanonical quantities.

The concept of a microcanonical ensemble entails a conserved energy but a free excited cluster or molecule has a means of getting rid of excess energy through unimolecular decay. A modification of the microcanonical ensemble often referred to as the evaporative ensemble is then the appropriate nomenclature to use because it describes both the accurate initial energy distribution and its decay.

One aspect of the evaporative ensemble is that there exists a highest sustainable temperature of a cluster or molecule and this temperature is determined by the experimental time (under the condition that the timescales are larger than $1/\omega$, which normally is a very short time). Depending on what kind of unimolecular decay we are studying and under which conditions the experiments are performed, the energy distributions are different. If we for instance have negative ions in a storage ring and study thermionic emission the ions are lost from the experiment when they neutralize. If we study evaporation of water clusters in a separator the clusters can lose molecules in a sequential manner and still be detected. We will here look at the energetics of the cluster distributions in three different settings; fragmentation in the small cluster limit, fragmentation in the large cluster limit, and thermionic emission.

4.2.1 Fragmentation in the small cluster limit

We start with the Arrhenius expression of the rate constant. The upper limit of the temperature containable within a cluster with N molecules and dissociation energy for the loss of one molecule from this cluster size D_N at time t can be expressed as

$$\omega e^{-D_N/k_B T_{\mathrm{e,\,max},\,N}} = \frac{1}{t} \qquad \Leftrightarrow \qquad T_{\mathrm{e,\,max},\,N} = \frac{D_N/k_B}{\ln(\omega t)}, \tag{4.19}$$

where $T_{\mathrm{e,\,max},\,N}$ here refers to the emission temperature as discussed previously. The parent maximum temperature is then $T_{\mathrm{p,\,max},\,N} = T_{\mathrm{e,\,max},\,N} + D_N/2C_{v,N}$. In the following derivation we will take differences between energies where this finite heat bath correction will cancel.

If the clusters are created with sufficiently high energy a lower temperature limit can also be defined. A sufficiently high energy means that the clusters have undergone at least one evaporation and thus that all clusters of a certain size N originate from evaporation from clusters of size $N+1$. Figure 4.1 shows a schematic illustration of the process, where the abundance of clusters of size N and $N+1$ as a function of energy is drawn. The hottest clusters in the $N+1$-distribution will lose a molecule and thereby lose an energy of about D_{N+1}. If the clusters are still hot they will continue to lose energy and molecules, but with a much decreasing rate. However, when clusters are small enough, one evaporation of a molecule will take with it so much energy (and thus also remove temperature) from the cluster that further evaporation will be strongly suppressed. The rate constants for two consecutive decays are thus very different in the small cluster limit [74].

The minimum temperature of a cluster of size N can thus be related to the highest temperature of the clusters of size $N+1$, and if expressed in energies

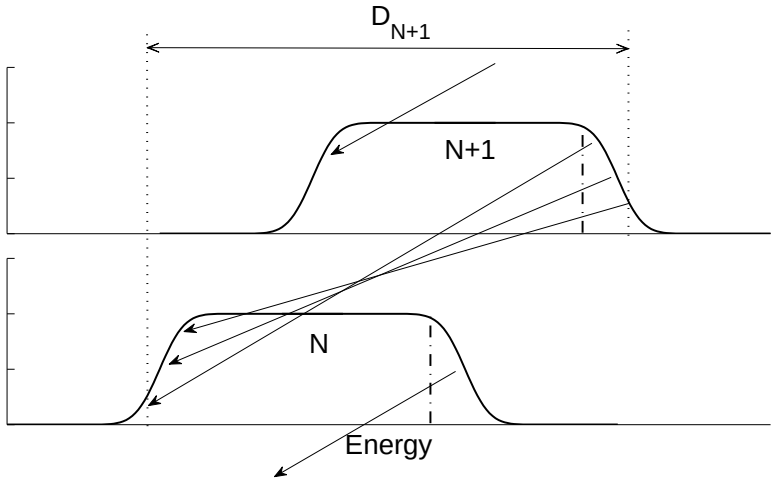

Figure 4.1: Schematic illustration of the small cluster limit evaporation systematics. The arrows represent clusters decaying and where they end up. Figure adapted from [1].

the relation is

$$E_{\min,\,N} = E_{\max,\,N+1} - D_{N+1}. \tag{4.20}$$

If the heat capacity $C_{v,N}$ can be regarded constant within a temperature interval of $\Delta T = D_N/2C_v$ so that the relation $dT/dE = 1/C_v$ is valid, the maximum energy of a cluster of size N is

$$E_{\max,\,N} = \frac{D_N C_{v,N}/k_B}{\ln(\omega t)} + E_{0,N}, \tag{4.21}$$

under the same assumptions as before, that all clusters originate from evaporation of a larger cluster size. The offset in energy, $E_{0,N}$, is due to a temperature dependence of the heat capacity which makes the energy not simply proportional to the temperature. This factor will approximately cancel in the following derivation as we take differences between energies.

The energy distributions for each cluster size thus have an upper and lower limit determined by the experimental time, dissociation energy, and heat capacity, with a width of approximately the dissociation energy D_N. If we assume that the difference in dissociation energy between two consecutive cluster sizes is negligible the decay rate of a specific cluster size is dependent on the heat capacity only. Measurements of spontaneous decay and survival fraction for such a distribution during a well defined time thus yield this size dependent heat capacity. The systematics of extracting these heat capacities will now be presented. The experimental setup is described in Chapter 3.2, and the results from measurements on heat capacity for protonated water clusters are presented in Chapter 5.1.2.

There are some different sections of the experiment with different times associated to them which are relevant to the heat capacity measurements. A schematic drawing of the experimental apparatus can be seen in Chapter 3.2, figure 3.1, and a discussion of how the times are calculated can also be found therein. The times referring to a specific section are labeled in the figure with a prime and the total times since creation are

$$t_n = \sum_{i=1}^{n} t'_i. \tag{4.22}$$

The first time t_1 is the time from creation of the clusters until mass selection. During this time the decay of a cluster will feed the smaller sizes and the width of the energy distribution remains unchanged. Mass selection takes place during $t_4 - t_1$ where evaporation leads to depletion from the high energy side of the distribution. After mass selection only a specific cluster size remains in the beam and during the remaining time t'_5 continues to evaporate. After time t_5 the clusters and their daughters (the ones that have evaporated during time t'_5) are detected and the survival yield measured.

The measured decay takes place during t'_5, and the decrease in the width of the energy distribution is

$$\begin{aligned} \Delta E(t_5) &= E_{\max,\,N}(t_5) - E_{\max,\,N}(t_4) = \frac{D_N C_{v,N}/k_B}{\ln(\omega t_4)} - \frac{D_N C_{v,N}/k_B}{\ln(\omega t_5)} \\ &\approx \frac{D_N C_{v,N} \ln(t_5/t_4)/k_B}{\ln(\omega t_4)^2}. \end{aligned} \tag{4.23}$$

The depletion of the cluster beam during the mass-selection time needs to be accounted for to get a correct normalization of the decay constant. The decrease of energy width during this time is

$$\Delta E(t_4) = E_{\max,\,N}(t_1) - E_{\max,\,N}(t_4) \approx \frac{D_N C_{v,N} \ln(t_4/t_1)/k_B}{\ln(\omega t_4)^2}. \tag{4.24}$$

At the detector we measure the surviving fraction P of cluster of size N during the time t'_5, which is proportional to the width of the energy distribution D_N subtracted by the loss of energy $\Delta E(t_5)$ and $\Delta E(t_4)$. Normalization is achieved by dividing with the loss of intensity during the mass selection time t_4 as

$$P \approx \frac{D_N - \Delta E(t_5) - \Delta E(t_4)}{D_N - \Delta E(t_4)} = \frac{1 - \frac{C_{v,N} \ln(t_5/t_1)/k_B}{\ln(\omega t_4)^2}}{1 - \frac{C_{v,N} \ln(t_4/t_1)/k_B}{\ln(\omega t_4)^2}}, \tag{4.25}$$

which can be used to extract the size-dependent heat capacities $C_{v,N}$ from the measurements of the survival fraction P, as

$$\frac{C_{v,N}/k_B}{\ln(\omega t_4)^2} \approx \frac{1 - P}{\ln(t_5/t_1) - P \ln(t_4/t_1)}. \tag{4.26}$$

One should note that because of the assumption of constant dissociation energies for two consecutive cluster sizes ($D_N = D_{N+1}$), this method will not describe features such as magic numbers in cluster abundances.

4.2.2 Fragmentation in the large cluster limit

The situation is different in the large cluster limit. When a cluster contains more than a few hundred vibrational degrees of freedom the microcanonical temperature change when losing one constituent is not large [80]. The assumption of very different decay constants for consecutive decays as in the case of small clusters is not valid. Instead, the temperature distribution for a given cluster size is quite narrow with an approximately Gaussian shape and the temperature can be estimated with a single T_N, the ensemble mean temperature. The energy distribution is instead wide as a consequence of the large heat capacity. At a given experimental time clusters with the same internal temperature can be observed containing a variable number of constituents.

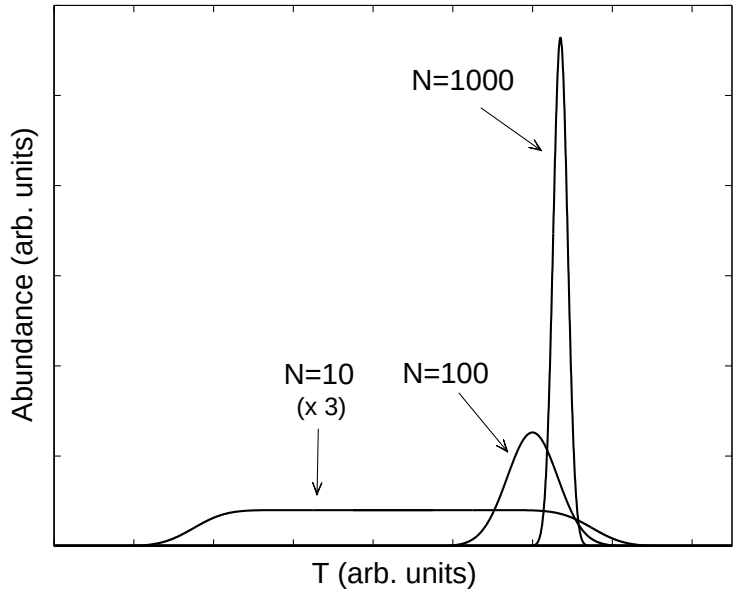

Figure 4.2: Schematic illustration of the small and large cluster temperature distribution after an experimental time of 1 ms. The figure is a drawn copy of a Monte Carlo simulation displayed in figure 5 of reference [80].

A Monte Carlo simulation of the temperature distribution of clusters of size $N = 10$, 100, and 1000 after a cooling time of 1 ms can be seen in figure 5 of reference [80]. Because it is a good illustration of the difference between small and large cluster systems a drawn copy of this figure is shown in figure 4.2.

Since the energy distribution is so wide for large clusters, we cannot define a maximum energy through the dissociation energy for a specific size cluster. The decay constant is thus not dependent on the dissociation energy. It is instead a function of the size of the particle through the heat capacity and can be written as

$$k_N \approx \frac{C_{v,N}/k_B}{\ln(\omega t)^2}\frac{1}{t}. \tag{4.27}$$

Derivations leading up to this expression can be found in several sources, see *e.g.* [1, 80, 81].

To relate the expression for the rate constant in equation 4.27 to the measurements performed on water clusters we use the experimental times again related to the separator described in Chapter 3.2. The last time for non-destructive decay is t_1 and the decay measured takes place during t_5'. The surviving cluster fraction measured after t_5' is then

$$P = e^{-k_N(t_1)(t_5')} = \exp\left(-\frac{C_{v,N}/k_B}{\ln(\omega t_1)^2}\frac{t_5'}{t_1}\right), \tag{4.28}$$

and we can solve for the heat capacity $C_{v,N}$ as

$$\frac{C_{v,N}/k_B}{\ln(\omega t_1)^2} = \frac{-\ln(P)}{(t_5')/t_1}. \tag{4.29}$$

4.2.3 Thermionic emission and radiative cooling

Thermionic emission and radiative cooling was studied in an electrostatic storage ring and here it will be shown how the theory of unimolecular decay is applied to an ensemble of clusters or molecules. We go back to the Arrhenius decay rate constant derived in section 4.1.2:

$$k = \omega e^{-\Phi/k_B T} \tag{4.30}$$

where Φ is the electron affinity. The decay rate constant is highly dependent on the temperature of the system and can essentially assume all values from $k = \omega$ when $T \to \infty$ to $k = 0$ when $T \to 0$. The temperatures that can be probed by decay are dependent on the timescales of the experiments, typical from a couple of μs to in some storage ring and trap experiments several seconds. The fraction of survived particles at time t can be expressed as

$$P = e^{-kt}, \tag{4.31}$$

and the decay rate at the same time is given by the integral of the surviving fraction times the decay rate constant and the energy distribution of the particles $g(E)$, as

$$R = \int_0^\infty g(E)k(E)e^{-k(E)t}\,\mathrm{d}E. \tag{4.32}$$

If a constant and energy independent distribution is assumed, $g(E) = g$, that factor can be taken outside the integral. We proceed with substituting the rate constant for the energy in the integral

$$R = g \int_0^\infty k e^{-kt} \left(\frac{dk}{dE} \right)^{-1} \mathrm{d}k = g \int_0^\infty e^{-kt} \left(\frac{d \ln k}{dE} \right)^{-1} \mathrm{d}k. \tag{4.33}$$

If the logarithmic derivative of the decay constant is a slowly varying function of the energy this factor can be evaluated at $k = 1/t$ where it peaks and taken outside the integral which gives us

$$R \approx g \left(\frac{d \ln k}{dE} \right)^{-1} \Big|_{k=1/t} \int_0^\infty e^{-kt} \, \mathrm{d}k = g \left(\frac{d \ln k}{dE} \right)^{-1} |_{k=1/t} \, \frac{1}{t} \int_0^\infty e^{-kt} \, \mathrm{d}kt, \tag{4.34}$$

and after evaluating the integral we get

$$R \approx g \left(\frac{d \ln k}{dE} \right)^{-1} \Big|_{k=1/t} \frac{1}{t}. \tag{4.35}$$

We continue by evaluating the energy derivative of $\ln k$ (and ignore the comparably weak energy dependence in ω)

$$\begin{aligned} \left(\frac{d \ln k}{dE} \right)^{-1} &= \left(\frac{d \ln \left(\omega \exp[-\Phi/k_B T] \right)}{dE} \right)^{-1} = \left(\frac{d \left(-\Phi/k_B T \right)}{dE} \right)^{-1} = \left(\frac{\Phi}{k_B T^2 C_v} \right)^{-1} \\ &= [\text{with } k = 1/t = \omega \exp(-\Phi/k_B T) \;\; \Rightarrow \;\; \Phi/k_B T = \ln(\omega t)] \\ &= \frac{C_v \Phi}{k_B \ln(\omega t)^2}. \end{aligned} \tag{4.36}$$

Combining equations 4.35 and 4.36 renders R as

$$R \approx g \frac{\Phi \, C_v / k_B}{\ln(\omega t)^2} \frac{1}{t}. \tag{4.37}$$

The decay rate thus follows essentially a $1/t$-decay curve with a minor logarithmic correction. NB, this correction is not due to competing processes such as radiative cooling. In Chapter 6.2.2 we will see a numerical example of simulated decay that fits well to this expression.

Usually there is a competition between radiative cooling and thermionic emission, where radiative cooling is seen in experiments as a quenching of the thermionic emission rate and a deviation from the $1/t$-decay. If the particle is very small emission of a single photon can cool the particle enough to be rendered inactive but in a larger system the emission can be considered as a continuous cooling process. The rest of this section will describe one way of extracting radiation properties by means of separating thermionic emission from radiative cooling.

In an ensemble of hot clusters or molecules, the particles with the highest internal energy are most likely to release their extra electron the quickest and the change in the maximum ensemble energy decreases due to this as $dE_m/dt \propto 1/[\ln(\omega t)^2 t]$. When energy decrease simultaneously occurs through a second channel (*e.g.* radiation) the thermionic emission will be quenched. This can be expressed by deriving a modified expression for the rate constant k which includes a time dependent energy term. By investigating the time development of the logarithm of the Arrhenius rate constant ($k = \omega \exp(-\Phi/k_B T)$) we get

$$\frac{d\ln(k)}{dt} = \frac{d}{dt}\left(-\frac{\Phi}{k_B T}\right) = -\frac{\Phi}{k_B}\frac{d}{dT}\left(\frac{1}{T}\right)\frac{dT}{dE}\frac{dE}{dt} = -\frac{\Phi}{k_B T^2 C_v}\dot{E} \equiv -\frac{1}{\tau}, \quad (4.38)$$

where τ is the radiative time, as defined by the expression above. $\dot{E}$ is the radiative power, *i.e.* the change in internal energy with time due to radiation, and we estimate that this change will follow a temperature dependence resembling that of black body radiation:

$$\dot{E} = \alpha T^n, \quad (4.39)$$

where α is related to the emissivity ϵ, the Stefan-Boltzmann constant σ_{SB}, the radiative area of the molecule A, and the temperature T through $\alpha = \epsilon\sigma_{SB}AT^{4-n}$ [82]. If the second derivative of $\ln k$ is also included we get an expression of k to the second order in time as

$$k \approx k_0 \exp\left(-\frac{t}{\tau} + \frac{n-2}{2}\frac{T}{\Phi}\frac{t^2}{\tau^2}\right), \quad (4.40)$$

where k_0 is the rate constant at time zero. A neutral spectrum $I(t)$ can then be fitted to an expression which also includes the radiative dependence in k

$$I(t) = \frac{a_0}{t\ln(\omega t)^2}\, e^{a_1 t + a_2 t^2}, \quad (4.41)$$

where we can make the identifications of a_1 and a_2 as

$$a_1 = -\frac{\Phi\alpha T^{n-2}}{k_B C_v} \equiv -\frac{1}{\tau} \quad (4.42)$$

and

$$a_2 = \frac{n-2}{2}\frac{1}{\tau^2}\frac{T}{\Phi} = \frac{n-2}{2}\frac{\Phi\alpha^2}{k_B^2 C_v^2}T^{2n-3}. \quad (4.43)$$

From experimental fits to a_1 and a_2 the power n on the temperature dependence in the radiative power can be extracted as

$$\frac{a_2}{a_1^2} = \frac{n-2}{2}\frac{T}{\Phi}, \quad (4.44)$$

where T/Φ is found from the relation $1/t = \omega \exp(-\Phi/k_B T_e)$. T_e is the emission temperature as before so the parent maximum temperature (before electron emission) is $T_m = T_e + \Phi/2C_v$.

From this, radiative cooling rates and emissivity can be extracted and practical examples of this will be given in Chapter 6.2.2. Parts of this description of thermionic emission and radiative cooling were also used in Paper III regarding cooling rates for C_{60}^- and in Paper IV where radiative cooling rates were deduced for C_5^-.

CHAPTER 5

Evaporation from water clusters

This chapter will present the experiments and some of the results from metastable evaporation (spontaneous fragmentation) of water clusters. The experimental setup of the Separator has been described in Chapter 3 and some background to the theory in Chapter 4.

All experiments on water covered by this thesis are carried out in a similar way and a general description will be given first. Then the results from three different experiments on three slightly different systems will be presented separately.

As already mentioned the charged clusters are created in a corona discharge source, guided through a capillary into the first vacuum chamber, and then successively enter chambers with lower and lower pressure. They are then accelerated (in these experiments to 50 keV), mass selected in a magnet, fly for 3.4 m, and are then electrostatically analyzed according to their kinetic energy and detected. The kinetic energy analysis serves as a mass analyzer in this case.

Depending on the temperature of the capillary and the potentials on the capillary, the needle, and the tube lens we can shift the cluster size distributions. The temperature effect of the capillary is shown in figure 2 of Paper I. High temperatures give small size clusters and vice versa. The capillary can only be heated, not cooled below room temperature.

The separator can be run in two different modes. Either the magnet is scanned and the analyzer is kept open to all clusters with the kinetic energy of 50 keV (an example is shown in figure 2.2 in Chapter 2.1.1). If the magnet is fixed on a magnetic field letting through a particular mass, the analyzer is scanned to register possible changes to this specific cluster size during the free flight. Figure 5.1 shows two analyzer scans of protonated water clusters of size $N = 40$ and $N = 17$.

Data analysis and corrections

The metastable evaporation is studied by fixing the magnetic field to allow the passage of a cluster of a certain m/q and then recording the difference in kinetic energy of the clusters after the free flight region by scanning the electrostatic analyzer. Figure 5.1 shows the evaporation spectra of two different size clusters; $N = 17$ and $N = 40$, for the protonated clusters.

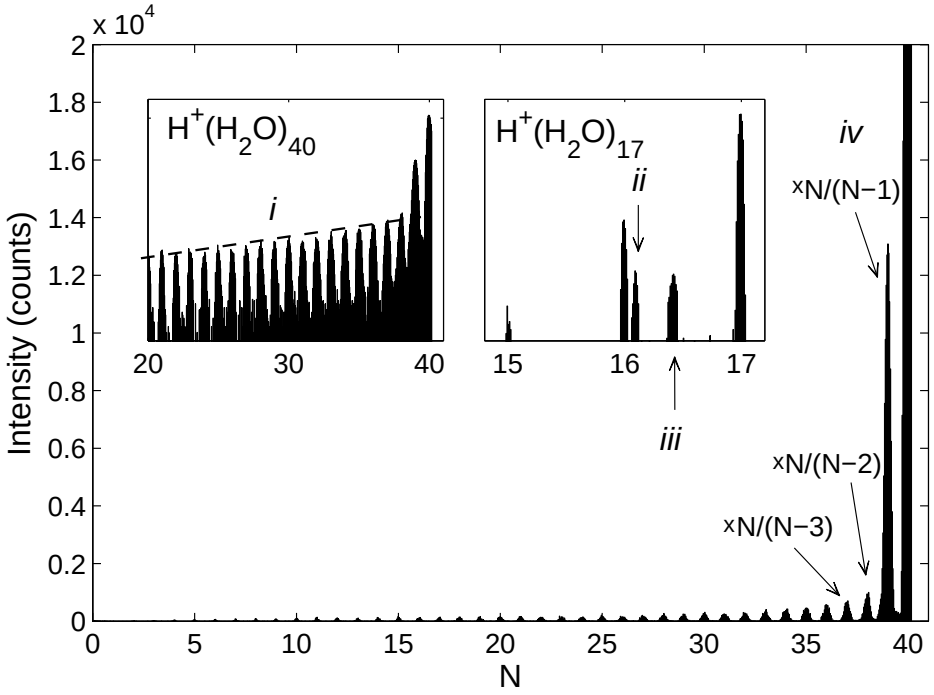

Figure 5.1: Evaporation of $H^+(H_2O)_{17}$ and $H^+(H_2O)_{40}$. The large frame shows the entire fragmentation chain on a linear scale for $N = 40$. Note that the y-axis is truncated for display purposes. The detection efficiency correction (*iv*) is written out for the first three daughter peaks but is applied to all of them. The inset to the left shows the same spectrum in logarithmic scale, where the line shows the intensity of the ions attributed to CID (correction *i*). The second inset shows the analyzer spectrum for parent cluster with $N = 17$ where correction *ii* and *iii* are labeled. See text for details.

There are some corrections to be made to the data, illustrated by the labeling (*i*)-(*iv*) in figure 5.1. The first one (*i*) is correcting for collision induced dissociation (CID), due to rest gas collisions in the free flight section. The dashed line is an illustration of the process, in reality the peaks are integrated before the subtraction is made. An exponential curve is fitted to the peaks originating from CID and is subtracted from the spontaneous evaporation peaks. In the case of $N = 17$ and $N = 40$ in figure 5.1 only the first daughter peak is attributed to spontaneous evaporation. Up to $N < 60$ we see only one daughter

peak originating from evaporation, for $60 < N < 160$ there are two daughter peaks, and for $160 < N < 300$ there are three.

The second correction (*ii*) to the evaporation spectra is due to evaporation in the first field free region, after acceleration but before mass selection by the magnet [83]. As was shown in Chapter 3, what particles go through the magnet depends on both mass and kinetic energy. If the magnet is set to pass a cluster with N water molecules then evaporation of a cluster of size $N + 2$ to a cluster of size $N + 1$ in the first field free region can have approximately the same apparent mass (m/q) as the desired cluster size N [83]. The kinetic energy is lower than for the cluster of size N and after the electrostatic analyzer, the peak will show up close to, or merged with, clusters of size $N - 1$. However, in the size region $10 < N < 23$ the two peaks are distinguishable and the ratio of the contribution from $H^+(H_2O)_{N+1}$ was determined to be $\approx 10\%$ of the first daughter peak. 10% of the counts in the first daughter peak are thus subtracted for $N > 23$.

The third correction (*iii*) that must be performed is clearly seen in the inset displaying $N = 17$ in figure 5.1. The relatively large peak between the parent peak and the first daughter peak is due to secondary ions released from the edge of the electrostatic analyzer when the parent ions are steered almost straight through. This peak wanders through the spectra with increasing N and is subtracted when merging with a daughter peak.

The fourth correction (*iv*) is due to the geometry and detection efficiency of the analyzing section. The radial force acting on the clusters due to the potential difference between the two plates in the analyzer is proportional to the kinetic energy of the clusters. When a cluster has lost n molecules the kinetic energy has been reduced to $(N-n)/N$ times the initial kinetic energy and it will travel with a reduced velocity. The potential difference between the two plates is scanned linearly with time so the clusters with lower kinetic energy than the initial one will be scanned faster than the parent by the factor $N/(N - n)$. We must therefor multiply the counts by $N/(N - 1)$ for the first daughter peak, $N/(N - 2)$ for the second *etc.* to compensate for this effect.

In Paper I, figures 3 and 4, examples of spontaneous evaporation spectra with both positive and negative clusters are shown for $N = 20$ and 225. There are no substantial differences between positive and negative clusters.

Frequency factor for water evaporation

The Arrhenius frequency factor $\omega = \frac{g_d\, m}{\pi^2 \hbar^3}\, \sigma(E)(k_B T_d)^2 \left(\frac{T_D}{T_d}\right)^s Z_{\mathrm{r}}(T_d)$ for water molecule emission from a water cluster enters into many calculations for different water properties. Here it will be calculated for H_2O, HDO, and D_2O. In

table 5.1 some useful properties of water are displayed. If not otherwise stated they are collected from the *CRC handbook of Chemistry and Physics* [84].

Table 5.1: Physical constants for water at $T = 0°\text{C}$ (when applicable) [84]

Parameter	Description	Value
ρ	density	$999.8\ \text{kg/m}^3$
K	dielectric constant	87.90
σ_s	surface tension	$75.64\ \text{mJ/m}^2$
$m_{\text{H}_2\text{O}}$	mass of H_2O	18.02 amu
m_{HDO}	mass of HDO	19.02 amu
$m_{\text{D}_2\text{O}}$	mass of D_2O	20.02 amu
T_D	Debye temperature	185 K [85]

From the density ρ and the mass of the water molecule m an equivalent spherical radius $r_1 = 1.92$ Å is extracted. We assume a geometrical cross section independent of energy:

$$\sigma = \sigma_N = \pi r_N^2 + \pi r_1^2 = \pi r_1^2 \left((N-1)^{1/3} - 1\right)^2 \approx \pi r_1^2 N^{2/3}, \tag{5.1}$$

where r_N is the radius of a water cluster containing N molecules. The electronic degeneracy factor g_d is unity since the two unpaired electrons from the oxygen atom combine with the two electrons from the two hydrogen atoms and form a closed electronic shell. The daughter temperature entering the expression for ω depends on the cluster size and is here estimated with the average value for daughter cluster with sizes between $N = 5 - 300$. It is calculated in the next section to be (on average for the cluster sizes measured in this thesis) $T_d = 163$ K. The degrees of freedom lost when one water molecule is evaporated from a cluster is approximately $s = 6$ (this will be shown in section 5.1.2).

The rotational partition function for a water molecule is calculated using the moment of inertia. The moment of inertia differs for the three isotopologues of water, with the values [86]

$$\text{H}_2\text{O} \begin{cases} I_x = 1.0220 \cdot 10^{-40} & \text{g cm}^2 \\ I_y = 2.9376 \cdot 10^{-40} & \text{g cm}^2 \\ I_z = 1.9187 \cdot 10^{-40} & \text{g cm}^2 \end{cases} \tag{5.2}$$

$$\text{HDO} \begin{cases} I_x = 1.2092 \cdot 10^{-40} & \text{g cm}^2 \\ I_y = 4.2715 \cdot 10^{-40} & \text{g cm}^2 \\ I_z = 3.0654 \cdot 10^{-40} & \text{g cm}^2 \end{cases} \tag{5.3}$$

$$\text{D}_2\text{O} \begin{cases} I_x = 1.8384 \cdot 10^{-40} & \text{g cm}^2 \\ I_y = 5.6698 \cdot 10^{-40} & \text{g cm}^2 \\ I_z = 3.8340 \cdot 10^{-40} & \text{g cm}^2 \end{cases} \tag{5.4}$$

From the moments of inertia of the respective molecules the rotational temperature is calculated as

$$T_{rot} = \frac{\hbar^2}{2Ik_B}. \tag{5.5}$$

This gives rotational temperatures for the three molecules as

$$\mathrm{H_2O} \begin{cases} T_x = 39.4 & \mathrm{K} \\ T_y = 13.7 & \mathrm{K} \\ T_z = 21.0 & \mathrm{K} \end{cases} \tag{5.6}$$

$$\mathrm{HDO} \begin{cases} T_x = 33.3 & \mathrm{K} \\ T_y = 9.43 & \mathrm{K} \\ T_z = 13.1 & \mathrm{K} \end{cases} \tag{5.7}$$

$$\mathrm{D_2O} \begin{cases} T_x = 21.9 & \mathrm{K} \\ T_y = 7.10 & \mathrm{K} \\ T_z = 10.5 & \mathrm{K}. \end{cases} \tag{5.8}$$

If the molecule is symmetric in some direction the rotational partition function must be divided with a so called symmetry number to avoid over-counting of the number of states. The symmetry number, denoted by σ_S, for H_2O and D_2O is equal to 2 whereas for HDO it is 1 (*i.e.* not symmetric). The expression for the rotational partition function as a function of rotational temperatures is

$$Z_{\mathrm{r}} = \frac{\pi^2}{\sigma_S} \left(\frac{T_d}{T_x} \frac{T_d}{T_y} \frac{T_d}{T_z} \right)^{1/2}. \tag{5.9}$$

A daughter temperature of $T_d = 163$ K renders the rotational partition function for the three molecules (H_2O, HDO, and D_2O) 96, 320, and 254. When including the mass and the rotational partition function this gives the following frequency factors

$$\omega_{\mathrm{H_2O}} = 3.1 \cdot 10^{17} N^{2/3} \ \mathrm{s}^{-1} \tag{5.10}$$

$$\omega_{\mathrm{HDO}} = 1.1 \cdot 10^{18} N^{2/3} \ \mathrm{s}^{-1} \tag{5.11}$$

$$\omega_{\mathrm{D_2O}} = 9.1 \cdot 10^{17} N^{2/3} \ \mathrm{s}^{-1} \tag{5.12}$$

An experiment on water evaporation from a cluster consisting of one ammonium ion and three water molecules of various degrees of deuteration will be discussed in section 5.3. Treating the ammonium ion in these clusters as a water molecule by using $N = 4$ in the expressions 5.10 to 5.12 gives the three frequency factors shown in figure 5.2, where they are plotted as a function of the daughter temperature T_d.

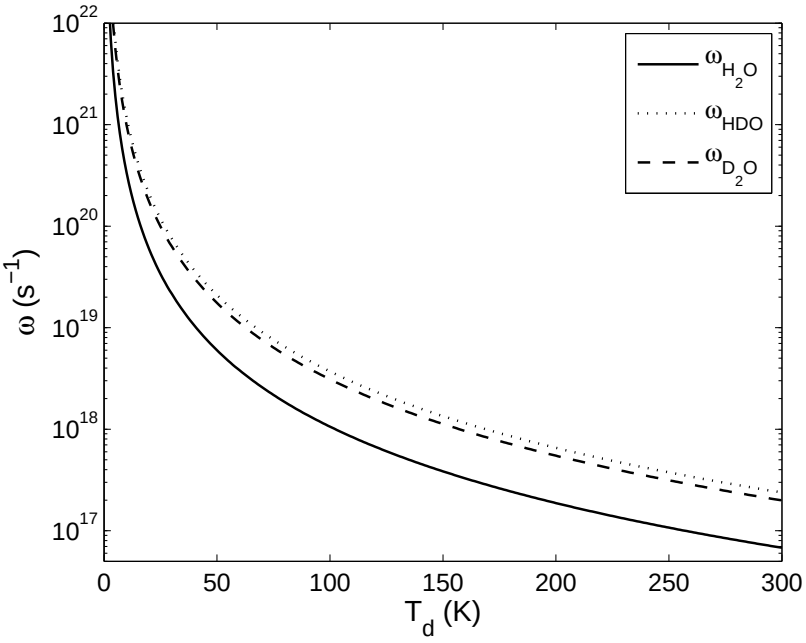

Figure 5.2: Frequency factor for loss of H_2O, HDO, or D_2O from a cluster containing initially $N = 4$ molecules, as a function of daughter temperature T_d.

Liquid drop model estimation of binding energies and temperatures

The maximum temperature of a cluster depends on the time and evaporation rate as has been shown above. The evaporation rate in turn depends on the activation energy for the process, *i.e.* the dissociation energy when no reverse activation barrier is present. To get an estimate of this energy we turn to the Gibbs-Thomson liquid drop model. In the case of water and other molecular clusters it has been used to calculate Gibbs free energy differences, enthalpy differences, and entropy differences [87–89]. Here it is used to estimate the dissociation energy of a monomer from the cluster.

The liquid drop binding energy of a neutral cluster is

$$-E_b(N) = AN - BN^{2/3} \tag{5.13}$$

where A is the bulk binding energy per molecule and B is related to the surface tension as $B = 4\pi r_1^2 \sigma_s$ where r_1 is the radius of one molecule and σ_s is the surface tension (see table 5.1). The derivative of the binding energy gives the dissociation energy

$$D_N = -\frac{dE_b}{dN} = A - \frac{2}{3}BN^{-1/3}. \tag{5.14}$$

The effect on the dissociation energy from the charge of the cluster is calcu-

lated from the polarization energy it creates and can be estimated with [76]

$$D_{pol,N} = \frac{1}{2}\frac{e^2}{4\pi\varepsilon_0}\left(1-\frac{1}{K}\right)\frac{1}{r_1}\frac{1}{3N^{4/3}} = CN^{-4/3}, \tag{5.15}$$

where K is a temperature dependent relative dielectric constant.

The total dissociation energy can thus be expressed in the bulk cohesive energy A, the surface tension term B, and the charge induced polarizable term C as

$$D_N = A - \frac{2}{3}BN^{-1/3} + CN^{-4/3}. \tag{5.16}$$

The bulk cohesive energy A is calculated using enthalpy differences ΔH and heat capacities C_p. The enthalpy differences used are given in table 5.2.

Table 5.2: Enthalpy differences at $T = 0°\text{C}$ [84]

Parameter	Description	Value
$\Delta_{\text{vap}}H$	liquid - vapor	45 054 J/mol = 0.47 eV/molecule
$\Delta_{\text{sub}}H$	solid - vapor	51 084 J/mol = 0.53 eV/molecule
$\Delta_{\text{fus}}H$	solid - liquid	6 005 J/mol = 0.06 eV/molecule

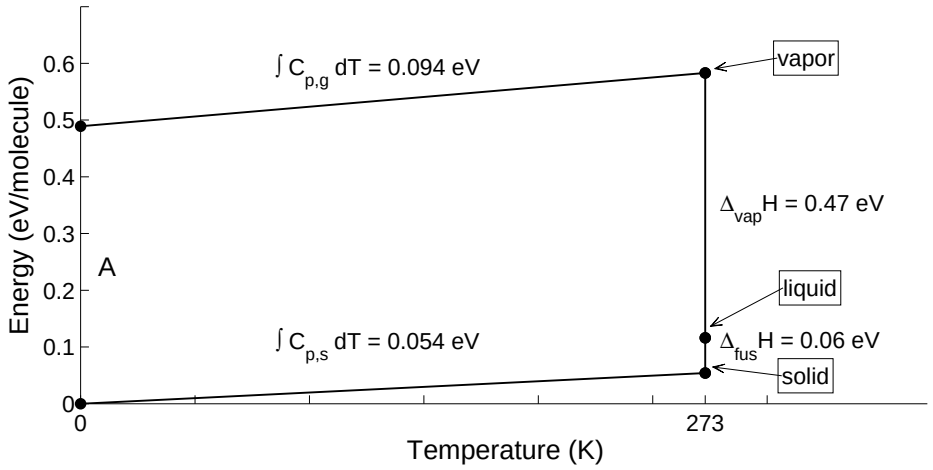

Figure 5.3: Illustration of how the enthalpy difference between ice and vapor at $T = 0\,\text{K}$ is extracted.

Figure 5.3 illustrates the process of extracting the enthalpy difference between ice and vapor at $0\,\text{K}$. The heat capacities for ice and vapor from 0 to $273\,\text{K}$ are integrated to find the value of A. The heat capacities for ice at temperatures ranging from $-250°\text{C}$ to $0°\text{C}$ are found in reference [90] and result in an approximately linear function of temperature from zero at $0\,\text{K}$ to 2.11 J/gK at

273 K. The integrated value then becomes

$$\int_0^{273\text{ K}} C_{p,s}\,\mathrm{d}T \approx \frac{2.11 \times 273}{2} = 288\text{ J/g} = 0.054\text{ eV}. \tag{5.17}$$

When integrating $C_{p,g}$ for the gas-phase a value of $C_{p,g} = 4R$ is used ($3R/2$ from translations, $3R/2$ from rotations and $1R$ from $C_{p,g} - C_v = 1$ (vibrational degrees of freedom are not active at these temperatures)), which translates to 1.847 J/gK. The integrated value becomes

$$\int_0^{273\text{ K}} C_{p,g}\,\mathrm{d}T = 1.847 \times 273 = 504\text{ J/g} = 0.094\text{ eV}, \tag{5.18}$$

and A in figure 5.3 is extracted to be equal to 0.49 eV.

The calculated values of the three parameters A, B, and C are displayed in table 5.3. The resulting dissociation energies (equation 5.16) can be seen in the

Table 5.3: Parameters included in the liquid drop model

Parameter	Value
A	0.49 eV/molecule
B	0.22 eV/molecule
C	1.25 eV/molecule

inset of figure 5.4 as a function of cluster size N. The dotted line excludes the charge effect. The maximum emission temperature of a cluster when entering the mass selection is

$$T_{e,\max} = \frac{D_N}{\ln(\omega t)}, \tag{5.19}$$

corresponding to a maximum parent temperature of $T_{p,\max} = T_{e,\max} + D_N/2C_{v,N}$ and t is the time from creation to mass selection ($t = t_1$) as described in section 3.2. The emission temperature, the emission temperature without the charging effect, the maximum sustainable parent temperature, and the resulting minimum daughter temperature are all shown in the large frame of figure 5.4. The ω used is the one calculated for H_2O in the previous section using an average $T_d = 163$ K. For heat capacity in the expression for parent temperature the microcanonical heat capacity is used, where $C_{v,N} = 6N - 6$. As we will see in the next section, this is a good approximation.

Noteworthy is that the dissociation energies and maximum temperatures extracted from the liquid drop model do not include any size-to-size variations such as shell closings or other unusual stabilities of instabilities (*i.e.* magic numbers).

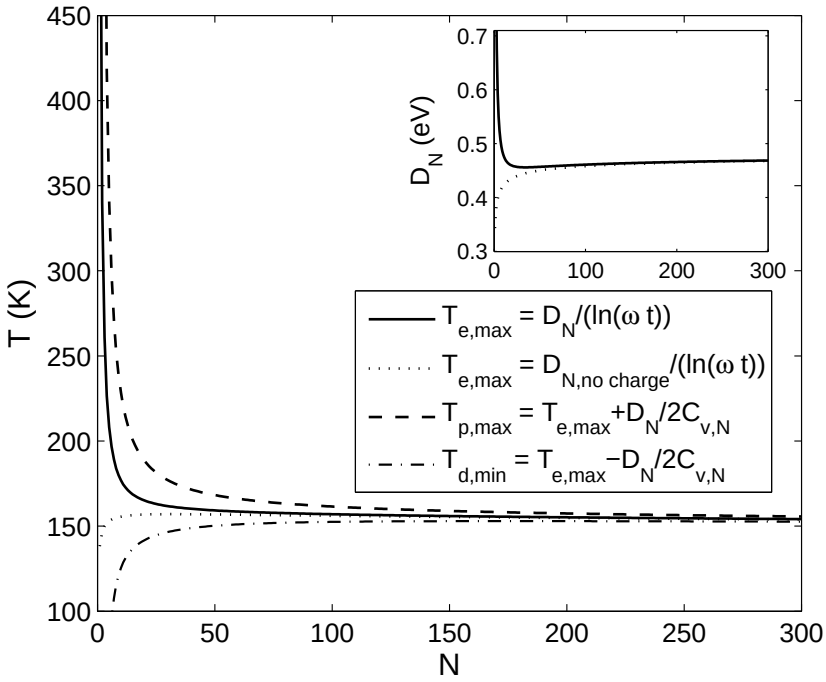

Figure 5.4: The liquid drop temperatures for emission with and without the charging parameter included in the dissociation energy (solid and dotted lines) and the parent and daughter temperature (dashed and dot-dashed lines). The inset shows the dissociation energies with and without the charging parameter included (solid and dotted lines).

For very small clusters ($N < 5$) the finite heat bath correction becomes larger than the emission temperature and the daughter temperature becomes negative. This is not physical and shows that the finite heat bath correction expansion fails for such a small system.

5.1 Heat capacities of charged water clusters

Evaporation from positive and negative clusters was studied in the cluster size range $N = 5 - 300$ and this section will show how the measured metastable decay fractions were used to deduce size dependent heat capacities for these clusters.

When attempting to produce positively charged water clusters in the corona discharge source, both pure protonated water clusters $H^+(H_2O)_N$ and mixed ammonium-water clusters $NH_4^+(H_2O)_N$ are created. Since NH_4^+ is one amu lighter than H_3O^+, they can be separated in the experiments. When switching

the polarization to study negative clusters we detect no pure water clusters at all. All clusters contain a core ion of something other than water. In some cases the specific composition of the core ion was investigated using collision induced dissociation (CID), for example in the measurements of $N = 10 - 14$ the core ion was O_2^-. Other examples of core ions produced in this source are NO_3^- [66], $N_2(NO_2)^-$, O_3^-, and CO_3^-.

5.1.1 Poisson distributed evaporation

The number of molecules lost during water molecule evaporation is quite well described by the Poisson distribution. Using the normalized intensities of the parent cluster and daughter peaks the average number of evaporated molecules λ can be calculated through

$$P_n = \frac{\lambda^n e^{-\lambda}}{n!}, \tag{5.20}$$

where n is the number of evaporated molecules and P_n is the intensity of the peak with n evaporated molecules. A Poisson distribution assumes equal probability for consecutive evaporation, which is not completely accurate in our system. The evaporation rate k depends on the cluster temperature and the clusters lower their temperature when evaporating a molecule. However, because of the low degree of evaporation in the small cluster regime (only one daughter peak) and the small change in temperature when evaporating a molecule in the large cluster regime, the Poisson distribution fits quite well for describing our process.

Paper I, figure 6 shows a comparison with the measured abundances and the ones calculated from the extracted λ, for both positive and negative clusters with $N = 20$ and 225. For $N = 225$ there is a small underestimation of the intensity in the first daughter peak, and a small overestimation of the second. Albeit small, the differences are consistent and show that it is not completely correct to assume a constant decay constant at this cluster size, but that it nevertheless fits reasonably well.

A way of approaching this problem with 'non-constant' decay constant is to use the surviving cluster fraction, *i.e.* the fraction of clusters that have not lost any molecules and calculate the average number of evaporated molecules from this. In this manner we get around the problem of decreasing temperature for the clusters in a decay chain, and this value is a principally more stable one. Setting $n = 0$ in equation 5.20 yields $P_0 = e^{-\lambda'}$, thus $\lambda' = -\ln(P_0)$. The difference between this λ' and the λ calculated using all fragmentation peaks is quite small and can be seen in figure 7, Paper I.

5.1.2 Heat capacities

As discussed in Chapter 4.2 the energy distributions for large and small cluster sizes are different. The heat capacities are extracted from the surviving fraction of clusters P using either equation 4.26 or 4.29, depending on the size regime. Both of the two limits for the positively charged clusters are shown for all N in figure 5.5, where the cross-over occurs around $N = 165$. We thus use the equation for small cluster below the crossing and the one for large cluster when $N > 165$ when extracting the size dependent heat capacities.

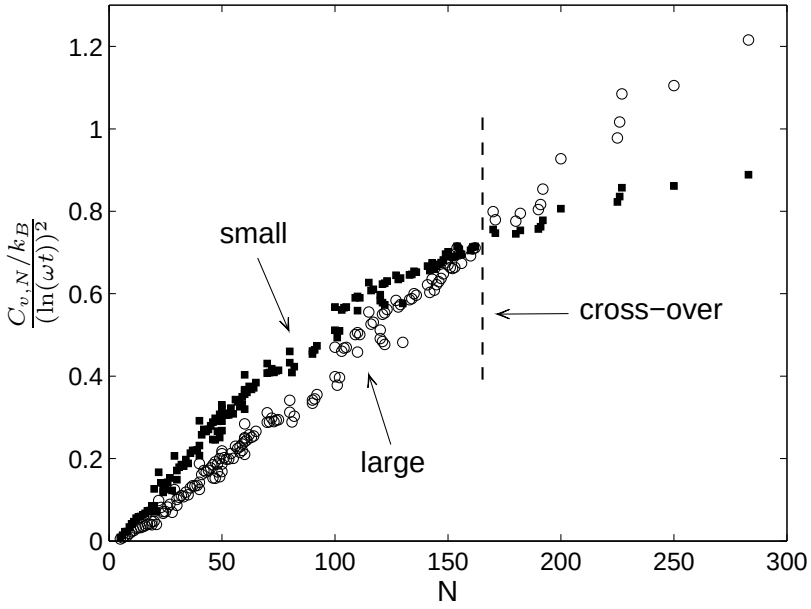

Figure 5.5: Heat capacities divided by $(\ln(\omega t))^2$ for both the large (open circles) and small (filled squares) cluster limit as a function of size N are shown. Only positively charged clusters are displayed here.

Figure 5.6 shows the size-dependent heat capacities $C_{v,N}$ for all the clusters measured. The uncertainties in the figure are from repeated measurements and the systematic uncertainties due to estimations in *e.g.* initial velocity of the clusters are estimated to be between 1% (smallest clusters) up to 9% for the largest ones. Below the cluster size $N = 165$ the small limit is plotted and above the large one. Bulk values for ice and liquid water at a few temperatures are also included as references. The small inset shows a magnified view of the small and medium size regime of the clusters, where we can see that for $N < 22$ the heat capacities coincide with those of ice, whereas for $N > 21$ they are in between ice and liquid water. The clusters investigated have heat capacities in between bulk liquid water and ice for all sizes except the smallest ones.

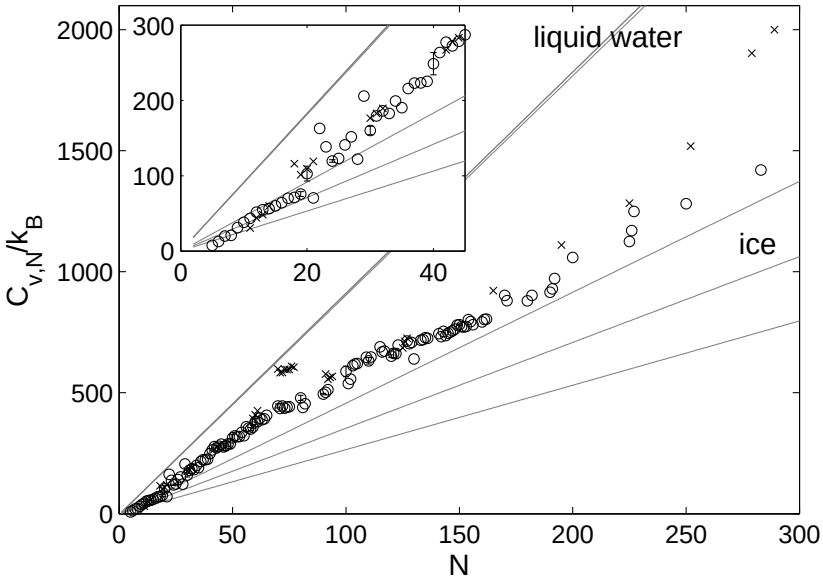

Figure 5.6: Heat capacities for positive clusters ($\circ$) and negative clusters ($\times$). Inset shows a magnified view of the large and medium size regime. References representing bulk values are included for ice at $T = 0$°C (topmost line), -63°C (middle line), and -123°C (bottom line); and liquid water at $T = 0, 50$, and 100°C, all at $P = 1$ atm.

No data in the literature have been found to compare with the results obtained here. Heat capacities have been measured for small amounts of water in nanopores [91, 92], but the influence from interaction with the substrate is hard to subtract from the results obtained. Hock *et al.* [93] have measured the caloric curves of the free water clusters $(H_2O)^-_{48}$ and $(H_2O)^-_{118}$, where a thermalization trap was used. The method can determine heat capacities below a temperature of ($\sim 120-130$ K) where spontaneous evaporation does not occur within the experimental times, but extrapolating their results to our temperatures of around $T = 160$ K show good agreement.

From figure 5.4 we see that the clusters (except for the very small ones) have a temperature of about $150 - 160$ K. The intramolecular vibrational frequencies of a water molecule are in the energy range $0.2 - 0.5$ eV ($\nu_1 = 3657$ cm^{-1}, $\nu_2 = 1595$ cm^{-1}, and $\nu_3 = 3756$ cm^{-1} [94]) which is much higher than the energy available at this temperature (160 K translates to about 14 meV). When water is in liquid or solid phase the motion of the molecules are more or less hindered by the spacial confinement and the hydrogen bonding to other molecules. Individual translational and rotational motion can still occur in this confined geometry but are converted to more or less harmonic motion around an equilibrium position. Each of these types of motion contribute approximately $3k_B$ to the heat capacity, giving a total of $6k_B$ for the contribution of the intermolecular motion to the heat capacity. The slope of the heat ca-

pacity measurements in figure 5.6 gives an increase of roughly $6k_B - 8k_B$ per added molecule which thus fits well with what is expected for water at these temperatures.

After the discussion about temperature it is quite noteworthy that in figure 5.6 the clusters of sizes larger than $N = 21$ have heat capacities between liquid and frozen. Bulk water at temperatures around 160 K is completely frozen. However, for very small particles there is often a decrease in the melting point temperature. As is shown in [93], the latent heat peak in the caloric curve for the two clusters measured did not exist as it does in bulk water. Instead a gradual transition occurs, which comes at a lower temperature the smaller the clusters are. This can explain why the middle-sized clusters appears to have a heat capacity in-between those for frozen and liquid water.

5.2 Mixed ammonia and water clusters

Relative evaporation fractions from small mixed ammonia and water clusters, $H^+(H_2O)_n(NH_4)_m$, were measured in the same manner as the positively and negatively charged water clusters, where the fraction of water alt. ammonia loss is measured by a mass difference of the daughter cluster of 1 amu. Some of the air surrounding the needle where the corona discharge takes place was enriched with ammonia by bubbling it through an ammonia-water solution before it entered the cluster forming region. With this setup the majority of clusters contains four ammonia molecules, as can be seen in figure 5.7. Three different scans are shown, with three different flow rates of air through the water ammonia solution. In (a) only a small portion ($5 - 10$ %) of the air went through the solution before entering the chamber, in (b) the fraction was about 50 % and in (c) all the air went through the solution. Relative and overall intensities of the various cluster configurations in the mass spectra are quite sensitive to the ammonia concentration in the solution. With the proportion of ammonia content in the solution decreasing over time, the mass spectra shift to heavier clusters containing a larger proportion of water molecules.

The total number of molecules in a cluster is called the rank $N = n + m$ and spontaneous evaporation was measured for rank $N = 3 - 11$ and 16 with all the combinations of n and m that could be produced. The number of water and ammonia molecules in a cluster is uniquely determined by the mass up to 307 amu, equivalent to a protonated cluster containing 17 water molecules or 18 ammonia molecules, *i.e.* up to rank 17. In this size regime the clusters only evaporate one molecule, apart from the identified CID peaks.

A summary of the results from the spontaneous evaporation measurements can be seen in figure 5.8, where the darker circles represent a cluster contain-

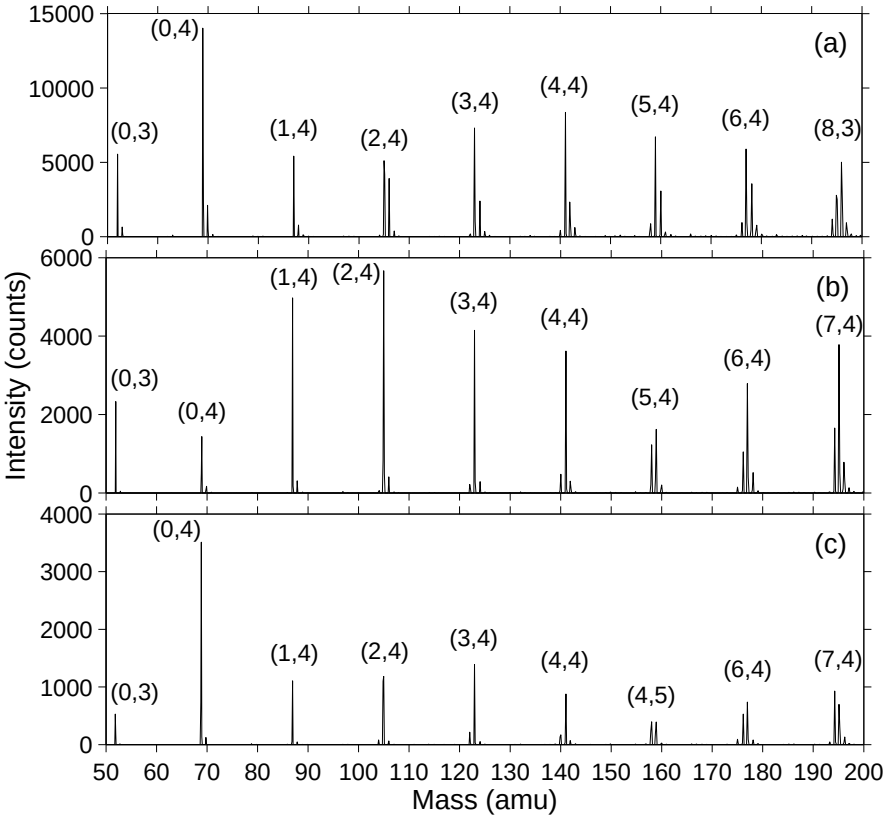

Figure 5.7: Mass spectra for three different ammonia flow rates, increasing from (a) to (c). The masses $50 - 200$ amu correspond to a total number of molecules in the clusters, N, between 3 and 11. The numbers in parentheses represent the number of water and ammonia molecules ((n, m), as explained in the text) in the cluster with the highest intensity.

ing (n, m) water and ammonia molecules respectively, with the addition of one proton. The lighter color circles represent clusters not measured. The bars going down to the right (blue) and left (red) represent the relative water and ammonia loss, adding up to 100 for each cluster. The number in italics underneath each cluster circle with $N \geq 5$ is the total evaporation probability in parts per thousand. This information is not available for the smaller clusters because it is not possible to separate CID from true evaporation.

5.2.1 Discussion on stability and structure

The proton affinity of ammonia is larger than the one for water and should therefore bind stronger to the protonated ammonium ion. Up to rank 4 this fits

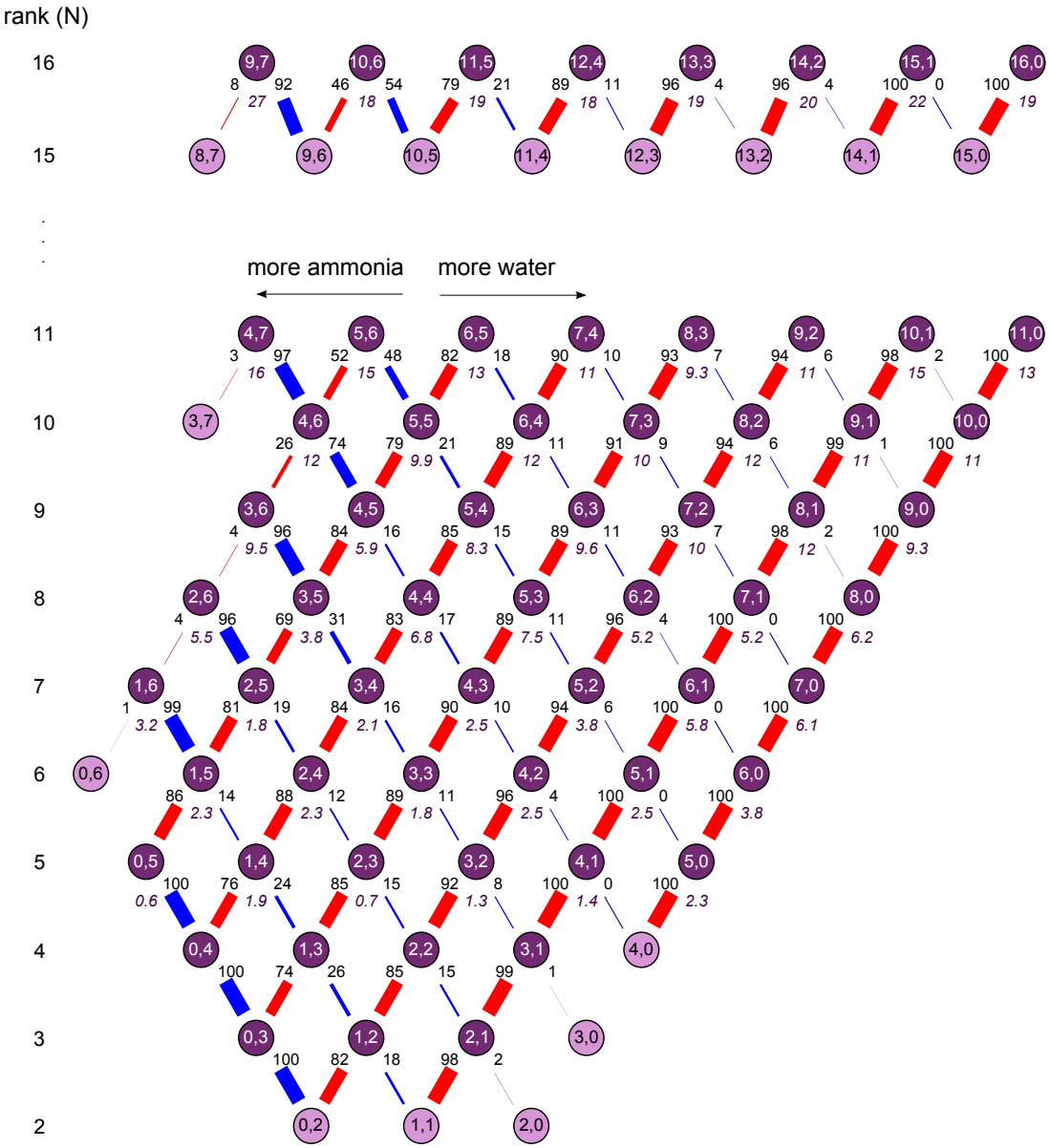

Figure 5.8: Map of the clusters for which metastable decay has been measured (represented by darker colored circles). The products for which metastable decay was not measured are shown in lighter color. The number of water and ammonia molecules are represented by the numbers (n, m) in the circles. The bars from each of the measured cluster give the relative spontaneous evaporation fraction of water (pointing left) and ammonia (pointing right). The numbers in italic just below the circles represent the total evaporation in parts per thousand (‰). The ranks N are given to the left of the diagram.

with what is observed in the mass spectra; see figure 5.7 where even in spectrum (a) where a relatively small proportion of ammonia is in the vicinity of the needle during production, there are mostly pure ammonia clusters. Water is however in general a more efficient hydrogen bonding molecule with its two acceptor and two donor sites whereas ammonia has three donor and only one acceptor site. In an unlimited network of hydrogen bonding molecules, this numerical symmetry and the dipolar character of the water molecule makes it the most efficient binding molecule. This is consistent with what is detected in the mass spectra for clusters larger than rank 4 where the majority of the clusters contain additional water molecules to the four ammonia molecules. In addition, the ion induced force binding molecules to the ammonium ion decreases rapidly with distance and becomes partially shielded with the first shell around it occupied [35]. Calculations on free energies on these clusters from [45] show that the two first sites around the ammonium ion is filled by ammonia but that the two last sites are preferably occupied by water. The strength with which the other ammonia molecules bind to the outer shell is found to be the same as for water molecules.

From figure 5.8 it is clear that in most cases the preferred evaporation channel is water loss. Only for clusters with 6 or more ammonia molecules is ammonia evaporation the preferred channel, except at rank 11 and 16 where the clusters with $m = 6$ have a close to $50/50$ chance of losing either molecule. It might now be tempting to conclude that the cluster geometries consist of a central ammonium ion surrounded by four ammonia molecules in an inner shell, and with the water molecules in the next shell which if an additional ammonia molecule were present would be much more loosely bound. However, studying what types of clusters are produced in most abundance do not support this picture (see figure 5.7). Up till $N = 4$ the clusters consist of mainly ammonia but for $N \geq 5$ the most intense peaks show up for clusters with water added, even in the spectrum with an abundance of ammonia present at the creation site.

From the measurements of dominant evaporation channel alone, deducing a single structure for each cluster kind is not possible. It might not be meaningful either since as reported before, mixed ammonia and water clusters have several energetically low-lying isomers and the population studied here likely consists of a mixture of these. Comparing these results with computations deducing structure such as those in [45] is thus difficult. We can only conclude that even if there are water molecules in the first shell surrounding the ammonium ion and ammonia molecules in the second shell, water still evaporates to a higher degree than ammonia if the number of ammonia molecules does not exceed six.

5.3 Relative evaporation rates for light, heavy, and mixed water molecules

Spontaneous evaporation branching ratios for light, heavy, and mixed water molecules were measured for the clusters $NH_4^+(H_2O)_3 - d_n, n = 0 - 6$, *i.e.* one ammonium ion with three water molecules attached, containing in total zero to six deuterium replacing hydrogens.

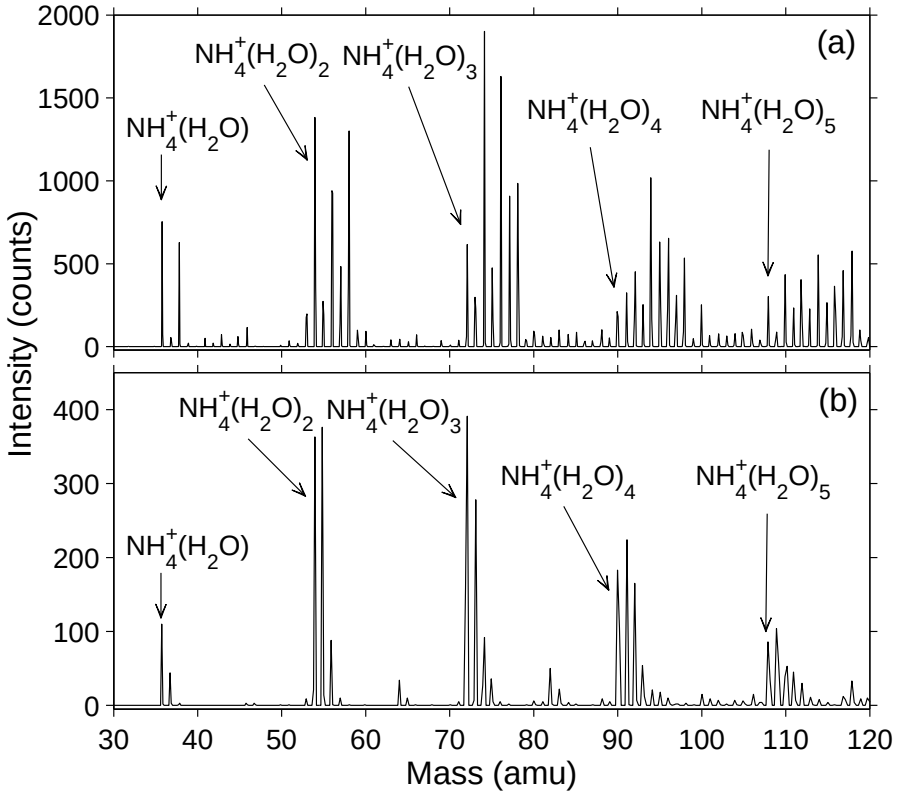

Figure 5.9: Mass spectra from the two production methods described in the text, where (a) is from heavy water collisions in the octopole and (b) from when heavy water vapor was present at the corona discharge. The marked peaks are the ones containing no deuterium. The peaks following them have one, two, etc. H exchanged with D.

The clusters are generated in the same way as the pure protonated water clusters. To facilitate the exchange of hydrogens to deuterium the octopole was flooded with heavy water steam to ca. $3 \cdot 10^{-2}$ mbar where low energy collisions take place and deuterium becomes incorporated into the clusters. An example of a mass spectrum is shown in figure 5.9(a). Another method was

also attempted where heavy water was incorporated already at the production site, using the electrospray source. A mass spectrum using this method is shown in figure 5.9(b). Unfortunately the cluster beam was too instable and too low in intensity to perform evaporation measurements on clusters containing three or more deuterium atoms.

The composition of the clusters seen in the mass spectrum in figure 5.9(a) shows a strong odd even effect in the number of deuterium incorporated. The intensity of the even number deuterium peaks is relatively much stronger. This could be due to at least three effects. Either heavy water simply aggregates onto the clusters, with or without proton scrambling, and loss is negligible. There could also be scrambling involved and a strong bias towards mixed water molecules (HDO) evaporation. The final alternative is that heavy water molecules are incorporated, low or no proton scrambling takes place, and both heavy and light water molecules evaporate intact. By examining only the mass spectrum none of the above explanations can be excluded.

Comparing the mass spectrum in (a) with the other production method in (b) when heavy water was present already in the production phase displays a difference in composition. The deuterium distribution in (b) is more of a smooth function where the odd even effect seen in (a) is not present. This give an indication that the second explanation is less likely; if there was a strong bias towards HDO evaporation in the first case, it seems likely that it would be so regardless of production method. The absence of an odd-even effect in the abundance distribution in (b) can be due to the longer time spent in the formation region as compared to the octopole, or to high energy processes associated with the cluster formation, in particular the formation of the core ion.

Also notable is the low intensity of clusters in (a) containing more deuterium than twice the number of water molecules present in the cluster. This is an indication that the hydrogens in the ammonium ion remain unswitched.

5.3.1 Branching ratios and evaporation rates

The metastable evaporation in the free flight section of the separator was measured in the same manner as for the mixed ammonia and water clusters. The relative evaporation fractions for the mixed clusters created by collisions in the octopole are shown in figure 5.10 as a function of deuterium content. In the following we shall restrict ourselves to clusters produced in this manner.

The clusters are seen to evaporate exclusively single water molecules, except for the clusters containing five deuterium ($NH_4^+(H_2O)_3 - d_5$) where a fragment of mass 17 amu was detected as 12% of the total evaporation. It is labeled NH_3

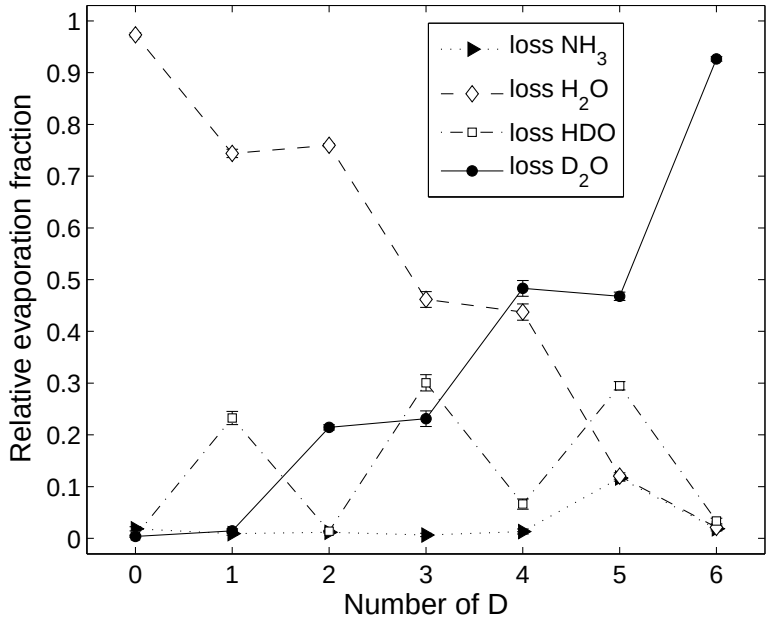

Figure 5.10: Relative evaporation fractions for NH_3, H_2O, HDO, and D_2O from $NH_4^+(H_2O)_3$ as a function of deuterium content in the cluster. The data displayed here is collected from measurements on metastable evaporation from cluster created through heavy water collisions in the octopole, *i.e.* the situation shown in figure 5.9(a).

loss in figure 5.10 but can possibly be due to impurities at this cluster mass in the beam.

For clusters containing even number deuterium there is hardly any HDO evaporating. This indicates that very little scrambling takes place, or that the evaporation is selective for the isotopically pure species. The latter explanation runs counter to the second hypothesis for explaining the low abundances of odd mass peaks in the mass spectrum in figure 5.9(a), that there is a strong bias for HDO evaporation.

To sort out the different possible situations we start by making some assumptions and compare the consequences from these with the measured evaporation fractions. Under the assumption of equal decay rate constants for the three water isotopologues there are three levels of scrambling to consider:

- ◇ No scrambling. The appearance of HDO in some clusters is due to direct attachment of HDO to the cluster from contamination of the heavy water in the octopole or of the light water in the corona discharge. The probability for HDO loss is zero for even number deuterium, $1/3$ for odd.

- ▷ Full scrambling between the hydrogens associated with the water molecules in the cluster. Total number of hydrogens possibly involved in the scrambling is six.
- ▼ Full scrambling between all hydrogens in the cluster, also the ones pertaining to the ammonium. Total number of hydrogens possibly involved in the scrambling is ten.

For the last two situations the isotope distribution of the emitted fragment can be calculated as

$$I(D,d) = \frac{\frac{D!}{(D-d)!}\frac{P!}{(P-p)!}\frac{(p+d)!}{p!d!}}{\frac{(D+P)!}{(D+P-d-p)!}} = \frac{\frac{D!}{(D-d)!}\frac{P!}{(P-p)!}\frac{2}{p!d!}}{\frac{(D+P)!}{(D+P-2)!}} \tag{5.21}$$

where $I(D,d)$ is the probability that the evaporating molecule contains p hydrogens and d deuterium, and $p+d=2$. D is the total number of deuterium in the parent cluster and P is the corresponding number of hydrogens. In the second situation (▷) $P+D=6$ and in the third (▼) $P+D=10$.

Figure 5.11 shows the evaporation fractions as calculated using the three models (◇, ▷, and ▼), together with the experimental data (•). The three different possible evaporation products are shown in different frames. The possible ammonia evaporation for $D=5$ is disregarded. The scheme that fits the experimental data the best is the no scrambling hypothesis. It correctly mimics the step-like behavior of the light and heavy water evaporation, but it does not give the correct relative amount of evaporation at the plateaus. It also correctly follows the odd-even shape of the HDO evaporation.

A modification of the first and second model (◇ and ▷) above can be attempted by letting go of the assumption of identical evaporation rate constants for the three species. Instead we assume that they are proportional to the content of the molecular species of the cluster but otherwise independent of the composition of the cluster. We also allow some scrambling among the hydrogens belonging to the water molecules but do not assume full scrambling. The branching ratios $I(D,d)$ from a cluster containing D deuterium with a fragment containing d deuterium can then be written as

$$I(D,d) = k_d f(D,d) \tag{5.22}$$

where k_d is the evaporation rate constant and $f(D,d)$ is the normalized abundance of water molecules containing d deuterium,

$$f(D,0) + f(D,1) + f(D,2) = 1. \tag{5.23}$$

We also make the assumption that the amount of scrambling is symmetric, *i.e.* $f(D,d) = f(6-D, 2-d)$. The symmetry is trivially fulfilled for the pairs

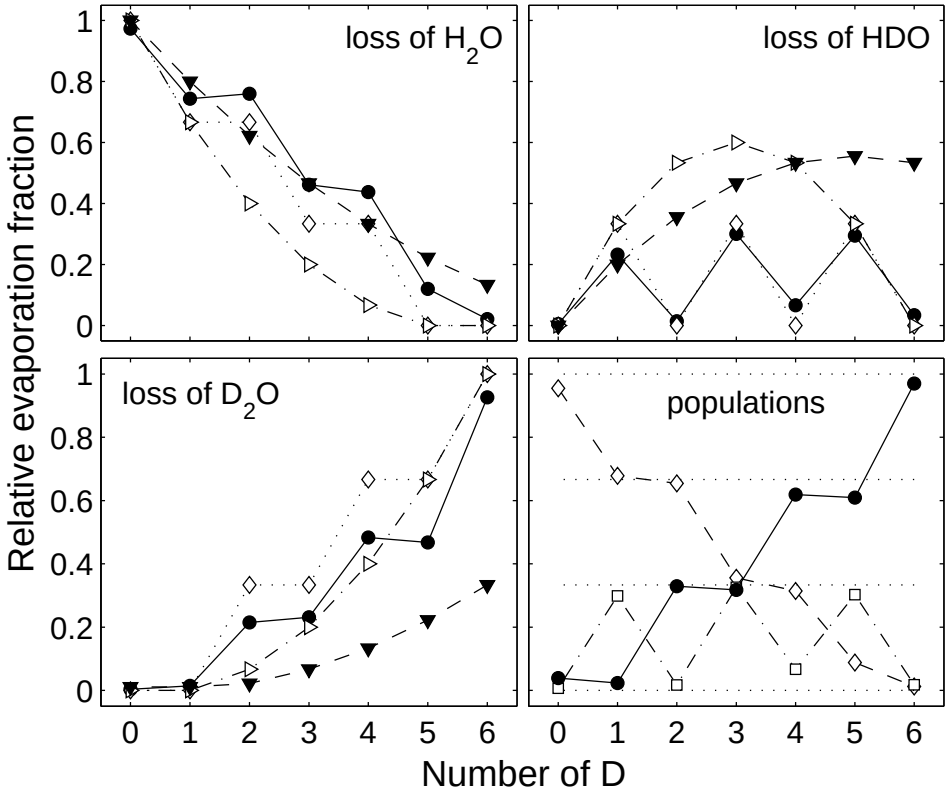

Figure 5.11: The first three frames displays the three models for evaporation assuming equal decay rate constants together with the experimental data (•). In short; ◇ - no scrambling, ▷ - scrambling among water hydrogens, and ▼ - scrambling among all hydrogens. The bottom right frame shows the relative populations $f(D, d)$ as calculated by equation 5.34. The symbols representing the different water isotopologues are the same as in figure 5.10.

$D = 0$ and $D = 6$, and $D = 1$ and $D = 5$, but has consequences for $D = 2$ and $D = 4$. For some compositions the populations can be expressed explicitly or be constraint by another population as $f(0, 0) = 1$, $f(0, 1) = 1$, $f(1, 1) = f(5, 1) = 1/3$, $f(3, 0) = f(3, 2)$ etc. Also some trivial branching ratios can be written down as

$$I(0,1) = I(0,2) = I(6,0) = I(6,1) = I(1,2) = I(5,0) = 0 \quad (5.24)$$

$$I(0,0) = I(6,2) = 1 \quad (5.25)$$

where a comparison with experimentally observed ratios give five values between 0.004 and 0.02 and a single value, for $I(5, 0)$, of 0.12 for equation 5.24. The two ratios for equation 5.25 were observed to be 0.96 (for $D = 0$) and 0.93 (for $D = 6$), which may suggest a minor contamination and/or a small amount of scrambling with the hydrogen atoms in the ammonia core.

Some relations between the decay rate constants can be posed as:

$$q_1 \equiv \frac{I(5,2)}{I(1,0)} = \frac{k_2}{k_0} \tag{5.26}$$

$$q_2 \equiv \frac{I(4,2)}{I(2,0)} = \frac{k_2}{k_0} \tag{5.27}$$

$$q_3 \equiv \frac{I(3,2)}{I(3,0)} = \frac{k_2}{k_0} \tag{5.28}$$

$$q_4 \equiv \frac{I(2,2)}{I(4,0)} = \frac{k_2}{k_0} \tag{5.29}$$

$$q_5 \equiv \frac{I(5,1)}{I(1,0)} = \frac{1}{2}\frac{k_1}{k_0} \tag{5.30}$$

$$q_6 \equiv \frac{I(1,1)}{I(1,0)} = \frac{1}{2}\frac{k_1}{k_0} \tag{5.31}$$

The measured relations for $q_n, n = 1-4$ give values for k_2/k_0 between 0.49 to 0.64 with an average value of 0.56 ± 0.08. The last two ratios give $k_1/k_0 = 0.71 \pm 0.12$, where the uncertainties are one standard deviation. Thus, the relative evaporation rate constants are then approximately $k_0 : k_1 : k_2 = 1 : 0.71 : 0.56$. The relative abundances of the three different water species for the different cluster compositions in the measurements are found by rewriting equation 5.22 as

$$f(D,d) = \frac{I(D,d)}{k_d}, \tag{5.32}$$

and normalizing by the common factor $c(D)$, which is

$$c(D) = \sum_{d=0,1,2} \frac{I(D,d)}{k_d}. \tag{5.33}$$

The relative populations of the three species are then

$$f(D,d) = \frac{1}{c(D)}\frac{I(D,d)}{k_d}. \tag{5.34}$$

The bottom right frame of figure 5.11 shows the populations as calculated from the experimental values using equation 5.34. The symbols representing the different water isotopes in this frame are the same that were used in figure 5.10. The vertical dotted lines are positioned at $0, 1/3, 2/3$, and 1. The populations calculated from the experimentally measured evaporation fractions falls very close to the expected populations when no scrambling takes place, when the evaporation rates for the different isotopes are allowed to be different.

As was discussed in Chapter 2.1.1 some different types of studies have been performed regarding the evaporation and nucleation of light and heavy water,

on both the macro- and microscale. Measurements of evaporation from ices at temperatures similar to these clusters ($170 - 190$ K) showed a 50% lower evaporation rate for D_2O [34], consistent with the results here. On the other hand Graul *et al.* [32] measured a slight preference for D_2O emission in collision experiments on mixed protonated cluster. We expect that the more gentle method of spontaneous evaporation gives a more faithful representation of the low energy thermodynamic properties of the clusters as compared to the higher energy processes involved in collisions, but also note that our results are not directly comparable because of the difference in core ion between their experiments and ours.

The frequency factors for the three isotopologues of water calculated in the beginning of this chapter would, everything else being equal, give a ratio of evaporation rate constants of $k_0 : k_1 : k_2 = 1 : 3.5 : 2.9$ which goes in stark contrast to our measurements of $k_0 : k_1 : k_2 = 1 : 0.71 : 0.56$. The observations must thus be ascribed to the thermal properties of the resulting daughter cluster after evaporation (since the parent clusters are in all cases identical). The nucleation rate study from [33] gives much higher nucleation rates for heavy water compared with light water under identical pressures and temperatures. Given that nucleation involves a large number of evaporation and absorption events for each net molecule gained, this is consistent with our observation of increased evaporation rate for H_2O. However, one should not make too much out of comparisons between pure species of either isotopologue. Measurements of metastable fragmentation yielding similar fractions from different pure species is rather an indication of similar heat capacities than of decay rate constants, as discussed in section 5.1.2.

CHAPTER 6

Thermionic emission and radiative cooling

Useful tool for the study of thermionic emission and radiative cooling are the electrostatic storage devices. Some examples of similar experiments but with different results and conclusions will be presented here. The work is performed utilizing the TMUe-ring, described in Chapter 3.

6.1 Absolute cooling rates for C_{60}^-

Absolute cooling rates for radiation and thermionic emission were determined for fullerenes. In short, the systematics is the following. A bunch of hot C_{60}^- is injected into the storage ring. The bunch cools down with time, both through radiative cooling of the individual ions and by depletion of the bunch from the high energy side of the distribution. After a certain predetermined time a laser pulse is fired at the bunch, thus heating up the fraction of the molecules that absorb a photon. Effectively, this can be seen as bringing them back in time, to a state (or time) when they were hotter. If this time can be determined, the cooling between this back-shifted time and the laser firing time equals the energy of the absorbed photon (assuming a maximum of one photon absorbed per ion).

The laser firing time is an experimentally set time, whereas the determination of the back-shifted time requires an analysis of the data. A way of finding this time is by comparing the logarithmic slope of the signal from the enhanced neutral yield after laser irradiation to the slope of the spontaneous electron emission. When they are the same, the energy distributions are also the same. The time difference between these two times is referred to as Δt and the average cooling rate between the back-shifted time and the laser firing time is thus $\dot{E} = h\nu/\Delta t$ where the absorbed photon has an energy $h\nu$. A schematic illustration of the idea can be seen in figure 6.1, but a more thorough description will follow.

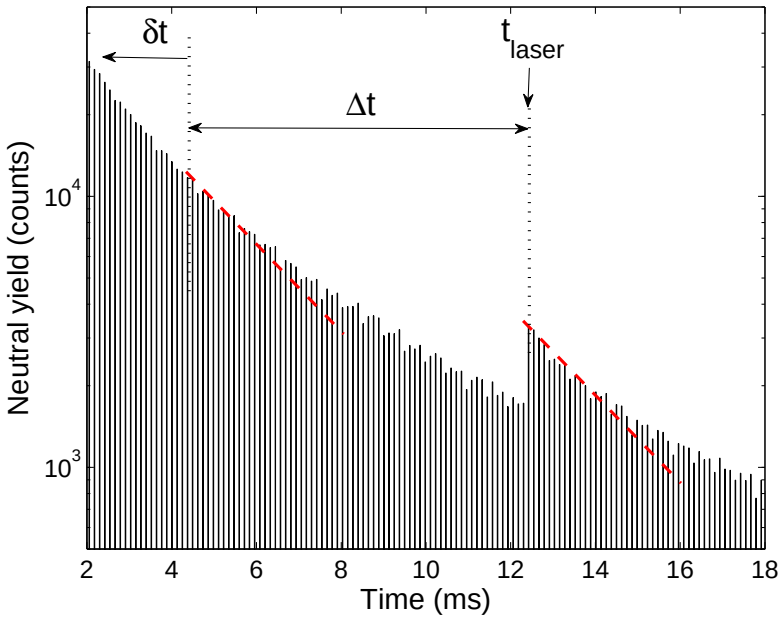

Figure 6.1: An illustration of the idea behind the extraction of cooling rates for C_{60}^-. Δt is the time it takes for the C_{60} to cool down one photon energy. δt is equal to the laser firing time subtracted with this time difference, *i.e.* $\delta t = t_{\text{laser}} - \Delta t$.

6.1.1 Experimental procedure and data analysis

As described in Chapter 3, C_{60}-molecules were laser desorbed from a surface and in the process became ionized. The molecules were accelerated to 15 keV and let into the storage ring. At this velocity one revolution takes 122 μs and three kick-pulses were applied to clean up the beam. Thus, the first 33 revolutions (~ 4 ms) may contain impurities and were left out of the analysis. The counts are summed up for each revolution in the ring.

The neutral yield from spontaneous electron emission for 58 spectra recorded without laser induced decay can be seen in figure 6.2(a). They are referred to as reference spectra, $I(t)$. The average of the spectra is shown as the black dashed line. Except for overall variations in intensities, the spectra are all quite similar. The average neutral yield is fitted to equation 4.41 using the method described section 4.2.3, yielding $a_1 = -122\,\text{s}^{-1}$ and $a_2 = 1324\,\text{s}^{-2}$ for the values in the exponential term.

When studying the enhanced yield from photon absorbtion ($I_e(t)$), laser energies of $h\nu = 1.9{-}2.7$ eV were used and the laser was fired after $t_{\text{laser}} = 5{-}35$ ms of storage time. The power of the laser was kept low enough to only allow one photon absorption. For every photon energy and storage time four spectra were collected and one reference spectrum without laser firing. Each spec-

trum contained between $4500 - 9000$ ion injections. The reference spectrum was used for subtracting spontaneous electron emission from the laser enhanced signal. Figure 6.2(b) shows both a reference spectrum (dashed line) and a laser enhanced spectrum (circles). The photon energy used in this example was $h\nu = 2.7$ eV and the laser was fired after $t_{\text{laser}} = 12.5$ ms of storage time. A proportionality constant d is used for normalization when subtracting the reference spectrum $I(t)$ from the laser enhanced one $I_e(t)$. Since the overall intensity of the injected clusters can vary from scan to scan, the d's are a measure of the statistics and used as weights for averaging the δt's extracted from the different scans, where $\delta t = t_{\text{laser}} - \Delta t$ as shown in figure 6.1.

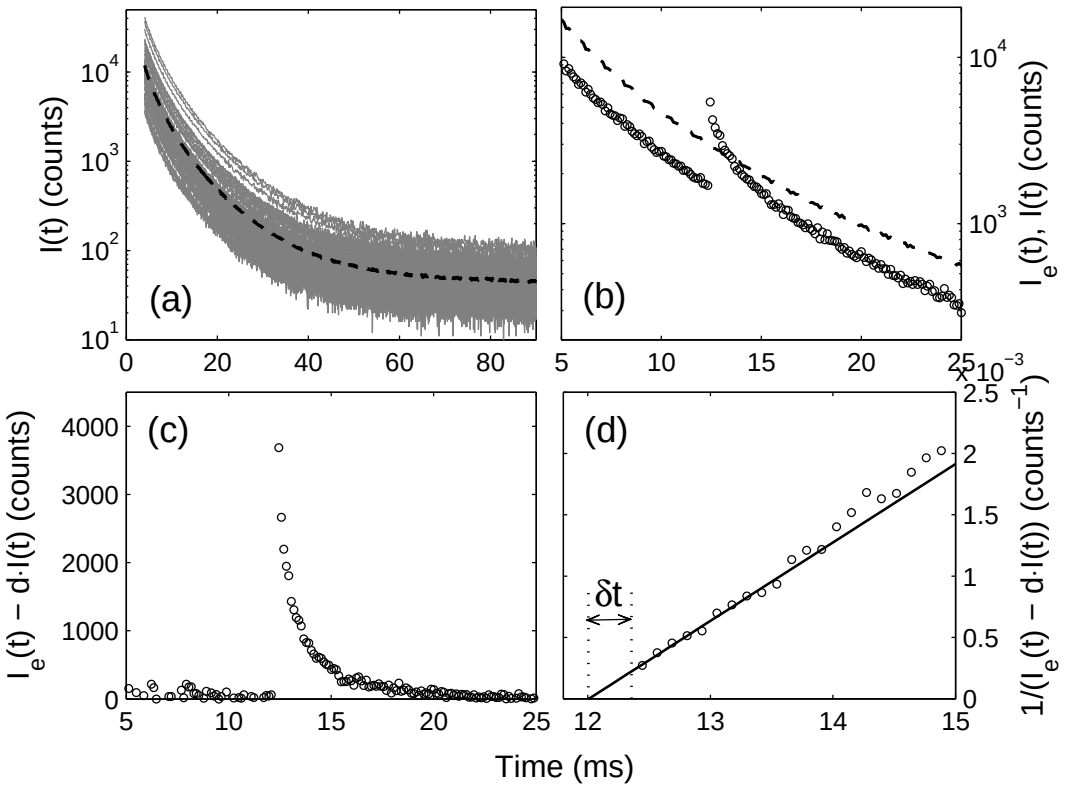

Figure 6.2: All 58 measured spectra without photon excitation, plotted in grey, together with the average of all spectra shown as the dashed line in (a). In (b) an enhanced spectrum with $t_{\text{laser}} = 12.5$ ms and $h\nu = 2.7$ eV is shown as circles together with a reference spectrum. Frame (c) shows the same spectrum when the reference spectrum has been subtracted, and (d) shows the extraction of the time δt by locating the intersection of the inverted enhanced spectrum with $y = 0$. Note the different timescales on the x-axes.

The enhanced spectrum after subtraction of the reference spectra ($I_e(t) - dI(t)$) is displayed in figure 6.2(c). For short times thermionic emission is the dominant process which makes the subtracted enhanced signal roughly propor-

tional to a $1/(t+\delta t)$-decay, as seen when the inverse is plotted in (d). The back-shifted time δt is to a first approximation extracted from $(t_{\text{laser}} - \Delta t)$, where Δt is the time where the fitted line in (d) intercepts $y = 0$. The relation used is

$$I_e(t) - dI(t) \propto \frac{p}{t - \Delta t} \quad \Rightarrow \quad \frac{1}{I_e(t) - dI(t)} \propto \frac{t - \Delta t}{p}, \tag{6.1}$$

where p is the fraction of clusters that have absorbed a photon. For the fit the counts in the ten first revolutions after the laser was fired are used with weights proportional to the counts in the peaks.

The first approximation of δt with $t_{\text{laser}} - \Delta t$ in equation 6.1 can be made more accurate by a few considerations. Firstly, the half revolution the molecules have gone between laser excitation and detection is subtracted. The next consideration is regarding the spontaneous electron emission from molecules not absorbing a photon. The measured intensity of the laser enhanced signal is

$$I_e(t) = p\, I(t - \Delta t) + (1 - p) I(t) \;\; \Rightarrow \;\; I_e(t) - I(t) = p\,(I(t - \Delta t) - I(t)), \tag{6.2}$$

where the last term on the right hand side in equation 6.2 was not included in equation 6.1. To include this term the fit to the neutral yield without photon absorption was used and we get a correction to the extracted δt's of on average 1.4%.

The small effect from radiative cooling at short times need also be considered. The curvature found in the fit to the reference spectra are used to correct for this effect as

$$\delta t' = \frac{\delta t}{1 + a_1 \delta t + 2 a_2 \delta t^2}, \tag{6.3}$$

where $\delta t'$ are the corrected values for the back-shifted times. This correction is a little bit larger, 7.4% on average.

6.1.2 Results and discussion

The δt's are the time the clusters are shifted back to after photon absorption, as has been explained above. Figure 6.3 shows the measured δt's for four photon energies $h\nu = 2.0, 2.3, 2.5$, and 2.7 eV. As expected, with the relatively low photon energy 2.0 eV, the clusters do not get as hot as with the higher photon energy and they are not brought back in time as far as with *e.g.* a 2.7 eV photon. Also as expected, when the clusters have circulated for a relatively long time in the ring, one photon absorption does not bring them back in time as far as when they have spent a shorter time in the ring.

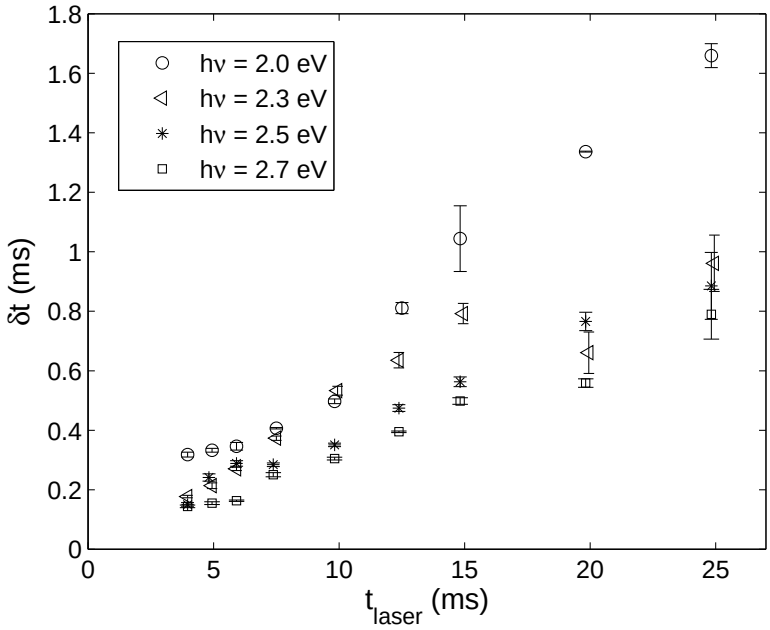

Figure 6.3: A selection of the measured δt plotted vs. t_{laser} for four different photon energies; $h\nu = 2.0, 2.3, 2.5$, and 2.7 eV.

Since the times δt and t_{laser} are so different in magnitude, the cooling rates directly extracted from this procedure will cover large time-spans, hence they will be averages over long times. To get a better coverage and shorter average intervals the data can be used in a better way. By subtracting rates for the same laser firing times but with different photon energies we get cooling rates for the time interval $[t_{\text{laser}} - \Delta t_1, t_{\text{laser}} - \Delta t_2]$ with the photon energy difference $h\nu_1 - h\nu_2$. This method will cover the cooling rates at short times. To get cooling rates for the longer times we identify the measurements that give the same δt (or $t_{\text{laser}} - \Delta t$), but with different photon energies and t_{laser}. The cooling rates will thus span the time intervals $[t_{\text{laser},1}, t_{\text{laser},2}]$.

The result from this analysis can be seen in figure 6.4, where the open black circles are the total cooling rates.

To disentangle the radiative cooling part from the thermionic emission the fit in equation 6.2 is used once more. An effective time $t'(t)$ where the rate would have had the observed value in the absence of radiative cooling is found by equating the expression in equation 6.2 with the fitted function for the mea-

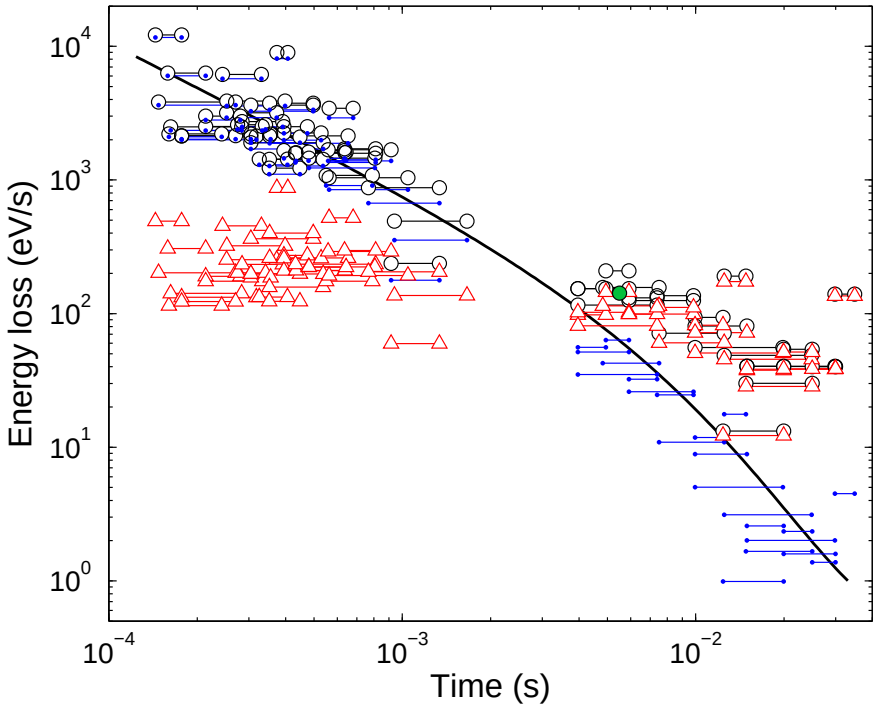

Figure 6.4: Cooling rates for C_{60}^-. The open black circles are the total cooling rate, the red dots represents the contribution from radiative cooling and the blue dots shows the contribution from thermionic emission. The line is equation 4.41 (the same as $I_{\mathrm{non-rad}}$ in figure 6.5, but with the constant a_0 fitted to the short times). The green circle is a modeled value of radiative cooling from the spontaneous decay curve in [77].

sured decay in equation 4.41 as

$$\begin{aligned} I_{\mathrm{non-rad}}(t') = I_{\mathrm{rad}}(t) \quad &\Rightarrow \quad \frac{1}{t'\ln(\omega t')^2} = \frac{e^{a_1 t + a_2 t^2}}{t\ln(\omega t)^2} \\ &\Rightarrow \quad t' = te^{-a_1 t - a_2 t^2}\frac{\ln(\omega t)^2}{\ln(\omega t')^2} \\ &\Rightarrow \quad t' \approx te^{-a_1 t - a_2 t^2}. \end{aligned} \tag{6.4}$$

t' is thus greater than t. An illustration of this effect is given in figure 6.5. On the right side the inverse of the intensities are plotted, and the deviation form a straight line is clearly seen.

The relation between t and t' is now used to disentangle the radiative cooling from the thermionic emission cooling. The method used assumes that radiative cooling can be described as a continuous process, which requires that the average energy of the emitted photons is not too large.

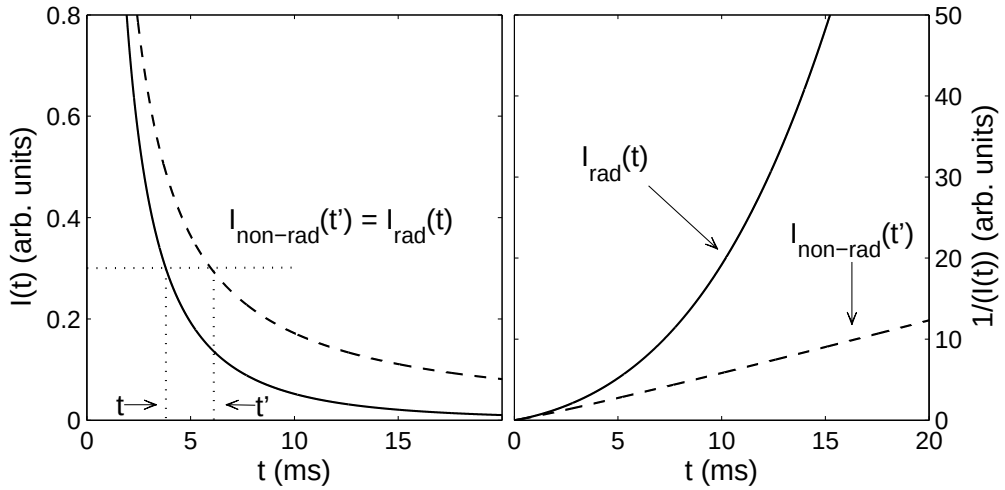

Figure 6.5: $I_{\mathrm{non-rad}}(t')$ (dashed line) and $I_{\mathrm{rad}}(t)$ (solid line) are plotted on the left side in the time interval $0-20$ ms, and the inverse of the neutral counts are plotted on the right side.

The total rate of decrease of the maximum energy in the ensemble is

$$\left.\frac{dE_m}{dt}\right|_{\mathrm{tot}} = \frac{\Phi C_v/k_B}{t'\ln(\omega t')^2}\frac{dt'}{dt} \tag{6.5}$$

and the radiative cooling part of this energy decrease is

$$\left.\frac{dE_m}{dt}\right|_{\mathrm{rad}} = \frac{\Phi C_v/k_B}{t'\ln(\omega t')^2}\left(\frac{dt'}{dt}-1\right). \tag{6.6}$$

Integrating equation 6.6 between two times $[t_1;t_2]$, where the time interval can be either the short or long intervals as described above, gives the radiative energy loss in this time interval. Thus

$$-E_{\mathrm{rad}}(t_1;t_2) = \int_{t_1}^{t_2}\left.\frac{dE_m}{dt}\right|_{\mathrm{tot}}dt = h\nu - \int_{t_1}^{t_2}\frac{\Phi C_v/k_B}{t'\ln(\omega t')^2}dt, \tag{6.7}$$

where $h\nu$ is either the energy of the absorbed photon or the difference between two photon energies if the short time intervals are calculated. But the energy $h\nu$ can also be expressed as the difference in maximum energy of the ensembles between time t_1' and t_2' as

$$h\nu = E_m(t_1') - E_m(t_2') = \frac{\Phi C_v/k_B}{\ln(\omega t_1')} - \frac{\Phi C_v/k_B}{\ln(\omega t_2')} = \frac{\Phi C_v/k_B}{\ln(\omega t_1')\ln(\omega t_2')}\ln\left(\frac{t_2'}{t_1'}\right). \tag{6.8}$$

The unknown factors in equation 6.7 can now be substituted with factors from equation 6.8 and with approximating $\ln(\omega t')$ with a constant the energy loss through radiative cooling becomes

$$-E_{\mathrm{rad}}(t_1;t_2) \approx h\nu\left(1 - \frac{1}{\ln(t_2'/t_1')}\int_{t_1}^{t_2}\frac{1}{t'}\,dt\right). \tag{6.9}$$

The energy loss due to depletion is correspondingly

$$-E_{\mathrm{dep}}(t_1;t_2) \approx \frac{h\nu}{\ln(t_2'/t_1')} \int_{t_1}^{t_2} \frac{1}{t'}\, dt. \tag{6.10}$$

The results from equations 6.9 and 6.10 are plotted in figure 6.4, as red and blue dots respectively.

The method of separating thermionic emission from radiative cooling is a proof-of-principle experiment and can be applied to a variety of different clusters and molecules. One condition is that radiation can be considered a continuous process, where the energy of the emitted photon does not exceed the energy width of the distribution that contributes to the decay at any time. As will be shown in the next section, for ZnPc this energy region is little over 3 eV which is well above the energy of an infrared photon. If the molecule is too small, this is no longer the case. The energy loss through emission of one photon can in those molecules be large enough to render the molecule inactive. In the case of C_5^-, which will also be discussed further on, the most IR-active vibrational mode has a frequency of 1831.8 cm^{-1} [95], corresponding to about 0.2 eV, which is a rather large part of the total energy distribution of the molecules, as we will see in section 6.3.

6.2 Radiative cooling and thermionic emission for large molecules

A slightly less sophisticated method of separating the two cooling channels thermionic emission and radiation is through a fitting procedure of the spontaneous decay. This will be exemplified here. The molecules used in this example are the anionic species of 5,10,15,20-Tetrakis[4-(tert-butyl)phenyl]-21H,23H-porphine, molecular structure $C_{60}H_{62}N_4$, hereafter referred to as H_2tBTPP, and zinc phthalocyanine, molecular structure $C_{32}H_{16}N_8Zn$, hereafter referred to as ZnPc. The molecules are presented in Chapter 2.

Both molecules were injected into the ring with a kinetic energy 15 kV and circulated for almost 100 ms before being kicked out and a new bunch let in. The revolution time for H_2tBTPP was 132 μs and for ZnPc 110 μs and neutral particles were detected at the end of one of the straight sections. The first 2.3 ms are reserved for cleaning the beam from isotopomers, fragments and other impurities. Thus these short times are inaccessible for analysis.

Figure 6.6 shows spontaneous thermionic emission from three different days of measurements for each of the two molecules. The neutral counts for each

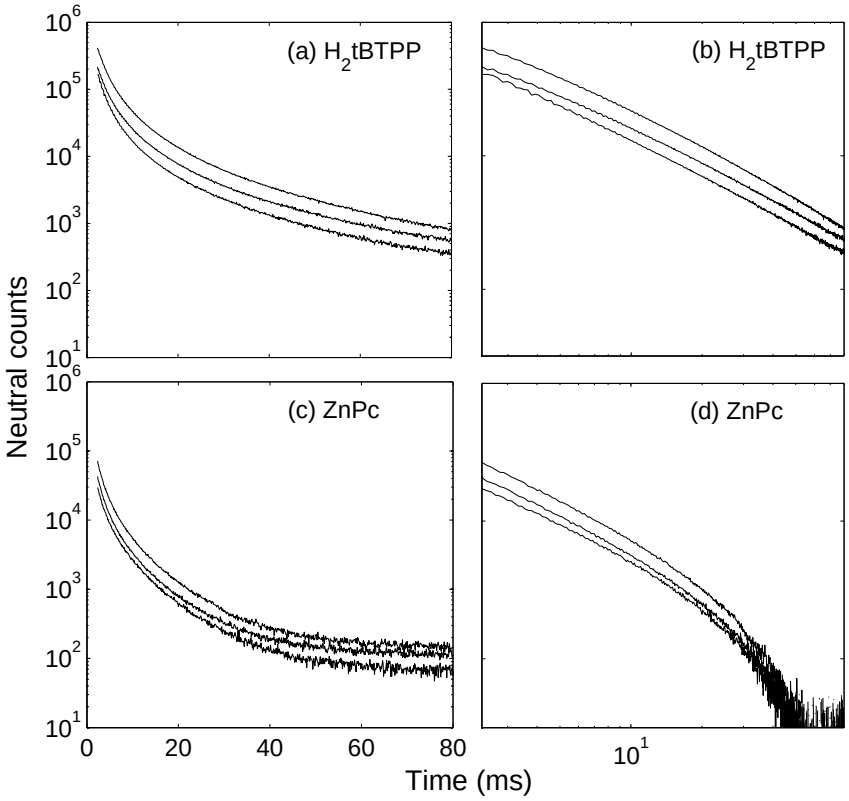

Figure 6.6: Measurement of spontaneous neutralization intensities of the two molecules. (a) and (b) shows H_2tBTPP in both linlog and loglog scale. In (c) and (d) ZnPc is presented in the same scales. In (d) CID with a lifetime of about 8.5 s has been divided out from the neutral counts.

revolution are summed up to one point and the spectrum for each day is the sum of many separate measurements. (a) and (b) show spectra for H_2tBTPP in both linlog and loglog scale, (c) and (d) are the corresponding graphs for ZnPc. When comparing (a) and (c) we detect a comparably larger contribution from CID in the neutralization spectra for ZnPc, as seen by the almost constant detection of neutrals at long times. This contribution is divided out by fitting an exponential function to the counts after 50 ms of storage. The decay time for this contribution is $\tau_{CID} \approx 8.5$ s and is divided out in the plot in (d).

From figure 6.6 we first of all conclude that the decay spectra a reproducible. Secondly, that the decay is clearly non-exponential, as expected from the broad energy distribution resulting from the hot production method. In (b) and (d) there is a difference. (b) shows a nearly linear behavior but not with a slope corresponding to -1, which is what is expected in the absence of radiative cooling and a $1/t$-decay, instead the slope is about -1.7. In (d) we see quicker drop off in intensity, which is an indication of radiative cooling in addition to

the thermionic emission.

6.2.1 H_2tBTPP

As seen in figure 6.6 there is a small curvature on the spectra from this molecule but the dominant feature is the nearly linear behavior in the loglog plot. The slop of approximately -1.7 cannot be explained by the correction to the potential from the $1/\ln(\omega t)^2$-factor. In the case of small particles (containing only a couple of atoms) there is a correction to the power relating to the small heat capacity (see *e.g.* an example regarding Ag_5^- in Hansen *et al.* in ref [96]), but this can hardly have an effect on this rather large molecule.

One possible explanation to the deviation from -1 on the slope in the loglog plot can be a non-uniform initial energy distribution. The reason for such an energy distribution could be parameters in the source such as the power and/or the energy of the laser light used to excite the molecules and it will change if the parameters change [1]. A simple parametrization of the energy distribution is

$$g(E) = ae^{bE}. \tag{6.11}$$

The decay rate is then modified to [1]

$$R \propto -g(E)\frac{dE_{\max}}{dt} \tag{6.12}$$

and by taking the double-logarithm derivative with respect to time we get the power from the decay as

$$\frac{d\ln(R)}{d\ln(t)} = \frac{d}{d\ln(t)}\left[\ln\left(\frac{ae^{bE_{\max}}E_{\max}}{t\ln(\omega t)^2}\right)\right] = -1 - b\frac{\Phi C_v}{\ln(\omega t)^2}. \tag{6.13}$$

With a dimensionless heat capacity of 250, electron affinity $\Phi = 1.7$ eV [58], and $G = \ln(\omega t) \approx 26.9$ and a measured slope of -1.7, the value of b extracted from the data is 1.19 eV^{-1}, corresponding to a change in ion density of a factor 3.3 for each eV.

The decay of this molecule was simulated in the same manner as ZnPc which will be described in detail in the next section. Here only the results from assuming no radiative cooling with both a uniform energy distribution and with a non-uniform initial energy distribution $g(E) \propto \exp(1.19 \cdot E)$ are shown in figure 6.7.

Since the value of b is dependent not on the molecule but on the preparation of the ensemble it is not of fundamental interest, but it seems to be a valid hypothesis for explaining the behavior of the experimental measurements.

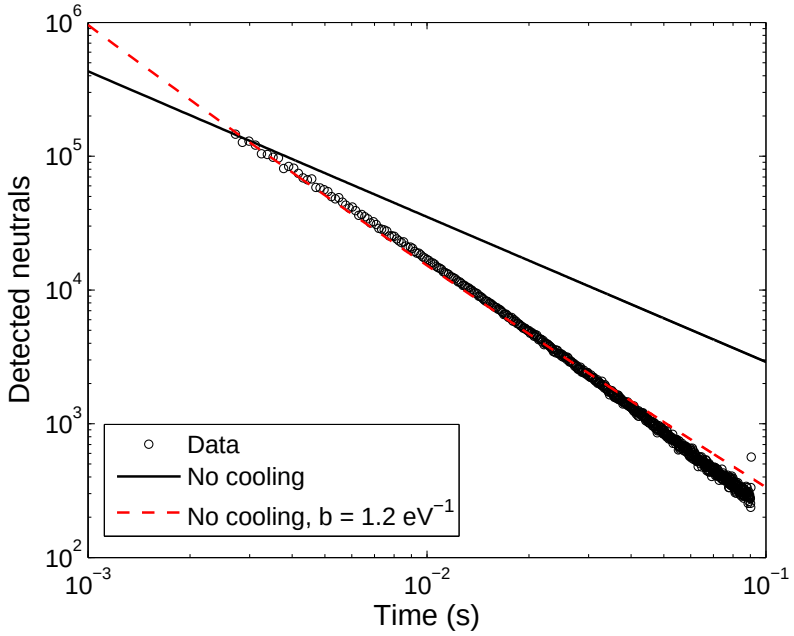

Figure 6.7: Simulated decay with a uniform energy distribution as solid black line and simulated decay with a non-uniform energy distribution as the red dashed line. The measured decay are the small empty circles.

6.2.2 ZnPc

In the case of spontaneous decay of ZnPc we see the typical behavior of thermionic emission being quenched by radiative cooling. The method in section 4.2.3 is used to extract the cooling rate and the emissivity of the molecule.

The frequency factor for thermionic emission is, as was shown in Chapter 4.1.2 $\omega = m_e\sigma_g/(\pi^2\hbar^3)\cdot(k_BT_d)^2 = 4.5\cdot10^7(k_BT_d)^2$ s^{-1} for ZnPc. The electron absorption cross section was estimated with the geometrical area of the molecule which is about 300 Å^2. The daughter temperature is, to first order approximation, $T_d = T_e - \Phi/2C_v$, where the electron affinity $\Phi = 3.8$ eV [56]. Through the relation $\Phi/T_e = \Phi/(T_d+\Phi/2C_v) = \ln(4.5\cdot10^7\cdot(T_d(K))^2\cdot t(=10\,\text{ms}))$, we find the daughter temperature to be about 1450 K, emission temperature about 1600 K and parent temperature about 1750 K (all calculated at $t = 10$ ms). The vibrational levels of ZnPc have been studied with high level density functional theory (DFT) method [57] and using the harmonic oscillator (h.o.) approximation we deduce the caloric curve. Through this the heat capacity was found as a function of temperature and is at the parent temperature $C_v = 13.1$ meV/K ≈ 150 (dimensionless).

The spontaneous decay was fitted to equation 4.41 in section 4.2.3 between $t = 2.3 - 15$ ms after the collision induced dissociation component with a

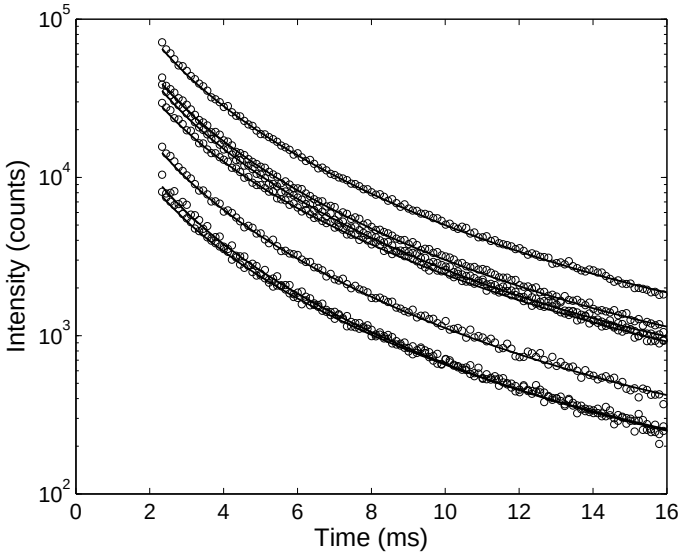

Figure 6.8: Spontaneous decay as small circles and fits as solid lines.

lifetime of about 8.5 s had been divided out. The data together with the fitted functions are shown in figure 6.8. The two fitted parameters a_1 and a_2 are 171 s^{-1} and 3590 s^{-2} respectively which, using equation 4.44, makes $n = 8.2$. As a comparison, the same procedure gives $n = 6.3$ for C_{60}^- where a classical dielectric model predicts a T^6 dependence on the radiative power [97] and hence $n = 6$.

Turning back to equation 4.42 we can now deduce the emissivity of this molecule using the variables extracted from the fits and we get $\epsilon = 1.6 \cdot 10^{-5}$. Using the same procedure with C_{60}-data an emissivity of $4.0 \cdot 10^{-5}$ is found to be compared with $3-8 \cdot 10^{-5}$ deduced from radiative cooling rates found in Andersen *et al.* [98] or $4.5 \cdot 10^{-5}$ reported by Kolodney *et al.* [99].

The radiative cooling rate $\dot{E} = \alpha T^n$ (where the right hand side is a convenient parametrization that will be used below) is also extracted and is about 130 eV/s for ZnPc at the emission temperature $T_e = 1600$ K. For C_{60}^- it is 90 eV/s after a storage time of about 10 ms using this method, which agrees well with the results from section 6.1.2, presented in figure 6.4.

Simulated radiation and thermionic emission

We can check the validity of some of the assumptions made above by simulating the thermionic emission and radiative cooling. The vibrational frequencies were given by [57] and were also calculated using the program *Gaussian* [54].

Using the harmonic oscillator approximation the vibrational energy E_{vib} is

$$E_{vib}(T_c) = \sum_i \frac{h\nu_i \, e^{-h\nu_i/k_B T_c}}{1 - e^{-h\nu_i/k_B T_c}} \tag{6.14}$$

where the temperature T_c is chosen to go from $0 - 4000$ K. The vibrational heat capacity C_v is the derivative of the energy with respect to temperature, or

$$C_v(T) = \sum_i \frac{(h\nu_i)^2/k_B T^2 \, e^{-h\nu_i/k_B T}}{(1 - e^{-h\nu_i/k_B T})^2}. \tag{6.15}$$

Figure 6.9 shows the caloric curve as calculated using equation 6.14 and the heat capacity as a function of temperature using equation 6.15.

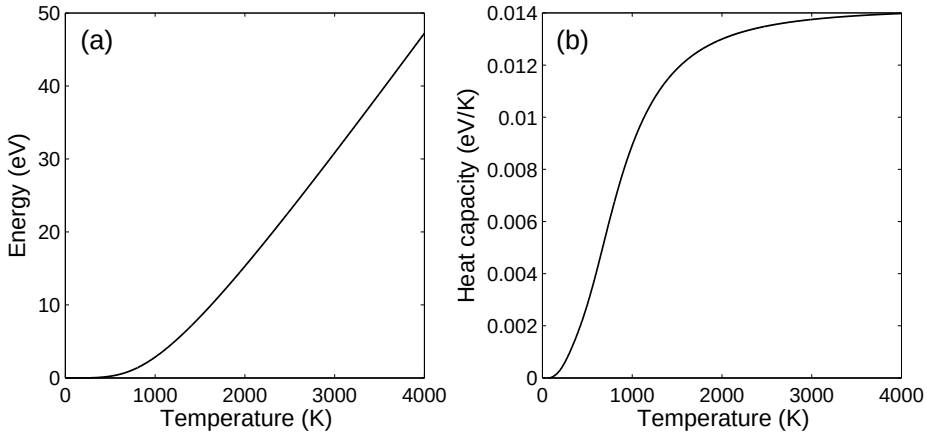

Figure 6.9: The caloric curve is shown in (a) for temperatures up to 4000 K. In (b) the heat capacity is shown as a function of temperature.

The change in temperature of the ions due to radiation is included by solving the differential equation $\dot{E} = C_v \dot{T} = -\alpha T^n$, yielding

$$T(t) = T_c \left(1 + \frac{t}{\tau} \frac{n-1}{\ln(\omega t)}\right)^{-\frac{1}{n-1}}, \tag{6.16}$$

where T_c is the initial temperature and values for n, τ, and $\ln(\omega t)$ are found from the fitting procedure to the experimental data. Through this process the canonical energy E_c is found as a function of time.

The aim here is to calculate the decay rate constant k for this molecule. For this we need the level density, ρ. The caloric curves calculated from the vibrational spectrum discussed above can be converted into the needed level density. The more standard conversion of frequencies to level densities, the Beyer Swinehart algorithm [100], is more computationally heavy for the relatively large system but is used for calculations of C_5^-, see below.

The canonical energy E_c is found as a function of temperature and time at steps equidistant in temperature. To get them equidistant in energy instead we create an energy vector from 0 eV to the maximum energy in figure 6.9(a) and transform the temperature to a microcanonical temperature iteratively by using the caloric curve in figure 6.9 and

$$E_c(T) = E_m + k_B T. \tag{6.17}$$

This equation is solved iteratively by

$$T_m(E_m) = T' + \frac{E_m + k_B T - E_c(T')}{C_v(T')}. \tag{6.18}$$

which usually takes no more than four iterations.

To find the level densities needed to calculate the rate constant, the relation between the canonical partition function and the level densities is utilized as

$$Z_c = \int \rho(E) \exp(\beta E)\, \mathrm{d}E \tag{6.19}$$

and through inverse Laplace transform (see reference [1] for details on this) the approximate relation between the canonical values and the level density is found to be

$$\rho(E_m) \approx Z(\beta) e^{\beta E_m} \frac{1}{\sqrt{2\pi T^2 C_v}}, \tag{6.20}$$

where E_m is the microcanonical energy of the particle.

The partition function $Z(T)$ is thus needed for the calculation of the level density and it is

$$\ln Z(T) = \sum_i - \ln(1 - e^{-h\nu_i / k_B T}). \tag{6.21}$$

Figure 6.10 shows plots of the partition function and the level density.

To simulate the decay of the molecules the decay constant $k(E, \epsilon)$ for thermionic emission deduced from detailed balance theory is used,

$$k(E, \varepsilon)\, d\varepsilon = 2 \frac{m_e}{\pi^2 \hbar^3}\, \varepsilon\, \sigma(E, \varepsilon)\, \frac{\rho(E - \Phi - \varepsilon)}{\rho(E)}\, \mathrm{d}\varepsilon, \tag{6.22}$$

where ε is the kinetic energy of the emitted electron and $\sigma(E, \varepsilon)$ is the capture cross section for the reverse process. We make the assumption that a good approximation of the cross section is the energy independent geometrical cross section, σ_g, and then integrate out the ε-dependence. Left is now

$$k(E_m) = 2 \frac{m_e}{\pi^2 \hbar^3}\, (k_B T_d(E_m))^2\, \sigma_g\, \frac{\rho(E_m - \Phi)}{\rho(E_m)}. \tag{6.23}$$

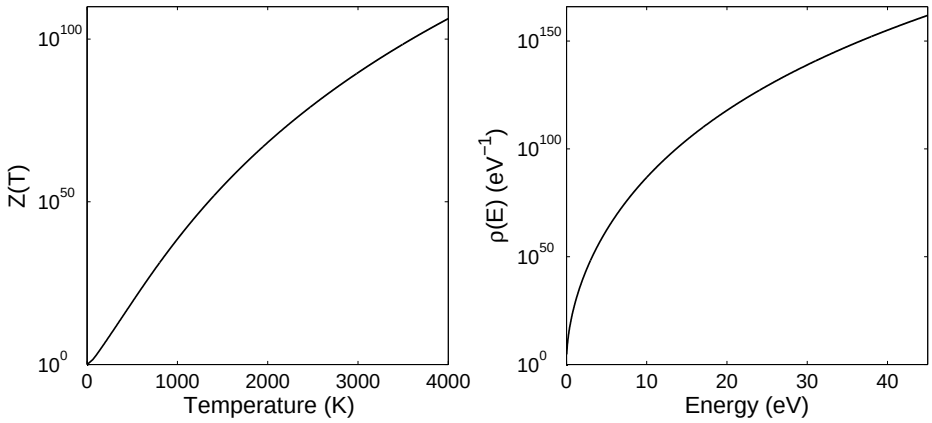

Figure 6.10: The calculated partition function and level densities of ZnPc.

Everything preceding the ratio of level densities goes into the frequency factor, which becomes $\omega = 4.5{\cdot}10^7\ (T_d(\mathrm{K}))^2\ \mathrm{s}^{-1}$. Equation 6.23 is plotted in figure 6.11, with $\sigma_g = 300$ Å^2 and electron affinity $\Phi = 3.8$ eV. With a storage time of 100 ms and a clean up time in the ring of at least 1 ms, the energy region contributing to the detected decay is a little over 3 eV, between $14.6-17.8$ eV internal energy.

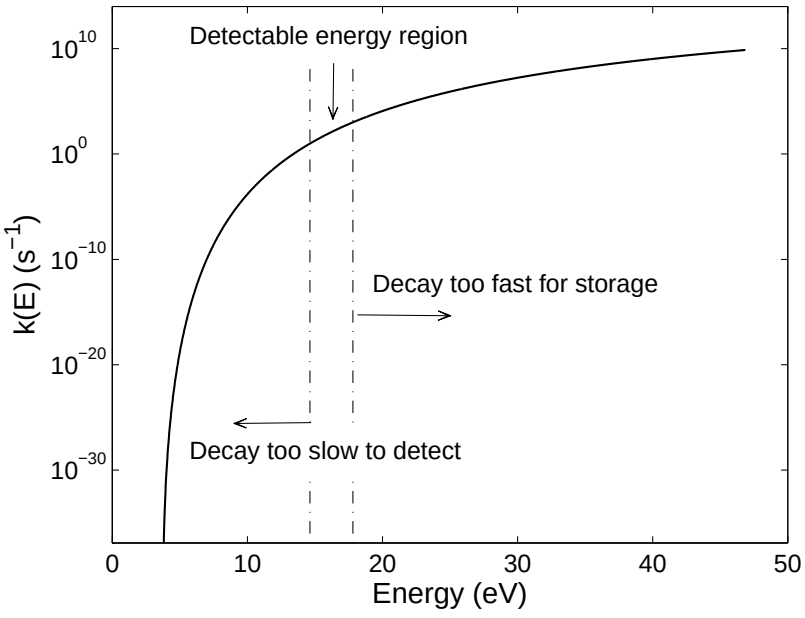

Figure 6.11: The decay rate constant k as a function of internal energy. The experimentally important energies are labeled as detectable energy region.

If a broad energy distribution of the ions from the start is assumed, and that

they are immediately isolated from all kinds of interactions (also absorption and emission of radiation) when entering the ring, the ions' excitation energy E is conserved and they will decay individually according to the radioactive decay law with the rate constant $k(E)$. The detected neutral product $I(t)$ is then

$$I(t) = \int k(E)\, g(E,0)\, e^{-k(E)t}\, \mathrm{d}E, \tag{6.24}$$

where $g(E,0)$ is a time independent energy distribution. In figure 6.12 $I(t)$ is plotted with $g(E,0) \equiv 1$ as the black line both in linlog and loglog plot. The shape is very close to a $1/t$-curve as is expected from a sum over many many individual exponential decay curves. More exact, the slope is -1.079 to be compared to a slope of -1.085, which is what you get from the expression $1/(\ln(\omega t)^2 t)$ with $\omega = 4.5 \cdot 10^7 \cdot (T_d = 1450K)^2$. If cooling by radiation is

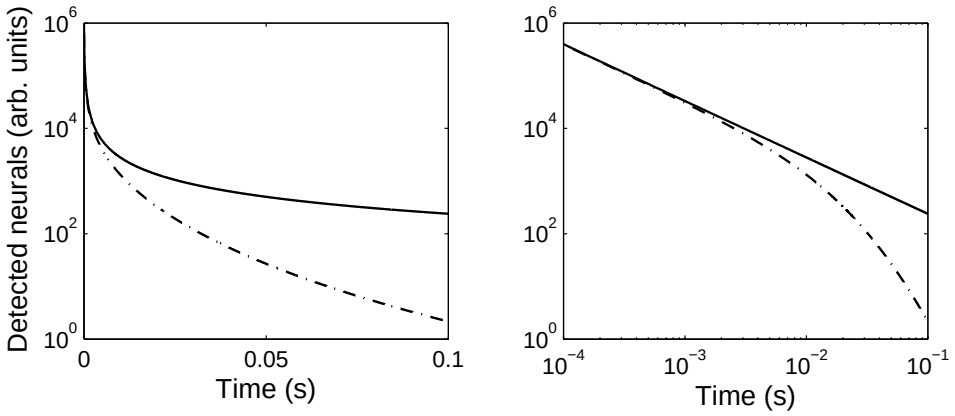

Figure 6.12: Simulated detected neutrals with a flat constant energy distribution without interactions from the surrounding environment (solid black line) and with the inclusion of radiative cooling (dot-dashed line). The right figure shows the loglog plot of the same detected neutrals signal.

included (*i.e.* a time dependence of the internal energy) the time-dependent distribution becomes

$$g(E,t) = g(E,0)\, e^{-k(E)t}, \tag{6.25}$$

where the starting point is a flat energy distribution equal to 1 at time equal to zero. The energy distribution at a couple of representative times ($t = 0, 1, 10, 100$ ms) is shown in figure 6.13.

The detected neutrals when the time dependence of the internal energy is included and thus the reduction in $k(E)$ is calculated as

$$I(E(t),t) = \sum_E g(E(t),t) \cdot k(E(t)) \tag{6.26}$$

and is plotted as the dot-dashed line in figure 6.12. The radiative time used here is $\tau = 5.8$ ms as found in the fitting procedure of the experimental data.

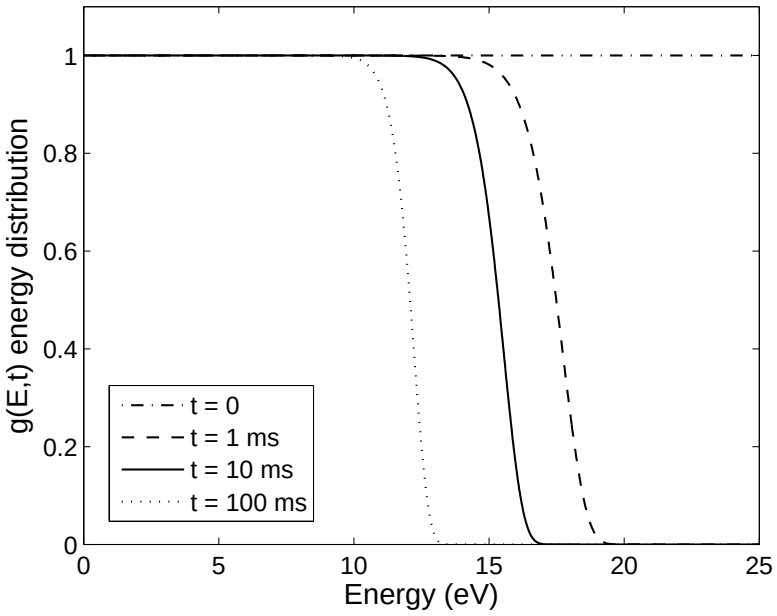

Figure 6.13: The simulated time evolution of the energy distribution $g(E,t)$ at times $t = 0, 1, 10, 100$ ms.

Finally, the simulated decay profiles are compared with the experimental data presented earlier. Figure 6.14 shows the simulated decay with and without radiation together with experimental data. The simulations that include radiative cooling are plotted with two radiative times; 5.8 ms and 2.9 ms. The simulations are normalized to the first measurement point at $t = 2.3$ ms.

The hypothesis of a non-uniform energy distribution is also tested. By fitting a slope to the first 5 ms of the experimental decay curves, the value of b is deduced in the same way as in section 6.2.1 and we get $b = 0.85$ eV^{-1}. This is included in the time dependent energy distribution with a radiative time of 5.8 ms.

As is apparent, the non-radiative decay is not a good fit. Also, only including the radiative time found from the fitting procedure ($\tau = 5.8$ ms), does not provide the best fit either. The simulation using a non-uniform initial energy distribution provides a reasonable fit at early times but fails to follow the entire curvature of the measured data. The best fit is provided when using half of the radiative time found from the fitting-procedure to the experimental data in the simulation, $\tau = 2.9$ ms. Since the first 2.3 ms of neutralization data is unavailable because of the clean up procedure, perhaps this missing information would yield a better fit with a larger curvature to the experimental data, thus yielding a shorter radiative time.

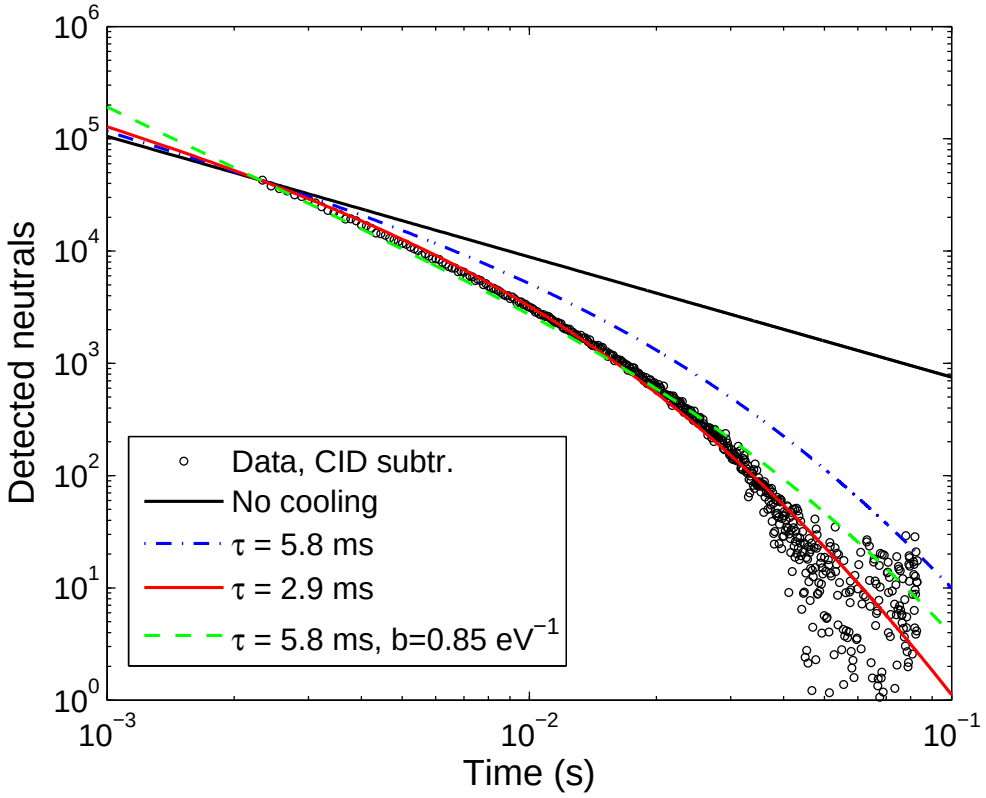

Figure 6.14: The detected neutrals when internal energy loss from radiation is included and experimental data from one day of measurement. Collision induced decay has been divided out. Radiative times of 5.8 ms and 2.9 ms from the simulation are displayed. The result from a non-uniform starting energy distribution with a radiative time of 5.8 ms is displayed as the green dashed line.

6.3 Energy distribution of C_5^-

Spontaneous and laser induced decay for initially hot C_5 anions was measured in the same storage ring as the previously described experiments. The biggest difference between C_5^- and the other three molecules is its size. By containing only five atoms the heat capacity of this molecule is much smaller than the others. Nevertheless, delayed thermionic emission after one photon absorption was detected, indicating a, at least partial, statistical redistribution of energy between its degrees of freedom.

The story presented here is about the energy distribution and radiative cooling of C_5^- and how it can be probed by adding a well defined amount of energy at a well defined time to a initially hot ensemble that spontaneously cools with time.

6.3.1 Experimental procedure

The molecules were created in a laser desorption source and injected into the ring with a kinetic energy of 15 keV. With a mass to charge ratio of 60 amu/e, the revolution time is 35.5 μs. Two kick-out pulses were applied to clean up the beam of unwanted species with the last one at 0.3 ms, rendering times earlier than that unavailable for measurements.

At various times of storage (between $1 - 90$ ms) a laser beam was fired and the enhanced neutral yield was detected at the end of the next straight section. Prompt decay resulting from photoabsorption is thus not measured. Photon energies between $1.85 - 2.75$ eV with a fluence below 6.1 mJ, typically $3 - 4$ mJ, per pulse were used to excite the molecules once in the ring. Measuring a linear dependence of the enhanced signal as a function of the laser pulse fluence indicates that we are in the one-photon absorption region.

An example of a measured spectrum with photon energy of 2.64 eV and storage time 20 ms is shown in figure 6.15.

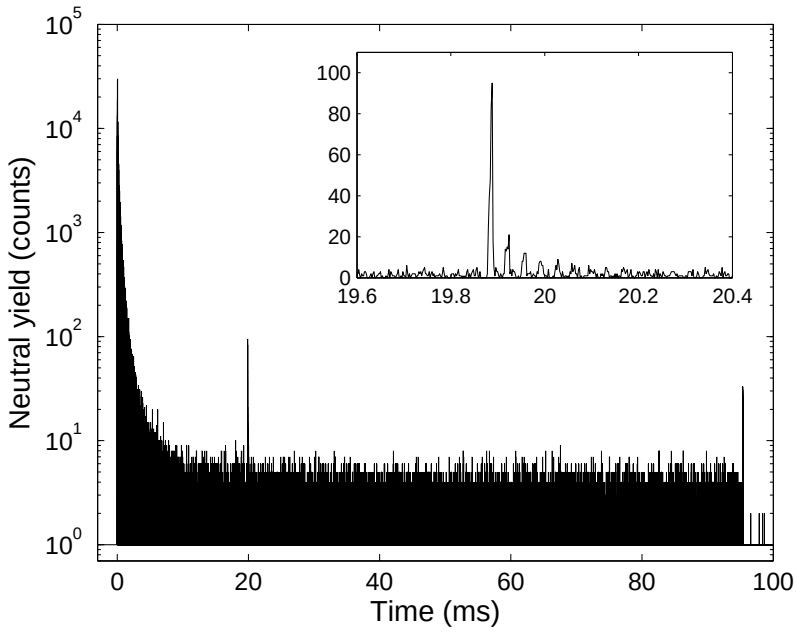

Figure 6.15: Neutralization spectrum with $t_{\text{laser}} = 20$ ms and with photon energy of $h\nu = 2.64$ eV and a pulse energy of 1.8 mJ. The inset shows an enlarged view of the enhanced peaks after photo absorption.

To compare the neutral yield measured at different storage times and with different photon energies a normalization procedure is needed. In each spectrum I the first two revolutions after the laser pulse are summed together and

labeled I_{p}. To normalize to the number of photons hitting the bunch, I_p is multiplied with the photon energy $h\nu$ and divided by the laser power P. Because the beam spreads out in time the width of the beam (w) is also multiplied with I_{p}. Because neutralization occurs spontaneously at short times and through CID at longer times, this contribution needs to be subtracted from I_{p}, using a reference spectrum I_{ref} normalized to the number of ions in the enhanced spectrum. Finally, I_{p} is normalized to the number of ions in the beam by multiplying it with the sum of the counts in I_{ref} before the laser pulse, divided by the sum of I over the same time span and divided by the total number of counts in I_{ref}. Equation 6.27 shows the normalization procedure where prp refers to *peaks pre laser pulse* and tot to total number of counts in the spectrum. The enhanced and normalized signal is labeled I_e.

$$I_e = \underbrace{\frac{\sum_{\mathrm{prp}} I_{\mathrm{ref}}}{\sum_{\mathrm{prp}} I \sum_{\mathrm{tot}} I_{\mathrm{ref}}}}_{1} \underbrace{\frac{w\, h\nu}{P}}_{2} \left(I_{\mathrm{p}} - \underbrace{I_{\mathrm{p,ref}} \frac{\sum_{\mathrm{prp}} I}{\sum_{\mathrm{prp}} I_{\mathrm{ref}}}}_{3} \right) \tag{6.27}$$

1 – Normalization to number of ions in beam

2 – Normalization to number of photons

3 – Subtraction of normalized reference spectrum

It should be noted that this normalization procedure does not account for overlap between the laser beam and the ion bunch, or for betatron oscillations. The normalized counts I_e for a couple of photon energies at different laser firing times can be seen in figure 6.16.

As is seen in figure 6.16 the enhanced signal peaks at different storage times depending on the photon energy. The reason for this and what properties of C_5^- that can be extracted from these measurements will be discussed in the next section.

6.3.2 Results and discussion

The enhanced signal detected is the sum of the first two revolutions after laser excitation. This means that the time window for detection is between 17.7 μs (half a revolution) and 54 μs (one and a half revolution) after the laser pulse was fired. As seen in figure 6.11 the detectable excitation energies are determined by the decay constant together with the window of time in which detection takes place. Molecules heated up to an energy that corresponds to a decay constant with a much faster decay than the lower limit of the decay window will not be detected. The same goes for molecules cold enough that even with an additional photon energy they are not hot enough to release their extra electron. Figure 6.17 shows a schematic sketch of the process.

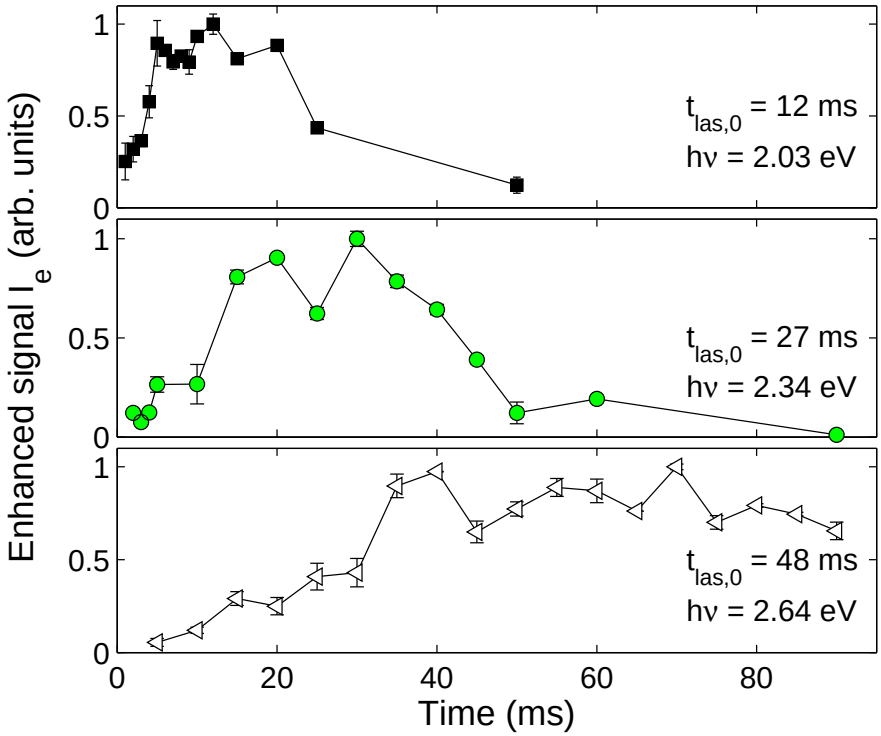

Figure 6.16: Normalized enhanced signal for photon energies 2.64, 2.34, and 2.03 eV at different laser firing times. The laser firing times corresponding to the maximum yields are written out in the corresponding figures.

The energy distribution resulting in the measured signal in figure 6.16 cannot be flat. A flat energy distribution would not give a signal that is low for short times, it could however give a decrease in the signal at the longer storage times due to energy loss from radiative cooling. Because the maximum in the enhanced signal shifts to longer storage times with larger photon energies the energy distribution must shift with time, and as is apparent from the spectrum in figure 6.15, after about 4 ms it does not happen through thermionic emission. Radiative cooling is the only accessible channel.

The decay rate constant for electron emission is given by equation 4.17. The capture cross section used was the Langevin cross section, here expressed as

$$\sigma = \left(\frac{2\alpha_p}{\varepsilon}\right)^{1/2}, \tag{6.28}$$

where α_p is the polarizability of C_5 and ε is the kinetic energy of the electron. Because of the small values for the kinetic energy the cross section in equation 6.28 will be significantly larger than the geometric cross section. The Beyer-Swinehart algorithm was used to calculate the vibrational level densities and the value for the electron affinity used was 2.8 eV.

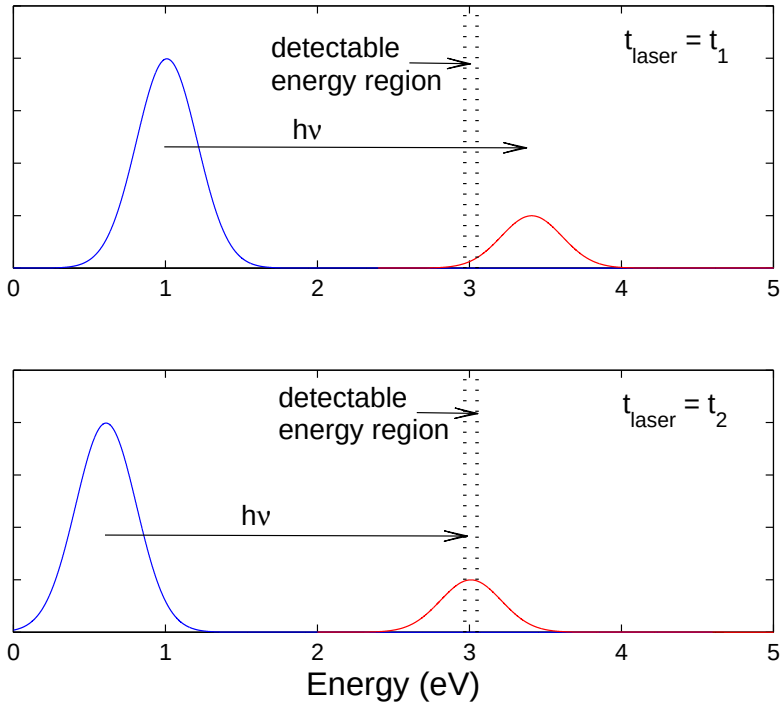

Figure 6.17: Sketch of the process of moving a part of the energy distribution up in energy and the energy window (corresponding to a time window) where neutralization can be detected. The storage time in the upper frame is shorter than the lower, $t_1 < t_2$. In the situation in the upper frame a small enhanced signal is detected whereas in the situation in the lower frame I_e is at its peak. The energy distributions are generic.

The center and width of the excitation energy distribution of the ions which will decay by thermionic emission in the time window experimentally available was found to be 2.935 eV with a standard deviation of 0.055 eV. It was calculated using $k(E)\exp(-k(E)t)$ for $t = 17.7$ μs. We call this center energy E_0.

The enhanced signal I_e will then be given by

$$I_e(h\nu, t_{las}) \propto \sigma(h\nu) g(E_0 - h\nu; t_{las}), \tag{6.29}$$

where the constant of proportionality is related to detection efficiency and universal due to the normalization procedure. For a given photon energy the peak in the distribution vs. laser firing time is identified as $E_m = E_0 - h\nu$ and the corresponding laser firing time is denoted $t_{las,0}$. The relation between the two is found experimentally to be $E_m \propto t_{las,0}^{-0.56}$. This fit does not take into account that the distribution changes with time. The time dependance means that the peak in the yield vs. time does not correspond to the peak vs. energy.

The yield vs. t_{las} can be converted to a yield as a function of energy at the time

$t_{las,0}$ by the transformations

$$E(t_{las,0}) = (E_0 - h\nu)\left(\frac{t_{las}}{t_{las,0}}\right)^{0.56} \tag{6.30}$$

and

$$g(E(t_{las,0}); t_{las,0}) \propto I_e(h\nu, t_{las})\left(\frac{t_{las}}{t_{las,0}}\right)^{-0.56}. \tag{6.31}$$

This transformation requires that ions cool with identical rates when they have identical energies, irrespective of initial energy. The fitting procedure is thus repeated with the corrected yield as explained above. This corrected curve can be seen in figure 3 of Paper IV and the relation is fitted well by a powerlaw as

$$E_m = 2.935\text{ eV} - h\nu = 0.43 \pm 0.13\text{ eV} \times \left(\frac{t_{las,0}}{1\text{ms}}\right)^{-0.58\pm0.10}, \tag{6.32}$$

where the uncertainties are from the fit. The relation between how energy goes with time (as $t^{-0.58}$) can be related to the emitted power of the molecule with the assumption that it cools as

$$P = \dot{E} = \alpha T^n. \tag{6.33}$$

This is the same assumption made for the larger molecule in section 6.2.2 and described in section 4.2.3 with the same definition of α. To find n we use the canonical relation between the energy and temperature through the heat capacity. Between $0.2-1.1$ eV it is $E = 0.447\,\text{K}\,(T\,[\text{K}])^{1.38} \equiv aT^\gamma$, calculated using the caloric curve from the vibrational frequencies. Solving the differential equation 6.33 yields

$$E = \left(E(t=0)^{1-n/\gamma} + \frac{\alpha a^{-n/\gamma}}{n/\gamma - 1}\right)^{-\frac{1}{n/\gamma-1}}, \tag{6.34}$$

where because of the very quick onset of radiative cooling the first term can be ignored and the data in figure 3 of Paper IV can be fitted to the second term only. A good fit to the slope of the line was found with $n = 3.8$.

So the radiative power was found to go as $T^{3.8}$ which is a weaker temperature dependence than *e.g.* C_{60}^- with $n = 6$ or $ZnPc^-$ which was found to have a temperature dependence of $n \approx 8$. For Al_4^- cluster however, Toker *et al.* [101] found a similar temperature dependence of the radiative cooling as our value for C_5^-. By storing their clusters in a electrostatic ion beam trap and radiating them with photons after different storage times they were able to deduce the ion temperatures and found a cooling proportional to $T^{3.5\pm0.2}$.

At present it is not clear how general the observation of high n for large carbon systems and low n for small carbon ions is.

CHAPTER 7

Summary

The study of the thermal properties of clusters and molecules is a vast and exciting field where there is still much to discover. The work presented in this thesis covers aspects of the three main processes included in unimolecular decay; evaporation, thermionic emission, and radiative cooling.

Spontaneous evaporation from different types and sizes of water clusters were measured in this work. Allowing initially hot clusters to spontaneously evaporate is a gentle method of studying energetic features. It was possible to draw conclusions based on consideration of the evaporative ensemble where, for a given time, there is a maximum temperature in the ensemble which is related to the heat capacity of the species. In this way, size-dependent heat capacities of freely evaporating negative and positive water clusters of sizes between five and 300 molecules were determined. For clusters containing more than 21 molecules, the heat capacity per molecule lies in the intermediate region between those for bulk ice and liquid water.

Measurements of the relative fraction of evaporation from protonated mixed water-ammonia clusters yielded the result that water evaporation dominated for most cluster containing five or less ammonia molecules. Cluster sizes with a total of three to eleven molecules and one series of 16 molecules were studied.

The experiments on small mixed water and deuterated water clusters with a core ion of ammonium showed that very little hydrogen scrambling occurred. The relative evaporation rates for H_2O:HDO:D_2O were determined to be $1 : 0.71 : 0.56$. The procedure of measuring evaporation of different species from the same parent cluster eliminates the systematic uncertainties related to different initial states.

A novel method of determining absolute cooling rates was applied to measurements on C_{60}^- in an electrostatic storage ring. The method is based on the non-exponential decay of the excited fullerene population, in combination with single photon reheating. The deviation from a $1/t$-decay was used to

separate the radiative cooling rate from cooling by thermionic emission. It was found that radiative cooling becomes the dominant cooling process already after 5 ms. Radiative cooling rates are difficult to measure directly for isolated particles and this method demonstrates that it is possible to measure time resolved cooling rates for a wide timespan through electron emission measurements.

The emissivity and cooling rates for another large carbon containing molecule, zinc phtalocyanine (ZnPc), were investigated by considering the spontaneous electron emission curves. A simulation of ZnPc based on detailed balance theory for the decay rate constant showed good agreement with the measurements. The emissivity and radiative cooling time were found to be similar to that of C_{60}^-. A type of porphyrin, H_2tBTPP, was studied using the same procedure where the thermionic emission rate was explained by a non-uniform energy distribution of the ions when entering the storage ring.

Finally, the radiative cooling rate of the comparatively small molecule C_5^- was measured. From measurements on laser induced electron emission it is clear that the energy distribution of the ions is not flat, and furthermore that it changes over time through radiative cooling. The cooling rate was determined by the dependence of the photoinduced neutralization yield vs. photon energy and laser firing time.

In this work it has been shown that through relatively easy experiments a lot of information can be obtained about clusters and molecules and their energetic properties. Using the systematics associated to unimolecular decay and the evaporative ensemble properties such as the heat capacity, relative evaporation rates, thermionic emission rates, radiative cooling rates, and emissivity have been obtained. Most methods used here are quite general and can be applied to a variety of different molecules and clusters.

Acknowledgements

A thesis is not something that writes itself or gets written by one person. Well, technical I guess I wrote it, but figuratively it takes a village. So many people have contributed or supported me in other ways, that I hardly know where to start.

First I would like to thank my supervisor Klavs Hansen for accepting me as a PhD-student all those years ago and for introducing me to and guiding me through the exciting, but at times, tricky world of clusters. I have learned a lot from you. My assistant supervisor Patrik Andersson also deserves thanks for the all the support he has given me and for sharing his expertise in, among other things, atmospheric science. Eleanor Campbell was my examiner during the first three years of my PhD-education and also the one to introduce me to the group formerly known as the Atomic and Molecular Physics-group as a Master-student. She is a source of inspiration and I am also very grateful for her comments on this thesis. I am also thankful to Hans Starnberg who accepted the role as my examiner after Eleanor left Gothenburg and for his help over these last couple of months.

I have been fortunate with excellent teachers throughout my entire schooling, but I think the one that first seriously awakened my curiosity for the natural sciences was my math and chemistry teacher in 7th grade, Inga Häger. One day she gave us an old matchbox (of the larger kind), taped together containing some unknown objects, and asked us to shake it, hold it, tilt it, to find out what was inside. We had some guesses; maybe some balls, bolts, perhaps a screw? When we were done she said 'This is scientific research, you shake, hold, look, smell, and then make an educated guess'. She then refused to reveal what she put inside the box. First it really irritated me, then it triggered me to want to know more, not necessarily about the content of the matchbox, but about the world and how new discoveries related to it were made. After having taught a wide variety of students and children myself during these five years, I don't know how these great teachers do it, how they keep their enthusiasm going year after year after year. But I'm grateful for it.

Returning to present day, there are lots more people in the group to thank and Anton should be the first one out. His help with everything has been

invaluable, his enthusiasm for physics contagious, and his tireless efforts in making this place a pleasant and fun place to work very appreciated. My first office-mate Mikael was also a great help and fun company during my first couple of years here, and how he managed to write a thesis and graduate with me talking to him all the time I do not understand now. After Mikael left Motoshi came and filled the seat. Motoshis knowledge of particularly storage rings and his subtle sense of humor both helped me in the research, and cheered me up.

Bertil has been a valuable support and a good discussion partner during the process of my studies and Mats' knowledge in instrumentation and computers have made the work much easier. For always having his door open to all kinds of questions and quandaries I want to thank Dag. Thanks should also go to Bea, Johanna, and Rosie at the administration for their support in everything and all concerning the practical aspects of traveling, courses, and various forms.

One year of my time as a PhD-student has been spent on teaching, where the bulk part of this time consisted of making ice-cream for little kids. It might seem like an easy task, but then you don't know kids! What made it fun were my great co-workers; first Gustav who taught me the trade and then Anna-Karin who we quickly recruited to take his place when he retired.

Other past and present PhD-students, with whom I've studied for courses, taught students along side, sat in various committees, or just had coffee-breaks, have all brighten my days and broaden my horizons. Some of them are Niklas, Sasa, Stina, Daniel, Staffan, Johannes, Fabio, Anders, Pontus, Johan, Fredrik, Emma, Erik, Camilla, Erik, Robert, Vladimir, Martin, Martin, and Martin (yes, there were three, and all at the same time).

I also want to thank all other past and present members of Level 8 physics for creating such a nice and stimulating atmosphere to work in.

The works presented in this thesis have been performed at two sites outside the University of Gothenburg. The water cluster experiments were carried out at the University of Aarhus, where I much enjoyed working with, among others, Kristian Støchkel, Umesh Kadhane, Maj-Britt Suhr Kirketerp, Preben Hvelplund, Jens Ulrich Andersen, and Steen Brøndsted Nielsen. The storage ring experiments were performed at Tokyo Metropolitan University where my co-workers have been numerous but among those who must be mentioned and thanked are Motoshi Goto (again), Jun Matsumoto, Haruo Shiromaru, and Yu Zama. The whole physics and physical chemistry-group deserves many thanks for taking such good care of us in Japan and showing us a good time. Especially at the time of the earthquake their calmness and helpfulness was of great support and comfort to me.

I am fortunate to have a number of very good friends who I can always rely on for support and encouragement when things look bleak, but also for good times with game-nights, cheese-clubs, pub-rounds, and other less organized events. I won't mention you all by name but I hope you know who you are and that I appreciate you a lot! Two that must be mentioned however are Petter and Frida. Petter for the daily interactions, the discussions on everything and nothing, the encouragement, and all the fun activities. Frida for even though there might go months between our visits, I know I can count on you if and when I need to.

Last, but not least, I want to thank my family. Your love and support have gotten me to this point and I could not have done it without you! To my sister Åsa, you've lived here and there and everywhere by now, but you are always here for me when it matters. Thank you all.

Erika Sundén
Göteborg, February 2012

BIBLIOGRAPHY

[1] K. Hansen, *Notes on statistical physics of nanoparticles*, to be published

[2] H. W. Kroto, J. R. Heath, S. C. O'Brien, R. F. Curl, and R. E. Smalley, *Nature* **318** (1985) 162

[3] M-C. Daniel, and D. Astruc, *Chem. Rev.* **104(1)** (2004) 293

[4] W. D. Knight, K. Clemenger, W. A. de Heer, W. A. Saunders, M. Y. Chou, and M. L. Cohen, *Phys. Rev. Let.* **52** (1984) 2141

[5] T. P. Martin, *Phys. Rep.* **273** (1996) 199

[6] L. N. Lewis, *Chem. Rev.* **93** (1993) 2693

[7] J. Tejada, E. M. Chudnovsky, E. del Barco, J. M. Hernadez, and T. P. Spiller *Nanotechnology* **12** (2001) 181

[8] M. Wang, C. Ma, H. Wen, and C. Chen *Dalton Trans.* (2009) 994-1003

[9] L. Hackenmüller, K. Hornberger, B. Brezger, A. Zeilinger, and M. Arndt, *Nature* **427** (2004) 711

[10] R. P. Wayne, *Chemistry of Atmospheres*, 3rd ed., Oxford University Press, 2000

[11] J. Curtius, E. R. Lovejoy, and K. D. Froyd, *Space Science Rev.* **125** (2006) 159

[12] E. R. Lovejoy, J. Curtius, and K. D. Froyd *J. Geophys. Res.* **109** (2004) D08204

[13] F. Yu, and R. P. Turco, *J. Geophys. Res.* **106** (2001) 4797

[14] C. T. R. Wilson, *Proc. Royal Soc. of London, Series A.* **85(578)** (1911) 285

[15] W. C. Hinds, *Aerosol technology: properties, behaviour, and measurement of airborne particles*, 2nd ed., John Wiley & Sons, United States of America, (1999) chap. 13

[16] J. Kirkby *et al.*, *Nature* **476** (2011) 429

[17] D. J. Coffman and D. A. Hegg, *J. of Geophys. Res.* **100(D4)** (1995) 7147

[18] U. Buck and F. Huisken, *Chem. Rev.* **100** (1982) 3863

[19] J. Q. Searcy and J. B. Finn, *J. Chem. Phys.* **61** (1974) 5282

[20] S.-S. Lin, *Rev. Sci. Instr.* **44(4)** (1973) 516

[21] V. Hermann, B. D. Kay, and A. W. Castleman Jr., *Chem. Phys.* **72** (1982) 185

[22] O. Echt, D. Kreisle, M. Knapp, and E. Recknagel, *Chem. Phys. Let.* **108(4)** (1984) 401

[23] D. Kreisle, O. Echt, M. Knapp, and E. Recknagel, *Surf. Science* **156** (1985) 321

[24] K. Hansen, P. U. Andersson, and E. Uggerud, *J. of Chem. Phys.* **131** (2009) 124303

[25] T. Schindler, C. Berg, G. Nieder-Schatteburg, and V. E. Bondybey, *Chem. Phys. Let.* **250** (1996) 301

[26] N. Agmon, *Chem. Phys. Let.* **244** (1995) 456

[27] M.-C. Bellissent-Funel and J. Teixeira *J. of Mol. Struc.* **250** (1991) 213

[28] Z. Sun, C.-K. Siu, O. P. Balaj, M. Gruber, V. E. Bondybey, and M. K. Beyer, *Angew. Chem. Int. Ed.* **45** (2006) 4027

[29] D. Smith, N. G. Adams, and M. J. Henchman, *J. Chem. Phys.* **72(9)** (1980) 4951

[30] K. Honma and P. B. Armentrout, *J. Chem. Phys.* **121(17)** (2004) 8307

[31] P. U. Andersson, M. J. Ryding, O. Sekiguchi, and E. Uggerud, *Phys. Chem. Chem. Phys.* **10** (2008) 6127

[32] S. T. Graul, M. D. Brickhouse, and R. R. Squires *J. Am. Chem. Soc.* **112** (1990) 631

[33] J. Wölk and R. Strey, *J. Phys. Chem. B* **105** (2001) 11683

[34] J. A. Smith, F. E. Livingstone, and S. M. George, *J. Phys. Chem. B* **107** (2003) 3871

[35] M. Meot-Ner (Mautner), *Chem. Rev.* **105** (2005) 213

[36] H. H. Bueker, and E. Uggerud, *J. Phys. Chem.* **99** (1995) 5945

[37] F. Brugé, M. Bernasconi, and M. Parrinello, *J. Chem. Phys.* **110** (1999) 4734

[38] S. Karthikeyan, J. N. Singh, M. Park, R. Kumar, and K. S. Kim, *J. Chem. Phys.* **128** (2008) 244304

[39] J. Douday, F. Calvo, and F. Spiegelman, *J. Chem. Phys.* **129** (2008) 154305

[40] E. P. L. Hunter, and S. G. Lias, *J. Phys. Chem. Ref. Data* **27** (1998) 413

[41] Y.-S. Wang, H.-C. Chang, J.-C. Jiang, S. H. Lin, Y. T. Lee, and H.-C. Chang, *J. Am. Chem. Soc.* **120** (1998) 8777

[42] J. C. Jiang, H.-C. Chang, Y. T. Lee, and S. H. Lin, *J. Phys. Chem. A* **103** (1999) 3123

[43] C. A. Deakyne, *J. Phys. Chem.* **90** (1986) 6625

[44] H. Shinohara, N. Nishi, and N. Washida, *Chem. Phys. Let.* **153(5)** (1988) 417

[45] P. Hvelplund, T. Kurtén, K. Støchkel, M. J. Ryding, S. Brøndsted Nielsen, and E. Uggerud, *J. Phys. Chem. A* **114** (2010) 7301

[46] W. Krätschmer, K. Fostiropoulos, and D. R. Huffman, *Chem. Phys. Let.* **170** (1990) 167

[47] K. S. Novoselov, A. K. Geim, S. V. Morozov, D. Jiang, Y. Zhang, S. V. Bubonus, I. V. Grigorieva, and A. A. Firsov, *Science* **306** (2004) 666

[48] S. Iijima, *Nature* **354** (1991) 56

[49] C. Brink, L. H. Andersen, P. Hvelplund, D. Mathur, and J. D. Voldstad, *Chem. Phys. Let.* **233** (1995) 52

[50] X.-B. Wang, H.-K. Woo, and L.-S. Wang, *J. Chem. Phys.* **123** (2005) 051106

[51] S. Tomita, J. U. Andersen, K. Hansen, and P. Hvelplund, *Chem. Phys. Lett.* **382** (2003) 120

[52] A. Y. Vul', *Perspectives of Fullerene Nanotechnology* Springer Netherlands (2002) 23

[53] U. Weiler, T. Mayer, W. Jaegermann, C. Kelting, D. Schlettwein, S. Makarov, and D. Wöhrle, *J. Phys. Chem. B* **108** (2004) 19398

[54] Gaussian 09, Revision A.01, M. J. Frisch *et al.*, Gaussian, Inc., Wallingford CT, 2009

[55] W. Gao and A. Kahn, *Organic Electronics* **3** (2002) 53

[56] T. G. Gantchev, J. E. van Lier and D. J. Hunting, *Rad. Phys. and Chem.* **72** (2005) 367

[57] Z. Liu, X. Zhang, Y. Zhang, and J. Jiang, *Spectrochimica Acta Part A* **67** (2007) 1232

[58] H. L. Chen, Y. H. Pan, S. Groh, T. E. Hagan, and D. P. Ridge, *J. Am. Chem. Soc.* **113** (1991) 2766

[59] W. Weltner Jr. and R. J. van Zee, *Chem. Rev.* **89** (1989) 1713

[60] A. van Orden and R. J. Saykally , *Chem. Rev.* **98** (1998) 2313

[61] M. C. McCarthy, C. A. Gottlieb, H. Gupta, and P. Thaddeus, *The Astrophys. J.* **652** (2006) L141

[62] E. Roueff and E. Herbst *J. of Phys.: Conf. Series* **192** (2009) 012008

[63] J. D. Watts and R. J. Bartlett, *J. Chem. Phys.* **97(5)** (1992) 3445

[64] D. W. Arnold, S. E. Bradforth, T. N. Kitsopoulos, and D. M. Neumark, *J. Chem. Phys.* **95** (1991) 8753

[65] J-S. Chang, P. A. Lawless, and T. Yamamoto, *IEEE Trans. on Plasma Sci.* **19** (1991) 1152

[66] K. Drenck, P. Hvelplund, S. Brøndsted Nielsen, S. Panja, and K. Støchkel, *Int. J. Mass Spect.* **273** (2008) 126

[67] S. Jinno, T. Takao, K. Hanada, M. Goto, K. Okuno, H. Tanuma, T. Azuma, and H. Shiromaru, *Nuc. Inst. and Meth. in Phys. Res. A* **527** (2007) 568

[68] O. V. Boltalina, P. Hvelplund, T. J. D. Jørgensen, M. C. Larsson, and D. A. Sharoitchenko, *Phys. Rev. A* **62** (2000) 023202

[69] H. Shen, P. Hvelplund, D. Mathur, A. Bárány, H. Cederquist, N. Selberg, and D. C. Lorents, *Phys. Rev. A* **52** (1995) 3847

[70] S. P. Møller, *Nuc. Inst. and Meth. in Phys. Res. A* **394** (1997) 281

[71] J. Ladislas Wiza, *Nuc. Inst. and Meth.* **162** (1979) 587

[72] F. Mandl, *Statistical Physics*, 2nd ed., John Wiley & Sons, Bookcraft Bath Ltd, Great Britain, (2000), p.4

[73] V. Weisskopf, *Phys. Rev.* **52** (1937) 295

[74] K. Hansen, *Phil. Mag. B* **79** (1999) 1413

[75] K. Hansen, E. E. B. Campbell, and O. Echt, *Int. J. Mass. Spec.* **252** (2006) 79

[76] K. Hansen, and E. E. B. Campbell, *Int. J. Mass. Spec.* **233** (2004) 215-221

[77] J. U. Andersen, E. Bonderup, and K. Hansen, *J. Phys. B: At. Mol. Opt. Phys.* **35** (2002) R1

[78] A. A. Scheidemann, V. V. Kresin, and W. D. Knight, *Hyperf. Int.* **89** (1994) 253

[79] J. U. Andersen, E. Bonderup, K. Hansen, P. Hvelplund, B. Liu, U. V. Pedersen, and S. Tomita, *Eur. Phys. J. D.* **24** (2003) 191

[80] U. Näher and K. Hansen, *J. Chem. Phys.* **101** (1994) 5367

[81] K. Hansen and U. Näher, *Phys. Rev. A* **60** (1999) 1240

[82] K. Hansen and E. E. B. Campbell, *J. Chem. Phys.* **104** (1996) 5012

[83] D. Schröder, and D. Sülze, *J. Chem. Phys.* **94** (1991) 6933

[84] R. C. Weast(Ed.), *CRC Handbook of Chemistry and Physics*, 89th ed., CRC Press, 2008-2009

[85] M. T. Suter, P. U. Andersson, and J. B. C. Pettersson, *J. Chem. Phys.* **125** (2006) 174704

[86] D. Eisenberg and W. Kauzmann, *The structure and properties of water*, Oxford University Press, London (1969)

[87] P. M. Holland and A. W. Castleman Jr., *J. Phys. Chem.* **86** (1982) 4181

[88] G. H. Peslherbe, B. M. Ladanyi, and J. T. Hynes, *J. Phys. Chem. A* **103** (1999) 2561

[89] Z. Shi, J. V. Ford, S. Wei, and A. W. Castleman Jr., *J. Chem. Phys.* **99** (1993) 8009

[90] R. C. Weast(Ed.), *CRC Handbook of Chemistry and Physics*, 58th ed., CRC Press, 1978

[91] E. Tombari, G. Salvetti, C. Ferrari, and G. P. Johari, *J. Chem. Phys.* **123** (2005) 214706-1

[92] M. Oguni, S. Maruyama, K. Wakabayashi, and A. Nagoe, *Chem. Asian J.* **2** (2007) 514

[93] C. Hock, M. Schmidt, R. Kuhnen, C. Bartels, L. Ma, H. Haberland, and B. v. Issendorff, *Phys. Rev. Let.* **103** (2009) 073401

[94] R. Lemus, *J. Mol. Spectr.* **225** (2004) 73

[95] J. Szczepanski, R. Hodyss, and M. Vala, *J. Phys. Chem. A* **102** (1998) 8300

[96] K. Hansen, J. U. Andersen, P. Hvelplund, S. P. Møller, U. V. Pedersen, and V. V. Petrunin, *Phys. Rev. Let.* **87** (2001) 123401-01

[97] J. U. Andersen, C. Gottrup, K. Hansen, P. Hvelplund, and M. O. Larsson, *Eur. Phys. J. D* **17** (2001) 189

[98] J. U. Andersen, C. Brink, P. Hvelplund, M. O. Larsson, B. Bech Nielsen, and H. Shen, *Phys. Rev. Let.* **77** (1996) 3991

[99] E. Kolodney, A. Budrevich, and B. Tsipinyuk, *Phys. Rev. Let.* **74** (1995) 510

[100] J. H. Moon, M. Sun, and M. S. Kim, *J. Am. Soc. Mass. Spec.* **18** (2007) 1063

[101] Y. Toker, O. Aviv, M. Eritt, M. L. Rappaport, O. Heber, D. Schwalm, and D. Zajfman, *Phys. Rev. A* **76** (2007) 053201